NASA Technical Memorandum 82535

Space Processing Applications Rocket (SPAR) Project

SPAR VII Final Report

OCTOBER 1983

25th Anniversary
1958-1983

NASA

NASA Technical Memorandum 82535

Space Processing Applications Rocket (SPAR) Project

SPAR VII Final Report

Richard M. Poorman, *Compiler*
George C. Marshall Space Flight Center
Marshall Space Flight Center, Alabama

NASA
National Aeronautics
and Space Administration
Scientific and Technical
Information Branch
1983

TABLE OF CONTENTS

CHAPTER I

SPACE PROCESSING APPLICATIONS ROCKET (SPAR) PROJECT

SPAR VII - FINAL REPORT

INTRODUCTION

The unique low-g environment of space affords an opportunity for exploring and developing techniques for processing a variety of materials without the constraining gravitational influences as evidenced with the processing of liquid phase materials or melts on Earth. The Materials Processing in Space (MPS) program is directed toward the stimulation and development of the associated science and technology required to pursue these investigations. This NASA activity is undertaken in cooperation with the scientific community and includes follow-on studies of specific areas of scientific research emphasizing those selected investigations of materials and processes wich best demonstrate potential benefit from the enhanced sensitivity of the controlled processing in a low-g environment. Examples of interest in the program are the reduction and/or elimination of adverse thermal effects such as convection, sedimentation of heavy particles, buoyancy rise and positioning aspects of bubbles in liquids or melts, and the stratification effects of particulates of variable densities in solution. These and similar studies are considered to be the means to expand the limiting frontier in the development of new materials and processes which are envisioned ultimately to be of immeasurable benefit to mankind. As complementary to the research and technological nature of the investigations, the evolving emphasis is being directed, with the advent of the Shuttle and increased payload potential, toward commercialization and the development of self-sustaining programs yielding direct product benefit.

The initial precursory zero-g demonstrations and investigations associated with this family of scientific experiments were proposed and developed for the Apollo flights beginning in the late 1960's and continued with Skylab and Apollo-Soyuz flights through the mid-1970's. During the period between the close of that era and the orbital space flights on the Space Shuttle in the 1980's, the Space Processing Applications Rocket (SPAR) project has provided the only viable flight opportunity for low-g scientific investigations for experimenters, and is serving in a precursory role for planned and approved Shuttle investigations. It is also anticipated that sounding rocket flights could satisfy a continuing need, and a complementary role, for the establishment and definition of future precursory Shuttle experiments.

The SPAR project is part of the MPS program of the Office of Space and Terrestrial Applications (OSTA) which is responsible for directing research into the scientific effects of materials processing in the unique environment of space. This effort involves participation and interaction from various disciplines of the scientific community, government-supported laboratories, universities, and industrial organizations, in addition to foreign participation.

The Black Brant VC (BBVC) sounding rocket series, which is currently the carrier vehicle for the scientific payloads, with a Nike-boosted configuration available for heavier payloads, provides the opportunity to process materials in a low-g environment for periods up to five minutes in duration during a sub-orbital flight.

The rocket flights, which are conducted at WSMR, afford experimenters and apparatus developers a flight opportunity for a proof-of-concept verification and/or refinement of equipment operation and procedures prior to the longer duration, more sophisticated Shuttle flights.

This SPAR flight, which is the seventh in a planned series of rocket flights, occurred on May 14, 1980, and carried three experiments. The investigations for the experiments comprising the payload manifest are managed and coordinated by the MPS Projects Office of the Marshall Space Flight Center (MSFC).

Previous experiments flown on the SPAR flights include the measurement of liquid mixing due to spacecraft motion, and the dispersion of normally immiscible materials in the area of fluid dynamics. Solidification experiments involving gravitational effects on dendritic growth, epitaxial growth, and solidification of eutectic materials with widely differing densities have flown previously, in addition to solidification studies of interactions between second-phase particles and an advancing crystal-liquid interface and gravity-induced convection on cast microstructures. In the area of multiphase particle interaction, various experiments were conducted on the migration and coalescence of bubbles and particles, closed-cell metal foam, and the dispersion strengthening of composites.

The SPAR project has been increasingly active in supporting research in the promising area of containerless processing with previous flights, including experiments on cast beryllium and the processing of amorphous ferro-magnetic materials in an electromagnetic field, and control of liquid droplets by an acoustic field in the furtherance of the state-of-the-art of acoustic containerless processing technology.

The SPAR flights have, through an evolutionary program, addressed experiments of increasing complexity and refinement and have afforded additional flight opportunities consistent with the maturity of each investigation. The payloads selected for this flight manifest were based on the advanced state-of-the-preparedness of their ground-based research activity.

The following experiments are included in this SPAR VII report:

- "Containerless Processing Technology" (Experiment No. 76-20), illustrating stability, oscillation and rotation as the three major aspects of containerless processing technology in space;

- "Containerless Processing Technology" (Experiment No. 77-18) illustrating sphericity and positioning of gas bubble inside a liquid drop;

- "Comparative Alloy Solidification " (Experiment No. 76-36) investigating casting phenomena of metal alloys, solidifying Tin 3% Bismuth.

The post-flight results and analyses of each experiment flown on SPAR VII as prepared by the respective flight investigators, in addition to an engineering report on the performance of the SPAR VII Science Payload, are contained in separate sections of this technical memorandum. With the successful completion of this flight and subsequent data analysis, much useful data and information were accumulated for directing and developing experimental techniques and investigations toward an expanding, commercially beneficial program of materials processing in the coming Shuttle era.

CHAPTER II

SPACE PROCESSING APPLICATIONS ROCKET PROJECT

SPAR VII

ENGINEERING REPORT

June 30, 1983

1.0 SUMMARY

The SPAR VII (R-18) Nike-Black Brant VC rocket was launched from White Sands Missile Range (WSMR), New Mexico, at 10:30 a.m. CST on May 14, 1980. The 963 pound gross payload achieved an apogee of 144.8 statute miles; 1.5 miles higher than predicted and a low-g period of 331 seconds. The launch was successful and the payload was recovered intact.

2.0 SPAR VII (R-18) PAYLOAD CONFIGURATION

The SPAR VII (R-18) science payload consisted of three materials experiments, the Experiment Support Module (ESM), and the Abbreviated Measurement Module (AMM). The SPAR VII experiments are:

76-20/3	Containerless Processing Technology
76-36/2	Comparative Alloy Solidification
77-18/1	Dynamics of Liquid Bubbles

The orientation of the experiments within the SPAR VII rocket vehicle is shown in Figure 1.

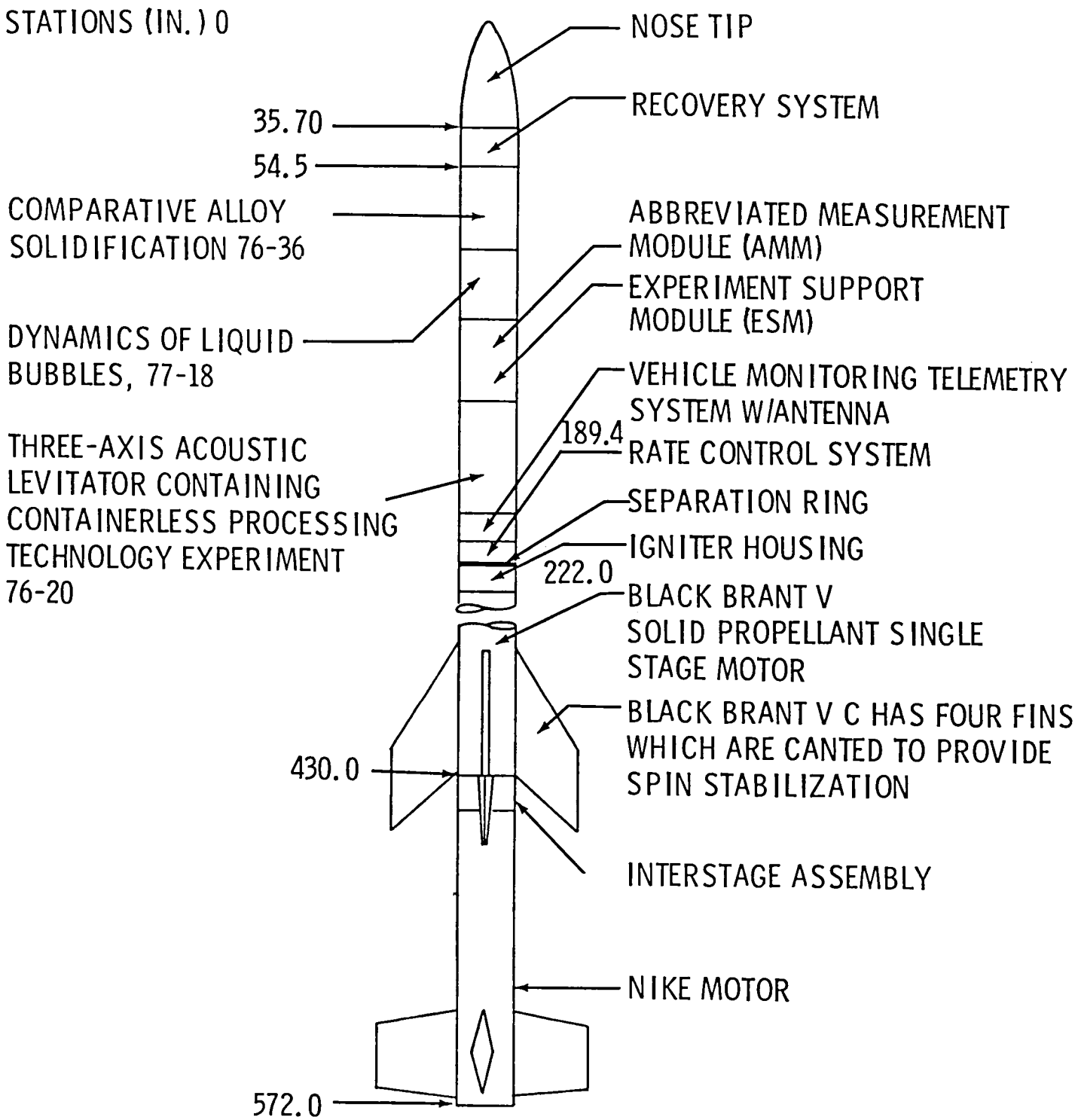

Figure 1. SPAR VII Launch Vehicle and R-18 Payload Configuration

3.0 ROCKET PERFORMANCE

3.1 Flight Sequence

The SPAR VII flight profile is shown in Figure 2. The predicted and actual sequence of events are shown as a function of flight time.

3.2 Low Gravity

The predicted low-g (10^{-4} or less) time was 322 seconds. This value was based upon an all-up payload weight of 963 pounds. The science payload furnished by MSFC weighed 645 pounds.

The Measurement Module low-g accelerometer measurements indicated that the low-g period began at T+79, T+75, and T+82 seconds on the X, Y, and Z axes, respectively, and ended at T+413, T+415, and T+424 seconds. Taking the latest onset of low-g (T+82 in the Z-axis) and the earliest termination of low-g (T+413 in the X-axis), indicates a low-g period of 331 seconds. The minimum low-g period required by experiments was 260 seconds.

4.0 PAYLOAD SUPPORT

4.1 Payload Sequence of Events

Experiment 76-36 required preheat power prior to launch that was supplied by ground power, beginning at T-90 minutes. At T-0, a lift-off signal was given which activated a timer within all three experiments for control of events during the flight. The planned power removal to experiments at 728 seconds occurred at 727 seconds.

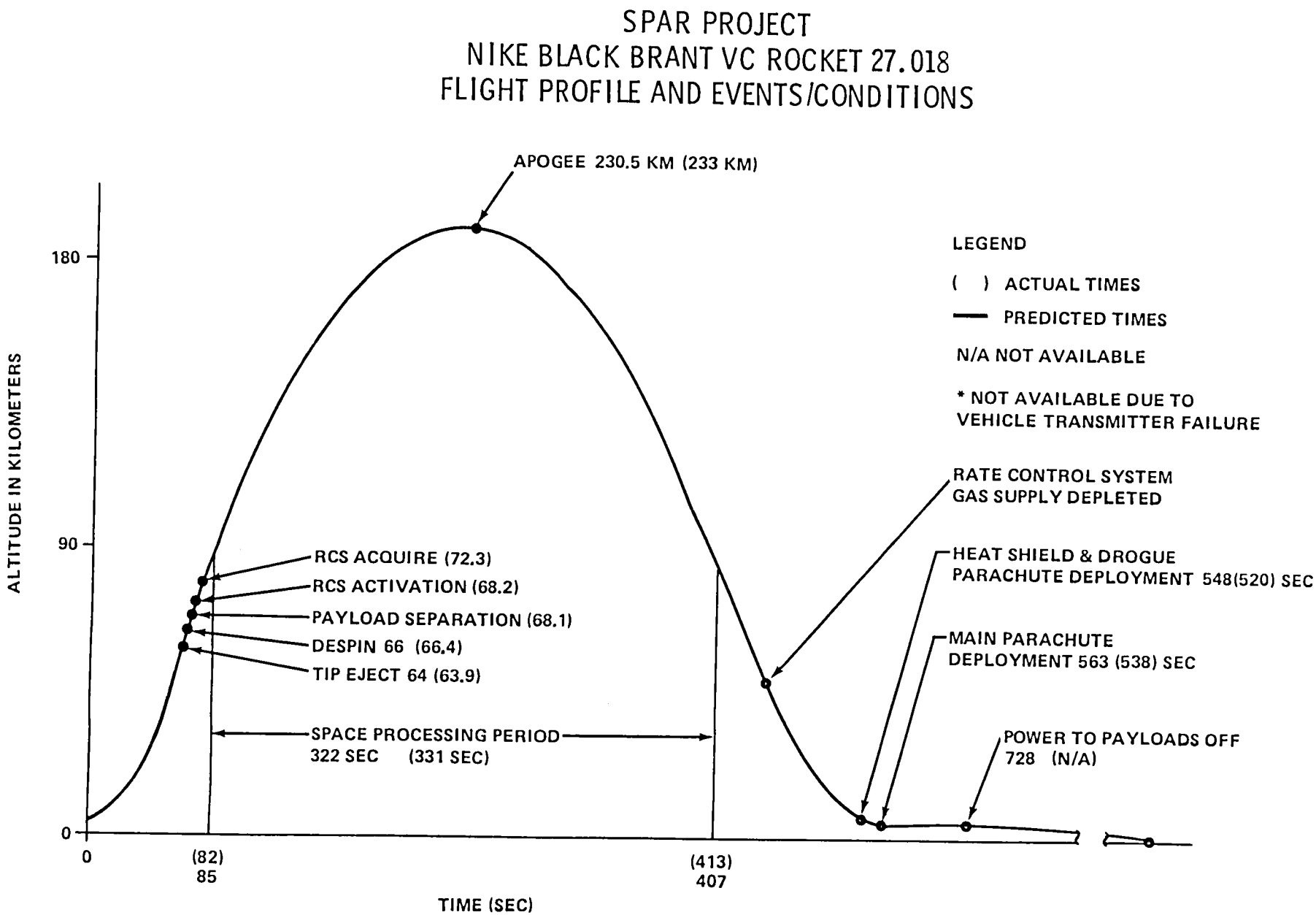

Figure 2. Flight Profile and Events

4.2 Payload Power

Transfer of electrical power from ground-support equipment to the flight battery was accomplished at 3 minutes prior to launch. The science payload battery, located in the Experiment Service Module (ESM), suppplied power to all experiments. Battery voltage measurement (M01-SM) indicates that the battery voltage was 35.0 volts at lift-off and remained there until 85 seconds, when it dropped to 34 volts, corresponding to activation of Experiments 77-18 and 76-20. Here it remained essentially constant until 445 seconds, then returned to 35 volts, corresponding to Experiment 76-20 power cut-off. The battery current measurement indicates that the current was about 21 amperes at lift-off, which is 2.3 amperes higher than calculated battery load profiles. At T+85 seconds, it increased to 30 amps as Experiments 76-20 and 77-18 were activated. It remained at 30 amps until 445 seconds, when Experiment 76-20 was cut off.

5.0 EXPERIMENTS

5.1 Experiment 76-20/3: Containerless Processing Technology

This experiment utilized the Jet Propulsion Laboratory (JPL) Acoustic Levitation Space Processing Rocket Instrument (ALSP) for the purpose of investigating the stability and manipulability of a liquid drop. The primary objectives of this flight were to:

1) Demonstrate the transport capability of the acoustic hamber for collision and coalescence of quiescent drops. The initial perturbation of the drops generated by the drop injection systems are allowed to damp down. Quiescent drops are transported to the center of the chamber for coalescence by the acoustic forces. This transport capability of the chamber and the possible perturbation on the drop shapes are studied.

2) Study the mixing effects generated by collision and coalescence of oscillating drops. Two oscillating drops are made to coalesce at the center of the chamber. The mixing effects generated by the coalescence are studied from the film file record.

3) Study the shift of natural frequencies of drop oscillation as a function of oscillation amplitude. The shift of natural frequencies of drop oscillation at large amplitude from those predicted at small amplitude has been observed in a laboratory immiscible system. The experiment allows comparison of values from zero-gravy and neutral bouyancy systems.

Four runs of approximately 6.5 seconds each were completed in this experiment. Each run consisted of an injector delivering a fluid drop to the ALSP, the levitation and manipulation of the fluid drop, and finally the removal of the drop from the levitation chamber. The runs were initiated at T+107 seconds, T+170 seconds, T+234 seconds, and T+299 seconds; drop removals occurred at 156 to 169 seconds, 220 to 233 seconds, and 285 to 298 seconds.

The first three runs of this experiment were unsatisfactory with the drop adhering to the injector; however, the fourth run was partially successful, thereby supporting the prescribed experiment objectives.

COMPILER'S NOTE: The SPAR VII acceleration records for the low-g period in question show all values to be less than 10^{-4}g's. This is the same as other flights and as expected. Rate control systems data also indicate normal flight conditions for this period.

The unplanned movements of the liquid drops in Experiment 76-20 were symmetrical about a point near the center of the experiment chamber. External forces from the payload that would correspond to these drop movements would require rotation of the payload about this same center of symmetry. In that the payload center of gravity (c.g.) is some four feet from this center of symmetry, such a payload rotation appears unlikely.

Also, there were no unplanned drop movements in Experiment 77-18 aboard SPAR VII operating at the same time that Experiment 76-20 was experiencing anomalies, which further indicates no payload movements which would influence the experiment results.

5.2 Experiment 76-36/2: Comparative Alloy Solidification

This experiment used tin and 3% bismuth to continue the low-g study of casting phenomena by investigating the solidification of selected metal alloys during the weightless period of a SPAR sounding rocket flight. Other objectives of this experiment included the verification of the conclusions of SPAR Experiment 74-21 by solidifiying metallic alloys in the 76-36 hardware and the procurement of quantitative segregation data as a function of gravity force.

The sample of tin and 3% bismuth was heated to $220^{o}C \pm 10^{o}C$ by a Lockheed furnace. The heating began at T-90 minutes to insure that the sample would be molten at launch. Allowing a minimum of a least 60 seconds for the damping of the fluid motions due to the launch vibrations, the cool down of the experiment material was started at T+190 sec. The cool down ended at T+400 sec and the low-g period ended at T+413 sec which allowed a total loss of time of 223 sec for the experiment sample to cool down and solidify. However, the cooling rate was slower than predicted due to a slower gas exhaust rate which required the sample to use much of the low-g time in cooling to solidification temperature. The slower gas exhaust rate occurred because of unexpected cooling system performance differences between pre-launch atmospheric conditions and the near-vacuum of a 230 kilometer altitude. Other than this problem with the quench rate, the experiment apparatus performed satisfactorily.

5.3 Experiment 77-18/1: Dynamics of Liquid Bubbles

This experiment utilized the JPL Acoustic Levitator ALSP for the purpose of investigating the stability and manipulability of a liquid drop. The primary objectives of the flight were to:

1) Determine the sphericity of a positioned liquid bubble. The equilibrium shape of a positioned liquid bubble is the result of the balance of acoustic forces, surface tension, and spacecraft G-jitter. The sphericity of the liquid bubble is determined from the film record.

2) Determine the efficiency of bubble centering by oscillation. The centering force generated by the oscillation of the liquid shell is studied by acoustically exciting the liquid shell in its various normal oscillation modes. The centering mechanism wil be compared with theoretical models developed at JPL.

3) Determine the perturbation on bubble centering by G-jitter. As the rocket experiences G-jitter, the liquid bubble moves back and forth within the chamber. The liquid bubble experiences a non-symmetrical modulating force, thus perturbing its shape. This can produce unwanted coupling between rotation and oscillation of the drop.

4) Study the natural resonant frequencies and damping mechanism of bubble oscillation. The resonant frequencies and the damping coefficient have been calculated. This experiment allows comparison of observed and calculated values.

5) Adiabatic expansion of liquid bubble. The liquid bubble's physical size and wall thickness is determined by the pressure difference across the two boundaries and the surface tension of the water/air interface. As the exterior pressure decreases, the bubble expands its size and reduces its wall thickness. The post-flight film analysis studies the bubble surface velocities and accelerations, and also the surface instabilities.

At 105 seconds after the SPAR sounding rocket launch, the fluid delivery to the ALSP was started and was completed 15 seconds later. At T+125 seconds, air was injected into the liquid drop in the ALSP. At T+290 seconds, when the decompression valves were opened, the experiment sample expanded due to the decreasing pressure.

This experiment apparatus worked as planned with the exception of the air bubble injected into the liquid drop being smaller than anticipated.

6.0 INSTRUMENTATION

6.1 Low-G Accelerations

The low-g data indicates that a low-g environment considerably less than 1×10^{-4}g was achieved in all three axes. The X-axis Linear Acceleration Measurement (AO2-MM) indicates that low-g entry in that axis was at about 79 seconds and exit at about 413 seconds with the g-levels during this period ranging from -0.9 to 0.4×10^{-4}g. A spike of 0.9×10^{-4} occurred on the X-axis plot in the -X (down range south) direction at approximately 108 seconds. A spike of $.23 \times 10^{-4}$ occurred on the Y-axis plot in the +Y (cross range, east) direction at 108 seconds.

Several, some nineteen or so, spikes occurred in the Y-axis beginning at 272 seconds and ending at 412 seconds. There values range up to about 1×10^{-4} g's. It is not known at this time what caused these perturbations, but they may be related to the lowering of pressure in Experiment 77-18.

The Z-axis Linear Acceleration Measurement (A04-MM) indicates the low-g entry in that axis as 82 seconds and exit at 424 seconds with the g-level ranging from -0.3 to 0.16×10^{-4}g. There were no significant spikes in the z-axis.

6.2 Pressures

Ambient pressure in the AMM (DOI-MM) was 13.3 psia at lift-off, and 0.6 psia at T+49 seconds. The SPL ambient pressure measuring device (DO6-MM) was also located in the AMM, and monitored from 30 to 10^{-4} torr in six ranges. It indicated that the ambient pressure continued to decrease until a minimum of 6.2 torr was reached at approximately T+184 seconds. From this point, the pressure began to rise, reaching 30 torr at 456 seconds.

6.3 Engineering Temperatures

SPAR VII temperature profiles closely resemble SPAR V data, and are slightly warmer than SPAR VI. All temperatures are well within the 20°C to 60°C range of previous SPAR flights. The temperature profiles are shown in Figure 2.

7.0 PAYLOAD RECOVERY

The R-18 payload landed approximately 2.75 kilometers south of Lady Bug Peak on the eastern side of the Andres Mountains. The landing site had a slope of approximately 35 degrees and consisted of a mixture of "brick-size" rock and sandy soil. The payload landed on its aft end, sinking approximately 15 centimeters into the semi-soft soil. It appeared that the forward end of

FIGURE 2. TEMPERATURE PROFILES

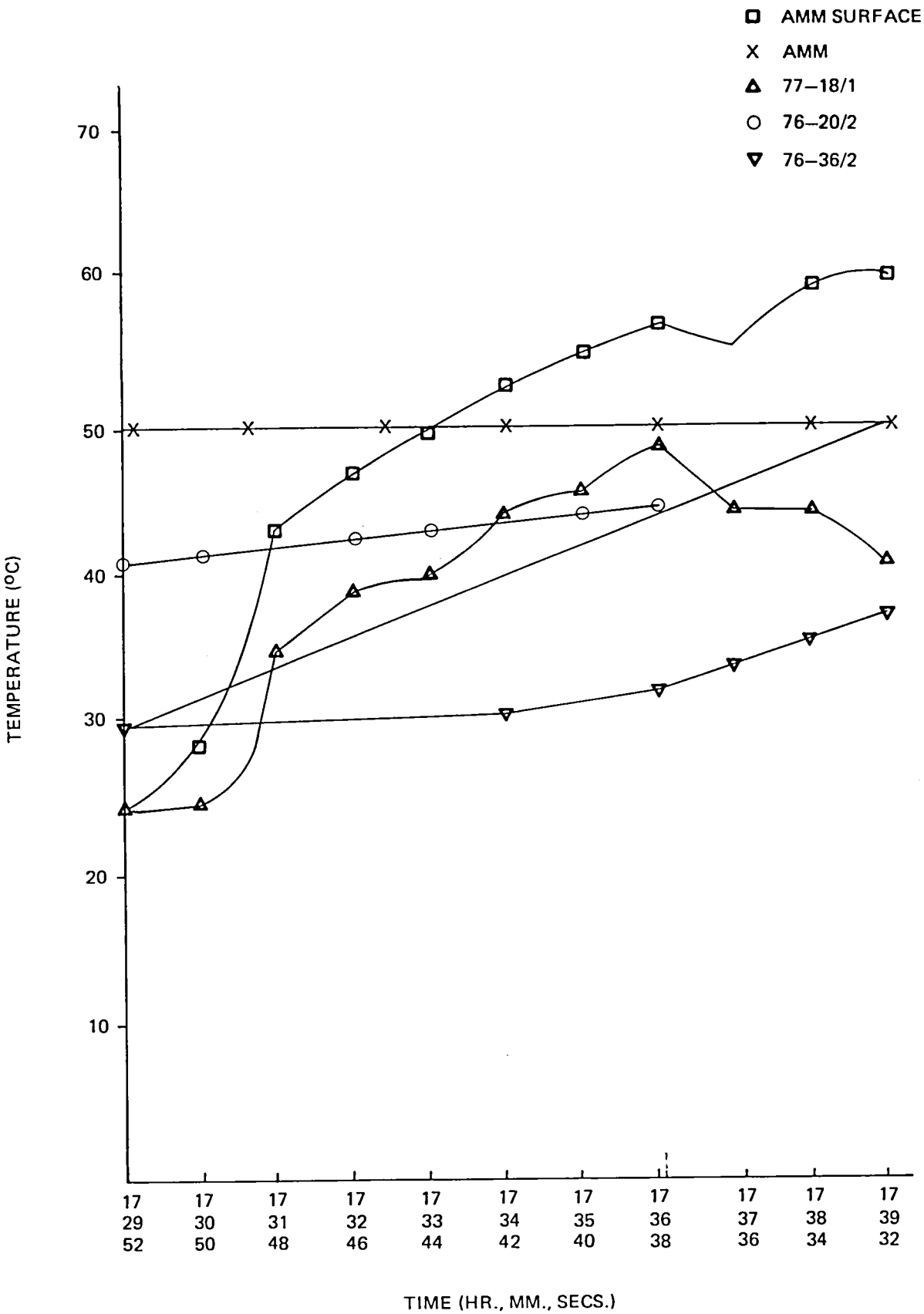

the payload fell generally uphill while at the same time the aft end began to roll down and across the slope. The forward end remained pointed uphill with the payload coming to rest about 23 meters from the initial point of impact. The parachute was stretched out forward of the payload. There appeared to be no major visible damage to the payload. The electrical safing box was used to ensure the payload was de-energized. Goddard Space Flight Center (GSFC) personnel removed the battery from the rate control system.

The parachute lines were detached from the four webbed risers and specially designed recovery lifting hardware was attached to the four risers. The payload was lifted by a cargo helicopter and transported, while slung beneath the helicopter, to road number 13, approximately 800 meters northeast of the landing site. At this point, the helicopter landed and the payload was loaded inside the cargo helicopter, secured, and transported without incident to the Launch Complex 36 Vehicle Assembly Building.

CHAPTER III

SPAR EXPERIMENT 76-36

SPAR VII

COMPARATIVE ALLOY SOLIDIFICATION

Principal Investigator: Dr. M. H. Johnston

Co-Investigator: Mr. R. A. Parr

THE INFLUENCE OF ACCELERATION FORCES ON DENDRITIC GROWTH AND GRAIN STRUCTURE

M. H. Johnston and R. A. Parr

Earlier studies[1,2] have proposed fluid flow as a determinant in the final structure of castings. The more recent discussions[3] allude to the control of convection as crucial to the regulation of grain size and material homogeneity. The presence of convection with its thermal pulses and fluid movement induces remelting,[4] fragmentation, and generally disrupts the dendrite solidification process. In addition, interdendritic flow contributes to macrosegregation in castings.[5,6]

Experiments related to Materials Processing in Space have led to investigations of such phenomena through analysis of the convection driving force; gravity or acceleration. Metal model casting simulation experiments on earth and in low-gravity[7,8] indicated that in the absence of gravity induced acceleration, the resulting structure would be large grained and columnar. Conjunctively, the dendrite secondary arm spacings are more uniform and larger than their earth-based counterparts.

The purpose of the present research was to extend the metal-model experiments to metal systems and to study the effect of acceleration force from the low-gravity (10^{-4} g's) available during sounding rocket flights, up to 5 g's in a centrifuge apparatus, thus magnifying the influence of the gravity force on the structure. This paper shows grain size distribution and shape, constituent segregation and dendrite arm spacings in the Sn-Pb system solidified at three selected cooling rates under the range of accelerations. A rationale will be proposed for the increase in secondary arm spacings at low-gravity, based on previous dendrite coarsening theories.[4,9,10]

Experimental Procedure

A centrifuge furnace apparatus was designed and built to solidify alloys under various accelerations. Centrifuge instrumentation consisted of a d.c. magnetic torque motor, a low-noise electrical slip ring, a gas quench system, temperature recorders, and a programmable temperature controller. The electronic control system and the furnace cannister were prototype units for a Space Processing Applications Rocket (SPAR) flight furnace.

The Sn-15wt%Pb alloy was prepared from elements of 99.9 percent nominal purity by melting in air and casting into a cold graphite crucible. The samples were removed and placed into a second graphite crucible for processing. Each sample was 12mm wide by 54mm long by 60mm deep. The acceleration force was applied parallel to the longer dimension. A schematic of the furnace cannister is shown in Figure 1.

Samples were melted by two flat heating element plates parallel to the larger crucible walls. Cooling was accomplished by flowing a quench gas (helium or nitrogen) through parallel quench manifolds placed directly against the smaller crucible walls. The acceleration force was also applied parallel to the cooled walls, a situation always conducive to increased fluid flow.

The alloy was melted and soaked for one hour at 220°C. The centrifuge was operated at the desired acceleration level three minutes prior to the furnace power cut-off, and initiation of quench. Cooling rates were varied by changing the pressure of the quench gas. Six thermocouples located in the walls of the graphite crucible recorded the time vs. temperature history.

The SPAR flight solidification sequence was similar to that used in the centrifuge experiments. The sample was held molten at 220^{o}C before launch. Approximately one minute after entry into low-gravity, the power was cut to the furnace and the quench was initiated. The sample solidified during the remainder of the low-gravity period. Temperatures from the six thermocouples in the graphite crucible were recorded via telemetry.

Experiment Results

Two hundred-sixty gram samples of Sn-15wt%Pb were solidified at three cooling rates and four acceleration levels of 1g, 1-3/4g, 3-1/2g, and 5 g (the symbol g is used in the discussion to represent the gravitational constant 980 cm/s^2). Since the low-gravity time is limited to ~5 minutes on SPAR, the flight sample had to be solidified at a rapid cooling rate during the flights acceleration level of 10^{-4}g. The samples were carefully cross sectioned as shown in Figure 2. The "B" surfaces were polished and etched in 10% HCl and H_2O to reveal the grain structure. The "B" surfaces along with g-levels are shown in Figures 3 and 4 for the fast cooling rate and the flight sample.

Since it was expected that fluid flow prior to solidification and through the ensuing dendrite arms would alter the melt thermal parameters, experiments were conducted to obtain the thermal profile in the liquid during the solidification. Two sets of thermocouples were placed in the melt; vertical thermocouples (parallel to the quench) to determine the curvature of the isotherms and growth front, and horizontal thermocouples (perpendicular to the quench) to determine the temperature gradients ahead of the solidification front and the local solidification times.

The vertical measurements showed that the growth front was curved since the lower thermocouples registered growth before the upper thermocouples. This became more pronounced as the acceleration force was increased. In all cases the primary growth rates were extremely rapid, indicating that growth occurred almost simultaneously throughout the melt. The acceleration level and cooling rate had a negligible effect on this initial growth rate and the temperature gradients, but they did influence the growth

rate and temperature gradient of the subsequent eutectic. The temperature gradient decreased with acceleration and the growth rate of the eutectic increased for the 13.5°C/min. cooling rate.

Secondary dendrite arm spacings were measured to obtain an estimate of dendrite permeability, and are given in Figure 5. The ground-based arm spacings varied with furnace cooling rate, decreasing from 0.07mm at 3°C/min. to 0.04mm at 13.5°C/min. The spacing from the flight experiment is also shown on the graph. This value does not lie on the ground-based data curve for the same cooling rate.

Since the thermal data had indicated that the primary tin dendrite growth rates were virtually independent of the cooling rates and therefore could not control the final arm spacing, further studies were made to determine the dominant factor. Thermocouples were placed in Sn-15wt%Pb samples which were directionally solidified using different temperature gradients and growth rates. The growth rates of the primary dendrites and the ensuing eutectic front were measured. There was no dependance of the dendrite arm spacing on the primary growth rate or the temperature gradients. It was expected from earlier studies[4] that the secondary arm spacings would be a function of the time the dendrites were associated with the molten eutectic liquid. Four our case this meant the spacings would be proportional only to local solidification time of the eutectic. Figure 6 confirms this. However, since the flight sample would have short local solidification times (similar to the centrifuge 13.5°C/min. cooling rate samples) this still does not explain the flight sample's large secondary arm spacings.

The volume fraction of tin dendrites was measured using quantitative metallography. The value ΔV_v, the difference in volume fraction of tin between the top and bottom of the sample, is shown plotted in Figure 7. Both cooling rate and the acceleration affect the tin dendrite segregation, a slow cooling rate with a high acceleration producing the most segregation.

Figure 8 shows the measured grain size distribution of the samples at two cooling rates and three acceleration levels. The grain size decreases with an increase in the acceleration. Figure 9 compares the variation in grain size through the middle of the samples at different acceleration levels. The size of the grains decreases and their number increases from the top to the bottom of the samples. Grain size distribution is significantly affected by increasing the acceleration level. The flight sample data are super-imposed on the data from the centrifuge processed samples (Figure 9).

The role of fluid flow on dendrite fragmentation and the creation of small grains was further defined by inserting a ceramic coated silver screen[12] in one sample at 1.5cm intervals. A second sample was then processed without the screen. The cooling rate and acceleration level which produced the largest number of small grains in prior tests was used to process the two samples. Figure 10 shows representative sections of these samples. The sample with the silver screen impediment has large grains which appear to grow through the screen as opposed to the control sample which is still fine grained. Damping the flow through the use of a screen successfully retained the large grained structure.

X-Ray Laue photographs were taken perpendicular to the "B" surfaces (Figure 3). These photographs indicated that the large grains were generally oriented along (001), the plane which contains the preferred growth orientation for tin. The smaller grains had random orientations. The grains in the flight sample were also randomly oriented. The random orientation was substantiated by isometricity measurements (Table I) which show equiaxed orientation at 10^{-4} and 5g, and the greatest preferred orientation at 1g.

Table I

Isometricity Measurements
Percent Degree Orientation
Perpendicular to Quench

-g-	Sn-15Pb
10^{-4}	0
1	50
1-3/4	30
3-1/2	26
5	0

Discussion

An increase in the acceleration level above 1-g had an obvious effect on the grain structure in Sn-15Pb castings. When the molten metal was cooled, nucleation of primary dendrites occurred almost simultaneously throughout the melt. The gravity force drove the nuclei towards the bottom of the crucible, producing a greater pile-up of tin dendrites and hence a more curved interface with the larger accelerations.

Decreasing the cooling rate enhanced this effect. The greater coarsening (and hence larger dendrite arm spacings) which occurred at the slower cooling rate, permitted convective flow through the arms and subsequent fragmentation of the dendrites. These particles also sank in the gravity field, joining the initial nuclei, and grew as fine grains. The magnitude of segregation of the tin therefore becomes a function of both the gravity level and the cooling rate.

The large grains which survived fragmentation grew along the plane of greatest heat flow in tin, (001). Although their appearance is not elongated, this does suggest a relationship to the columnar zone in castings. The randomly oriented (equiaxed) fine grains occur as discussed above. Their number can be increased by increasing the fluid flow through greater acceleration forces. The effect is magnified when the cooling rate is slow and permeability to flow is high.

The grain sizes of the sample processed at 10^{-4} g's were slightly larger than the similarly processed 1-g sample, (which in turn had larger grains than the higher g processed samples). Due to the absence of convection at 10^{-4} g there was no fragmentation creating nuclei for new small grains.

In order to explain the arm spacing anomaly which occurred in the low-g sample we must begin with the initial solidification of the dendrite. As evidenced by the pyramidal growth shape of the primary stalk plus arms, the secondary arms would see an environmental like the one shown in Figure 11a.[9] There is both a concentration and temperature gradient along the primary dendrite. In addition, there is a concentration gradient between the root of the secondary arms and the tip. Coalescence theory[4] says that the root, having a negative radius has enhanced solute and a lower melting point, whereas the tip with positive radius is depleted in solute.

The solute diffuses from the cold to the hot regions and from the areas of higher concentration to those of lesser concentration. Consequently, solute from the front surface of A would diffuse towards B. Solute from the root area should also diffuse toward the lower concentration, higher temperature at B. Since B is already smaller, it will tend to dissolve. Midway through the process, dendrites A & B would look like Figure 11b. The head of A has bulged toward the higher temperature while the root areas has begun to decrease radius and fill in, with the region adjacent to dendrite B filling in faster. Figure 12 shows this bulging and dissolution during a solidification sequence of NH_4Cl-H_2O. Some examples of partial coalescence are shown in Figure 13, which includes the Sn-15Pb flight sample, and the metal-model NH_4Cl-H_2O. The process would occur repetitively during the initial period of dendrite growth. Later in the solidification the irregular shapes and sizes encourage other coarsening methods. Smaller dendrite arms are completely dissolved by the larger arms, or melt away at the base creating a potential nuclei.

The main driving forces for the coarsening are therefore: surface energy (for enlarging radii), temperature gradient, and concentration gradient. Surface energy is not expected to vary with gravity level, and will not be a factor in this discussion. If we use the earlier theories[4,10] and include the presence of a temperature gradient in the basic flux equations, we obtain a rate of coarsening

$$\frac{dr}{dt} = \frac{D_1}{d} \quad \frac{1}{C_L^r (1-k)} \left[\left(C_L^B - C_L^A \right) + K \left(T_L^A - T_L^B \right) \right]$$

where KD is thermal mobility factor. (In this case we have not made the substitution of dendrite radii for concentrations C_L^r and C_L^a). The rate of coarsening is dependent on both the temperature gradient and the concentration gradient. As either is increased the rate of coarsening increases.

The presence of fluid flow would affect both of these gradients. It has been shown by Flemings et al[5] in their macrosegregation studies that there is flow between the dendrite arms during solidification. We have shown that this flow is increased by gravitational acceleration. Conversely, the absence of gravity decreases the fluid flow. Therefore the concentration gradient and temperature gradient would be greater in low-gravity. Additionally, without the perturbations of hot fluid pulses, the dendrites grow more uniformly, allowing more uniform coalescence. Hence the low-gravity arm spacings are not only larger, but have less deviation than ground based.

Conclusions

It is concluded that the gravitational acceleration force has a role in creating the final grain structure of a material. On a macroscopic scale, the acceleration force

drives the fluid flow which causes dendrite remelting/fragmentation and macro-segregation. The extent of these effects is directly dependent on the acceleration level. Other solidification parameters such as cooling rate impact the structure by influencing the dendrite arm spacings and hence permeability to flow.

On a microscopic scale, the acceleration level affects the dendrite arm spacings and uniformity, again through fluid flow. At low (10^{-4}) accelerations, the local temperature and concentration gradients are greater, establishing a greater driving force for the coarsening. The absence of local thermal fluctuations encourages uniformity of the arm spacings.

References

1. S. Wojeichowski & B. Chalmers; Trans Met Soc AIME, 1968, v. 242, p. 690.

2. G. S. Cole & G. F. Bolling; Trans Met Soc AIME, 1967, v. 239, p. 1824.

3. M. C. Flemings, Materials Society Conference on Solidification Technology in the Foundry & Casthouse; University of Warwick, Conventry, Sept. 1980.

4. T. Z. Kattamis, J. C. Conghlin & M. C. Flemings, Trans Met Soc AIME, 1967, v. 239, p. 1504.

5. M. C. Flemings & G. E. Nerev, Trans Met Soc AIME, 1968, v. 242, p. 40.

6. N. Streat & F. Weinkerg, Met Trans, 1974, v. 5, p. 2539.

7. M. H. Johnston & C. S. Griner, Met Trans, 1977, v. 8A, p. 77.

8. M. H. Johnston, C. S. Griner, R. A. Parr, & S. J. Robertson, J. of Crystal Growth, 1980, v. 50, p. 831.

9. D. J. Allen & J. D. Hunt, Met Trans, 1976, v. 7A, p. 767.

10. K. P. Young & D. H. Kirkwood, Met Trans, 1975, v. 6A, p. 197.

11. M. H. Johnston & D. H. Baldwin, Met Trans, 1974, v. 5, p. 2395.

12. G. S. Cole & G. F. Bolling, Trans TMS - AIME, 1965, v. 233, p. 1568.

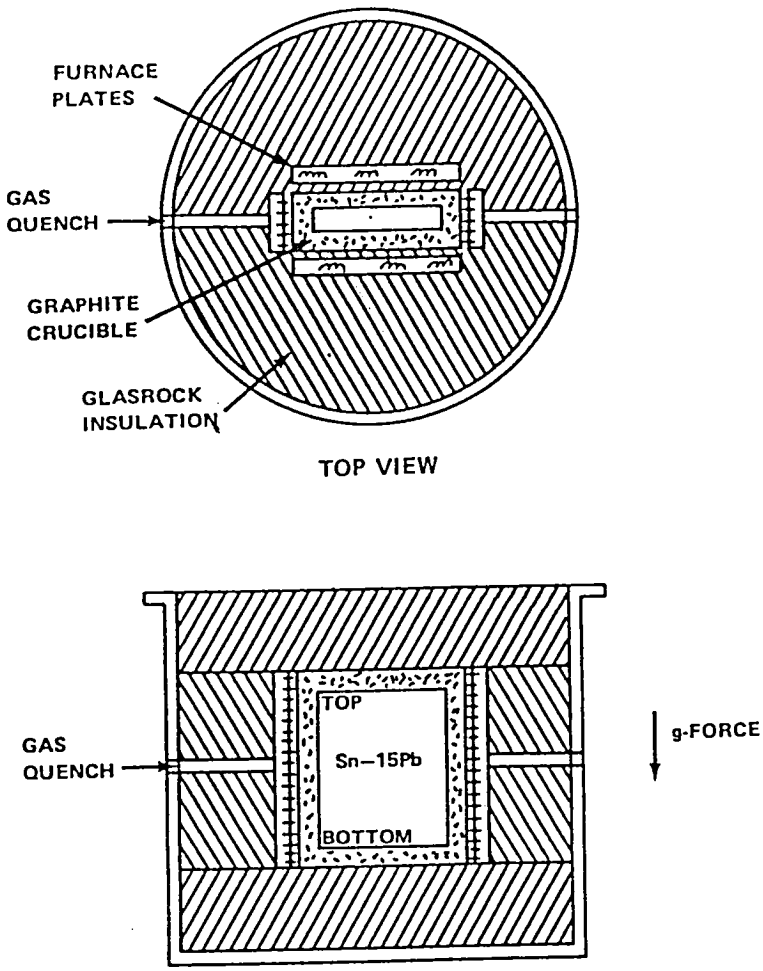

FIGURE 1: SCHEMATIC OF CANISTER ASSEMBLY

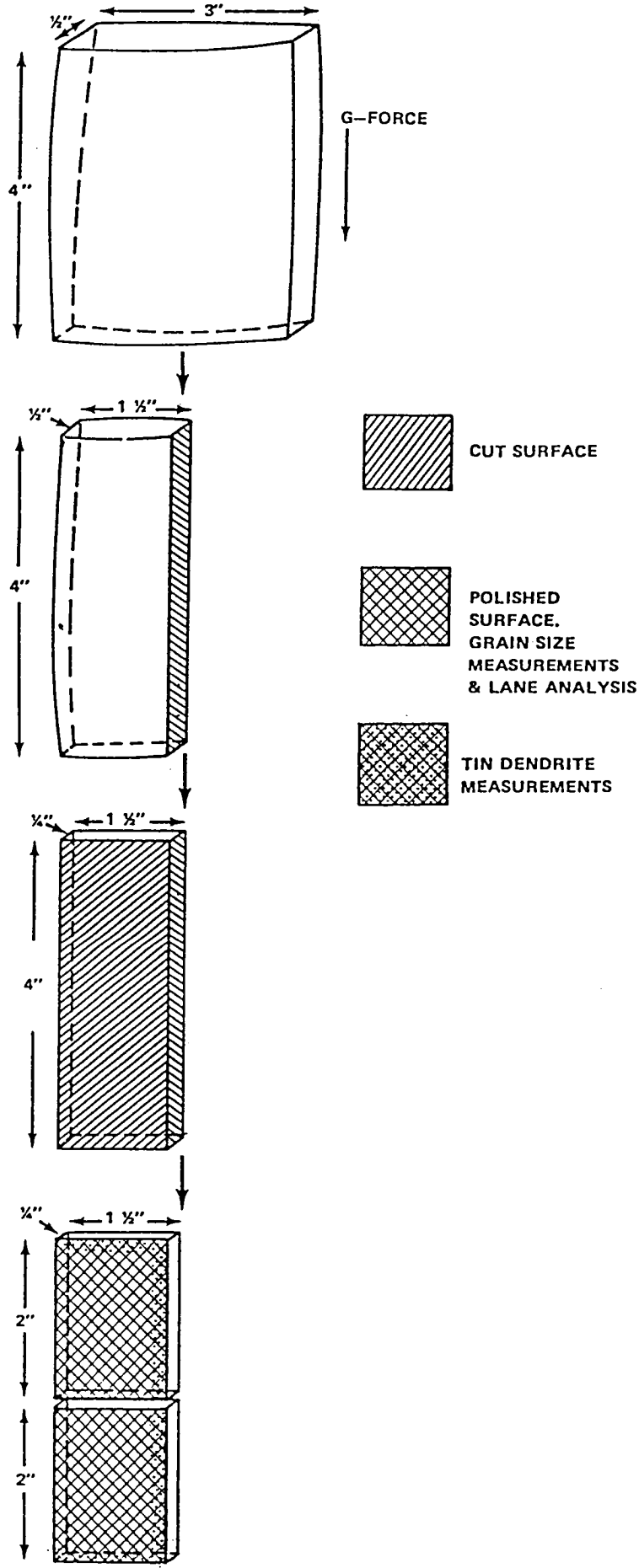

FIGURE 2: SCHEMATIC OF SAMPLE PREPARATION AND ANALYSIS

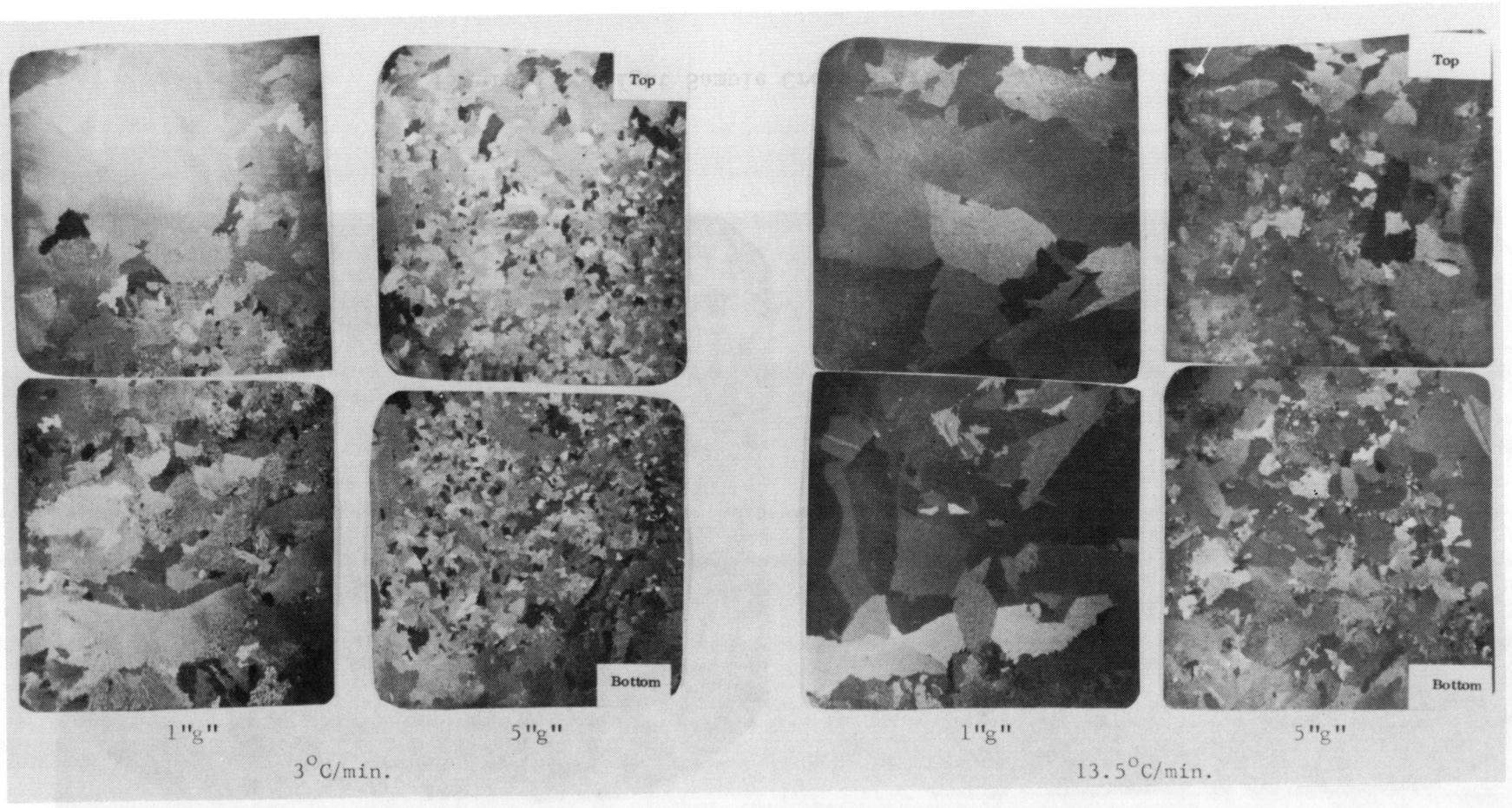

Figure 3. Grain Structure of Sn-15wt%Pb Solidified at Two Cooling Rates and Two Acceleration Levels (Magnification level:2X)

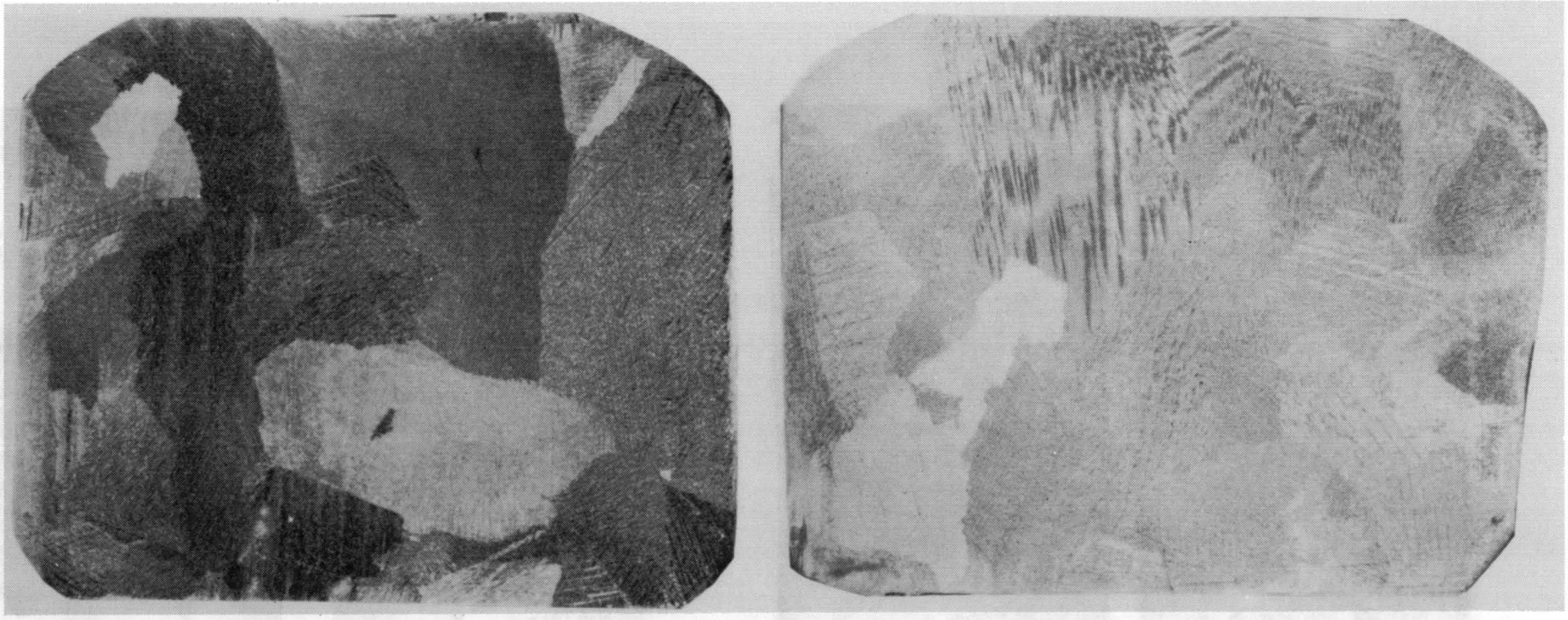

Figure 4. Flight Sample Cross Section (2-1/2X)

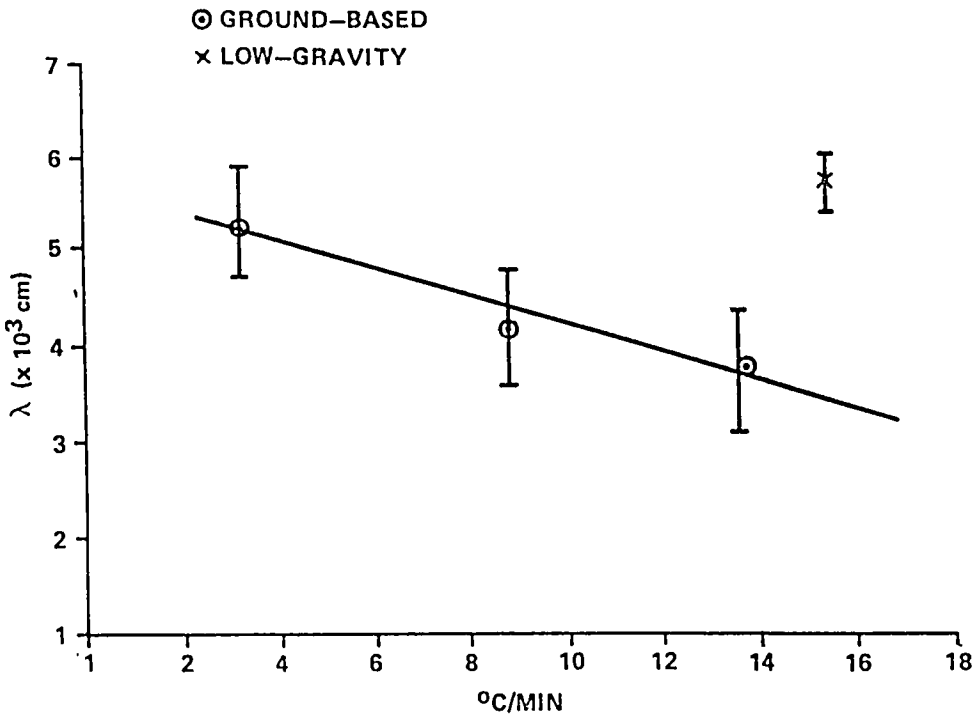

Figure 5. Secondary Dendrite Arm Spacings as a Function of Cooling Rate

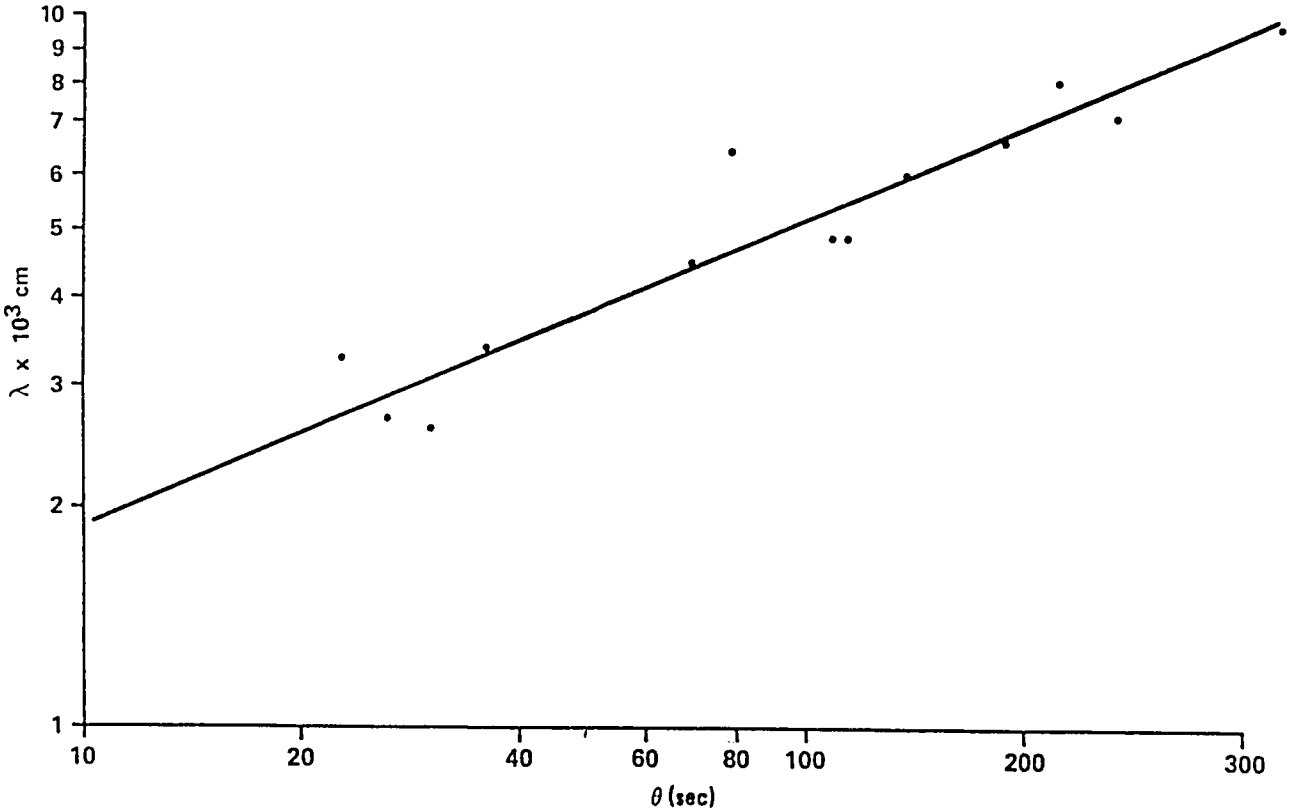

Figure 6. Secondary Dendrite Arm Spacings as a Function of Local Solidification Time of the Eutectic Phase

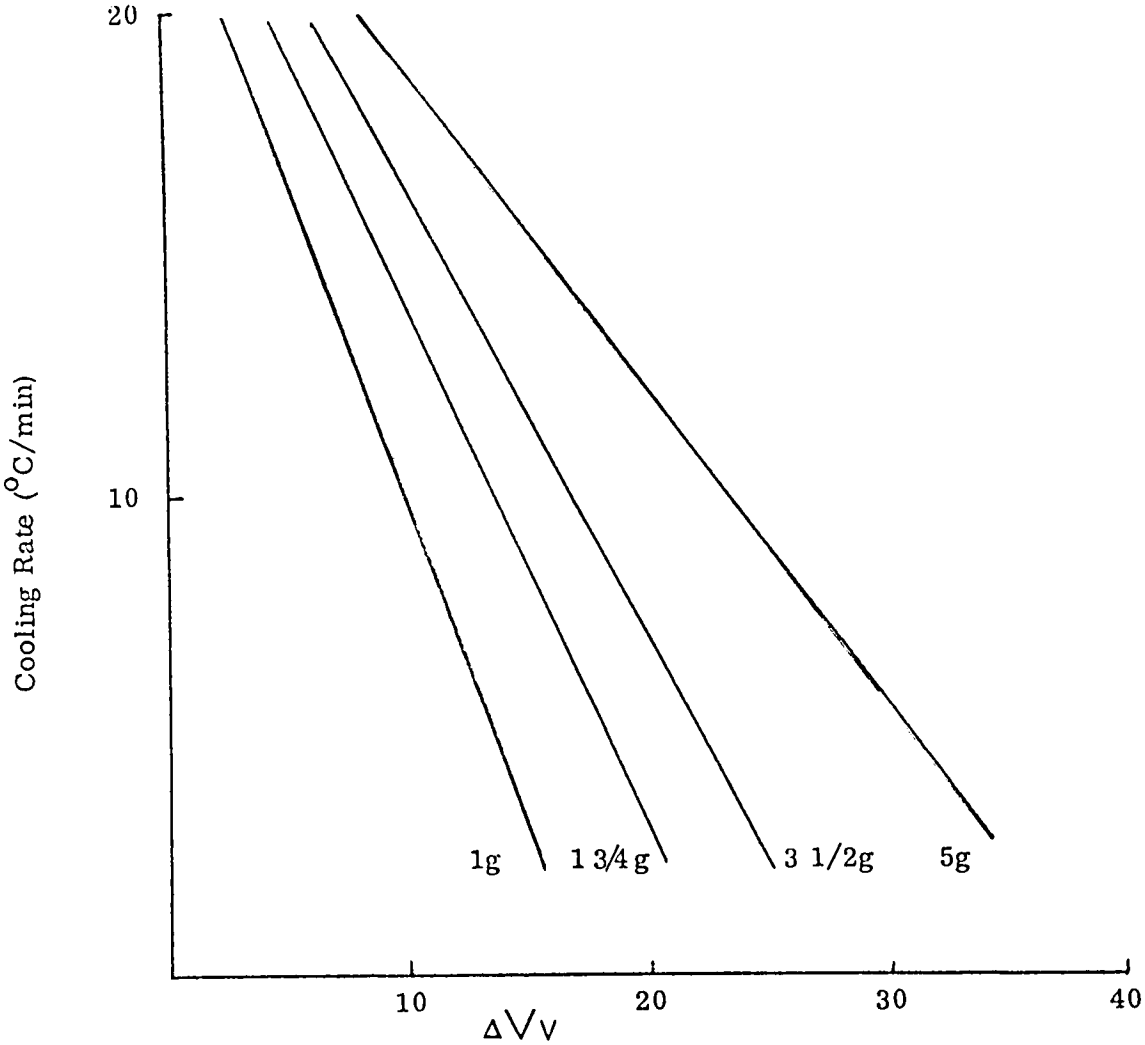

Figure 7. The Difference in Volume Fraction of Tin Dendrite Between the Top and Bottom of the Samples as a Function of Cooling Rate for Specific Accelerations

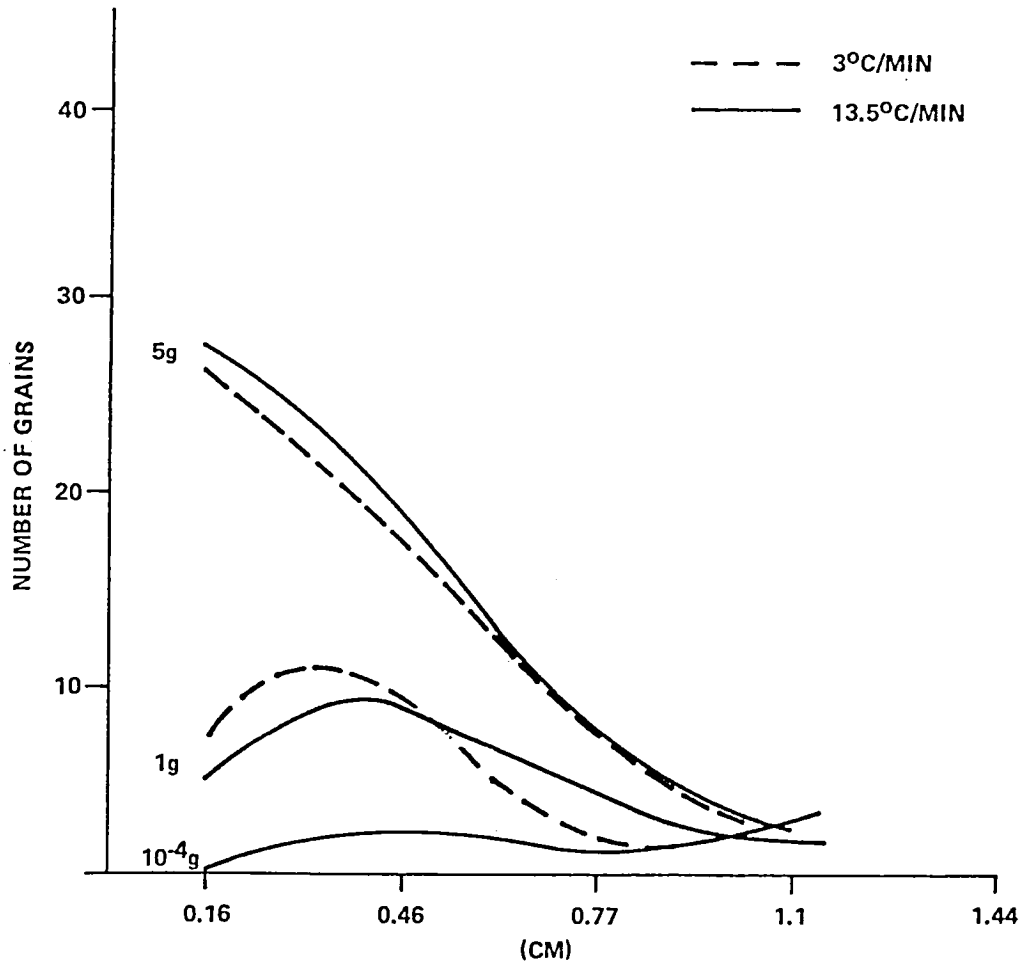

Figure 8. Bottom-Center Grain Size Distribution in Tin-15wt% Lead at Two Different Cooling Rates and Three Acceleration Levels

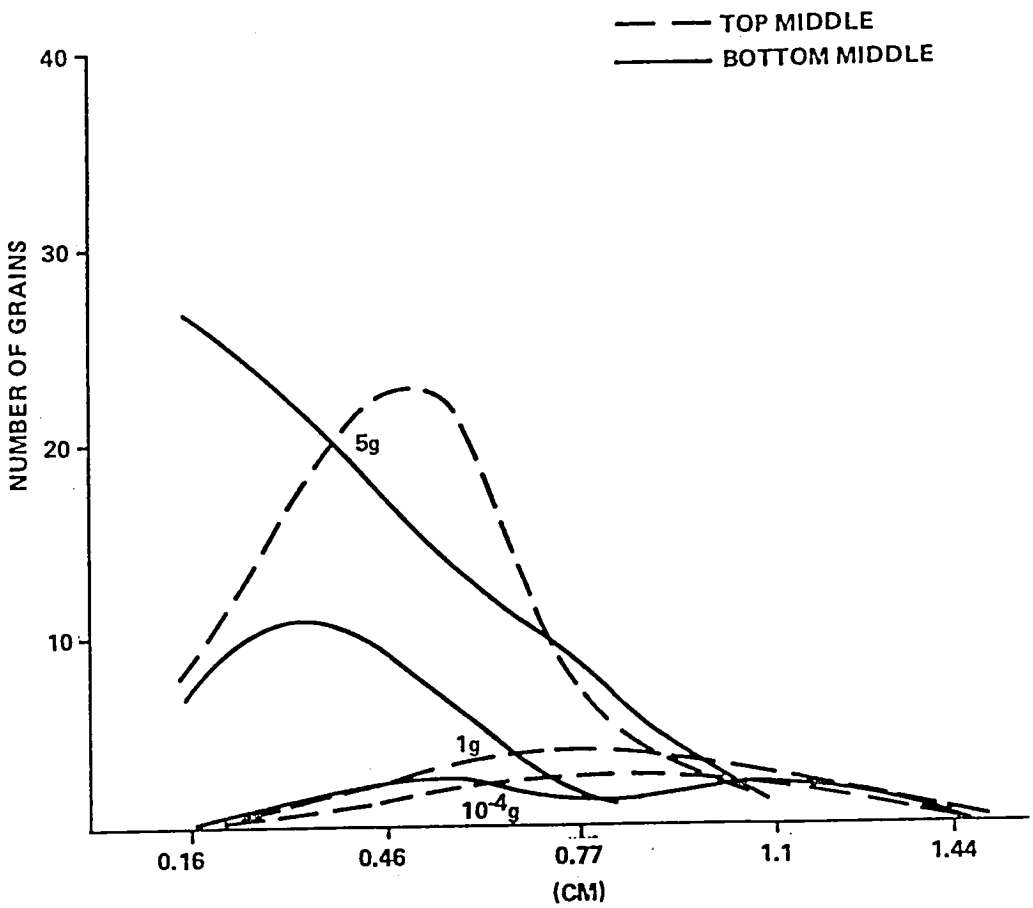

Figure 9. Grain Size Distribution in Tin-15wt% Lead, at Two Locations and Three Acceleration Levels, 3°C/Min Cooling Rate

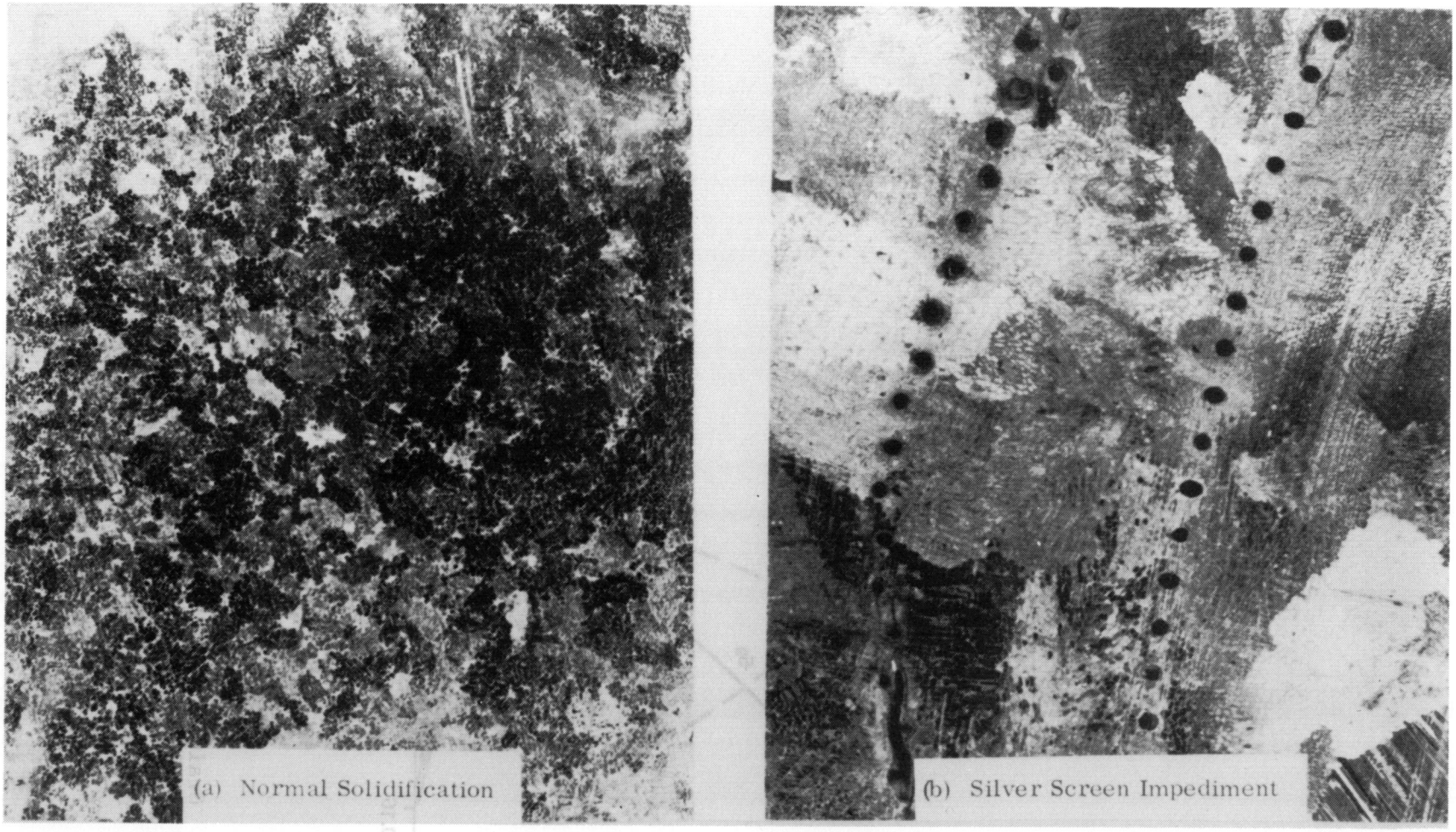

Figure 10. Cross-Sections of Samples Processed with and without Screen Impediment (Magnification level: 10X)

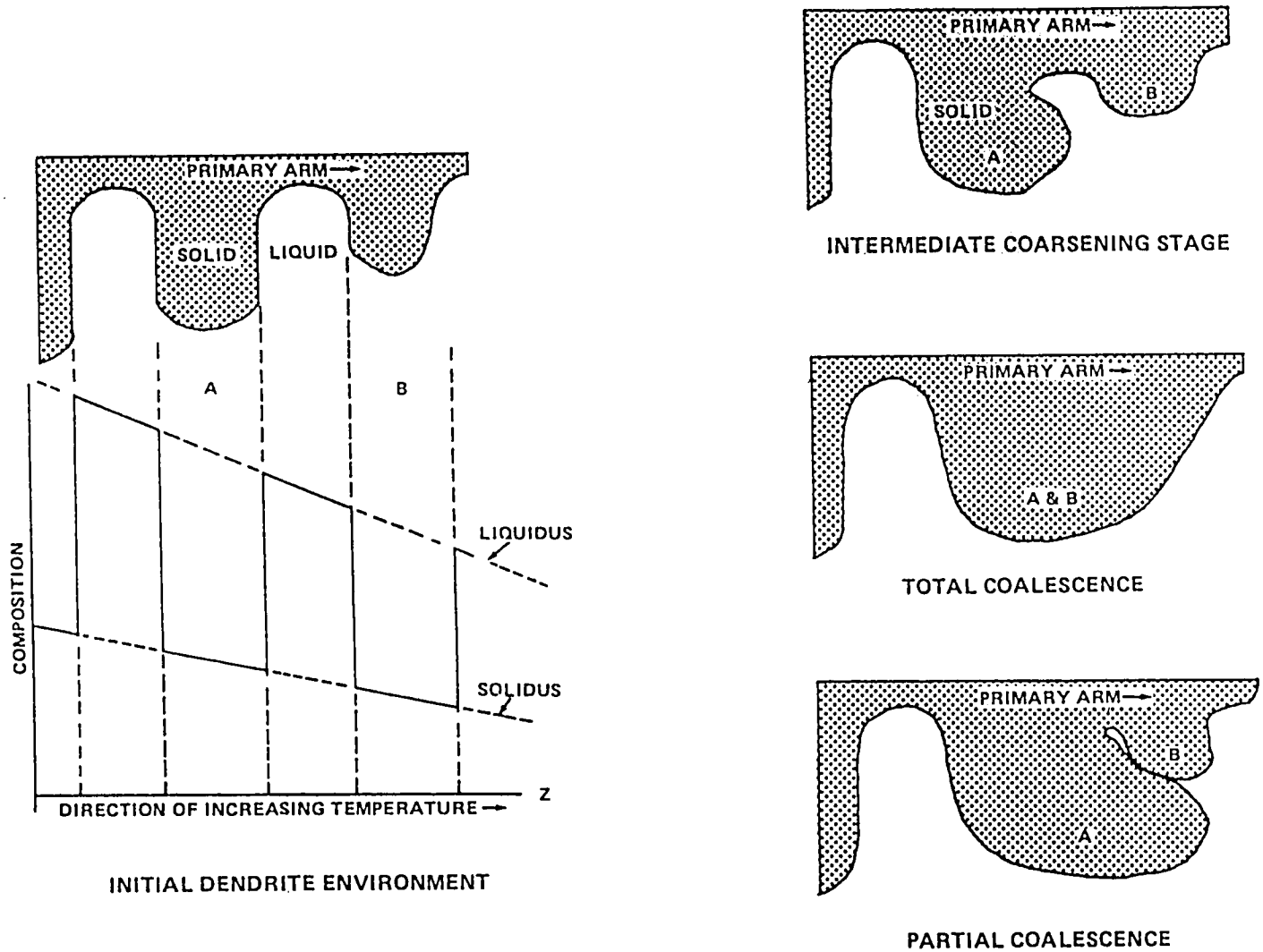

Figure 11. Dendrite Coarsening in a Temperature and Concentration Gradient

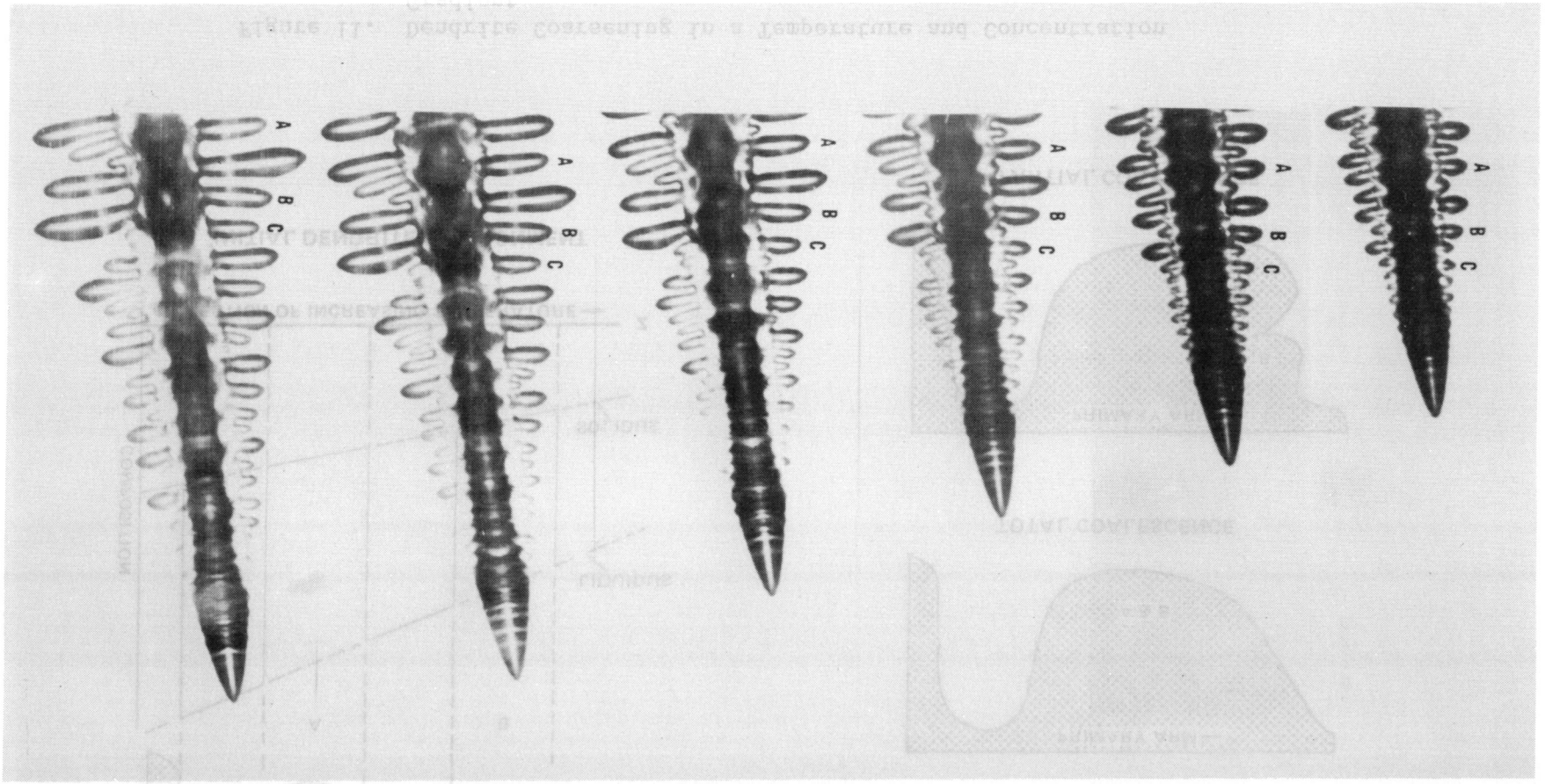

Figure 12. Solidification Sequence of Metal-Model Dendrite Showing Bulging and Coarsening (50X)

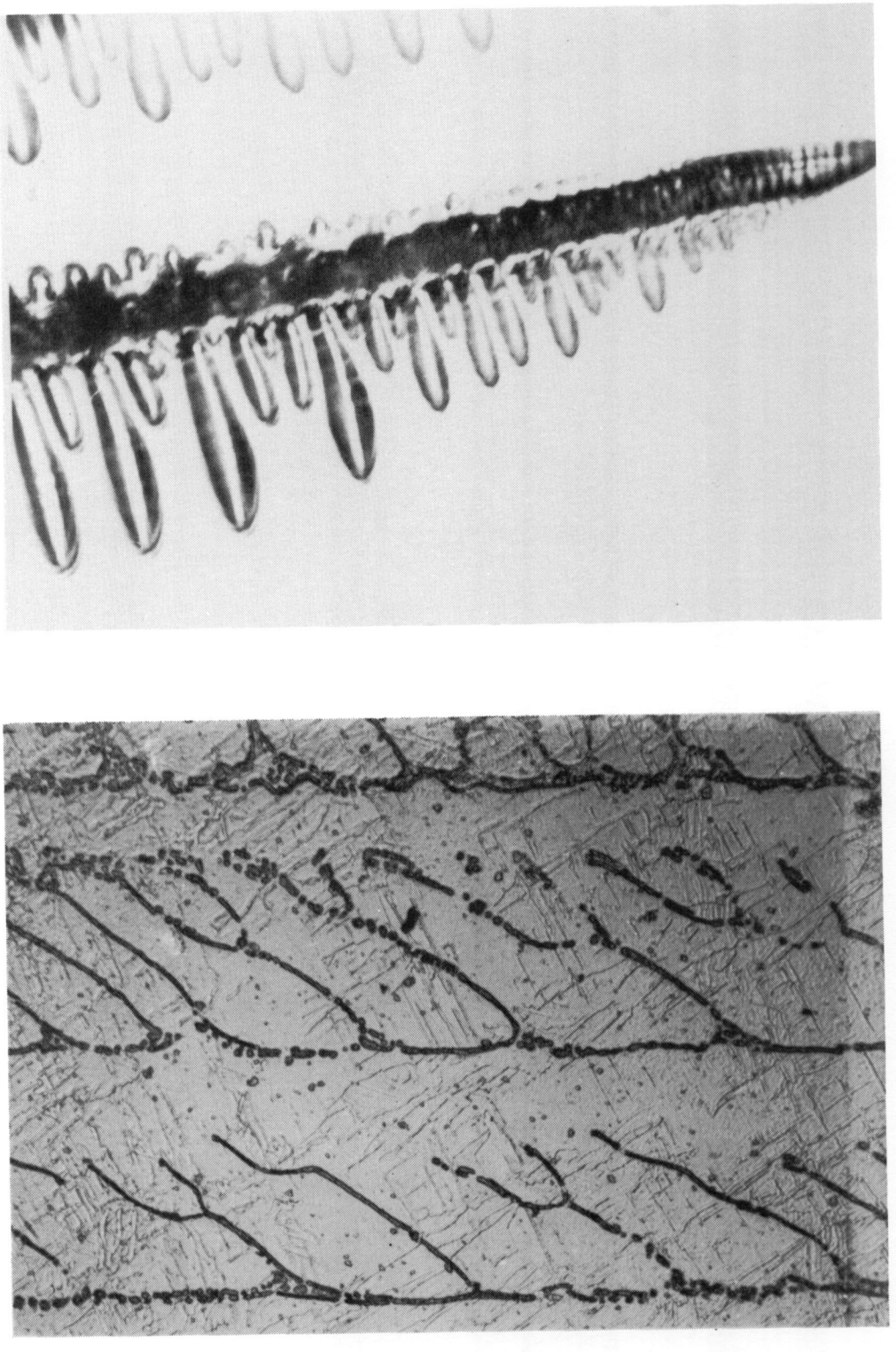

Figure 13. Flight Sample and Metal-Model Dendrites (50X)

CHAPTER IV

CONTAINERLESS PROCESSING TECHNOLOGY EXPERIMENT

DYNAMICS OF LIQUID DROPS

REPORT

SPAR VII EXPERIMENT 76-20/3

October 1981

A. P. Croonquist, T. G. Wang, D. D. Elleman, P. H. Rayermann

ACKNOWLEDGMENTS

The authors wish to thank L. Robinson, K. Tarver, D. Kerrisk, and H. Press of JPL for their valuable assistance in all phases of this experiment. The authors wish to thank R. Chassay, D. Schaefer and R. Fallon of MSFC for their contribution in this experiment.

This paper presents the results of one phase of research carried out at the Jet Propulsion Laboratory, California Institute of Technology, under Contract No. NAS 7-100, sponsored by the National Aeronautics and Space Administration

SECTION 1

INTRODUCTION

This report describes one phase of an experimental research program designed to contribute to the understanding of the fusion and mixing processes in the containerless processing of multiple samples. Study of the stability and manipulatability of liquid drops at room temperature is a useful and cost effective intermediate step in the development of a better understanding of the fluid physics pertinent to the mixing of two heated materials and the capability to produce alloys and amorphous materials in a zero-G environment. In addition the thermodynamics of chemical reactions can be studied by bringing two reactants together.

The primary goal of the experiment is to study three aspects of drop dynamics using containerless processing: the fusion and mixing processes, the shifts in the frequencies of the natural oscillations due to large amplitude effects, and the transport capability of the acoustic chamber for multiple drops.

The fusion process and the large scale response have been studied in ground based laboratories using neutrally buoyant systems to minimize the effects of gravity which would be appreciable on large samples.

The practical knowledge obtained in these rocket studies will aid in the design of a high-temperature system for containerless processing of materials in space. The study takes advantage of the laboratory work at JPL and zero-G aircraft tests as part of the overall Office of Applications Space Processing Program.

This experiment utilized an existing acoustic levitation rocket instrument which has been described in both the SPAR IV and SPAR VI 76-20 Reports with minor modifications.

SECTION 2

OBJECTIVES

The overall objective of this task is to study the containerless processing of materials in space. In containerless processing, most of the steps are conducted in the liquid-melt state. Our knowledge of the physical properties of liquid melts is only qualitative and empirical. The aim of this program is to gain a better understanding of the physics of liquid melts and the capabilities of manipulating them in a long-term, zero-gravity environment, thus aiding in the design of practical systems for space processing.

The primary objectives of this flight were to:

(1) Demonstrate the transport capability of the acoustic chamber for collision and coalescence of quiescent drops. The initial perturbation of the drops generated by the drop injection systems will be allowed to damp down. Quiescent drops will be transported to the center of the chamber for coalescence by the acoustic forces. This transport capability of the chamber and the possible perturbation on the drop shapes will be studied.

(2) Study the mixing effects generated by collision and coalescence of oscillating drops. Two oscillating drops will be made to coalesce at the center of the chamber. The mixing effects generated by the coalescence will be studied from the film record.

(3) Study the shift of natural frequencies of drop oscillation as a function of oscillation amplitude. The shift of natural frequencies of drop oscillation at large amplitude from those predicted at small amplitude has

been observed in a laboratory immiscible system. This experiment will allow comparison of values from zero-gravity and neutral-buoyancy systems.

SECTION 3

APPARATUS AND OPERATION

This experimental SPAR flight utilized an existing acoustic levitation rocket instrument, which had been flown on SPAR IV in June 1977[1] and on SPAR VI in October 1979[2]. The primary modification to the instrument was the addition of a multiple-drop injection system and a vacuum system to retrieve drops between experiments. This flight was the third in a series of four flights that are intended to study the dynamics of drops. The final flight is scheduled to take place in the latter portion of 1981.

A. Apparatus

Figure 3.1 shows the SPAR VII rocket payload 76-20 with the payload shell removed. The instrument consists of a triaxial acoustical levitation resonance chamber[3] which is used to position and control liquid drops in the low-G environment. This particular chamber is nearly cubical though the three dimensions were purposely made slightly different to preclude interference effects. The chamber's inside dimensions are 10.59 x 11.42 x 12.70 cm for the x, y, and z axes respectively. Three acoustic drivers are fixed rigidly to the center of three mutually perpendicular faces of the chamber.

During operation of the system, each driver excited the lowest-order standing wave along the direction that the driver faces. In a resonant system, the acoustic pressure is maximum at the nodes of the velocity wave and minimum at the antinodes; in this geometry the velocity nodes occur at the walls and the antinodes at the center of the chamber. When the chamber is

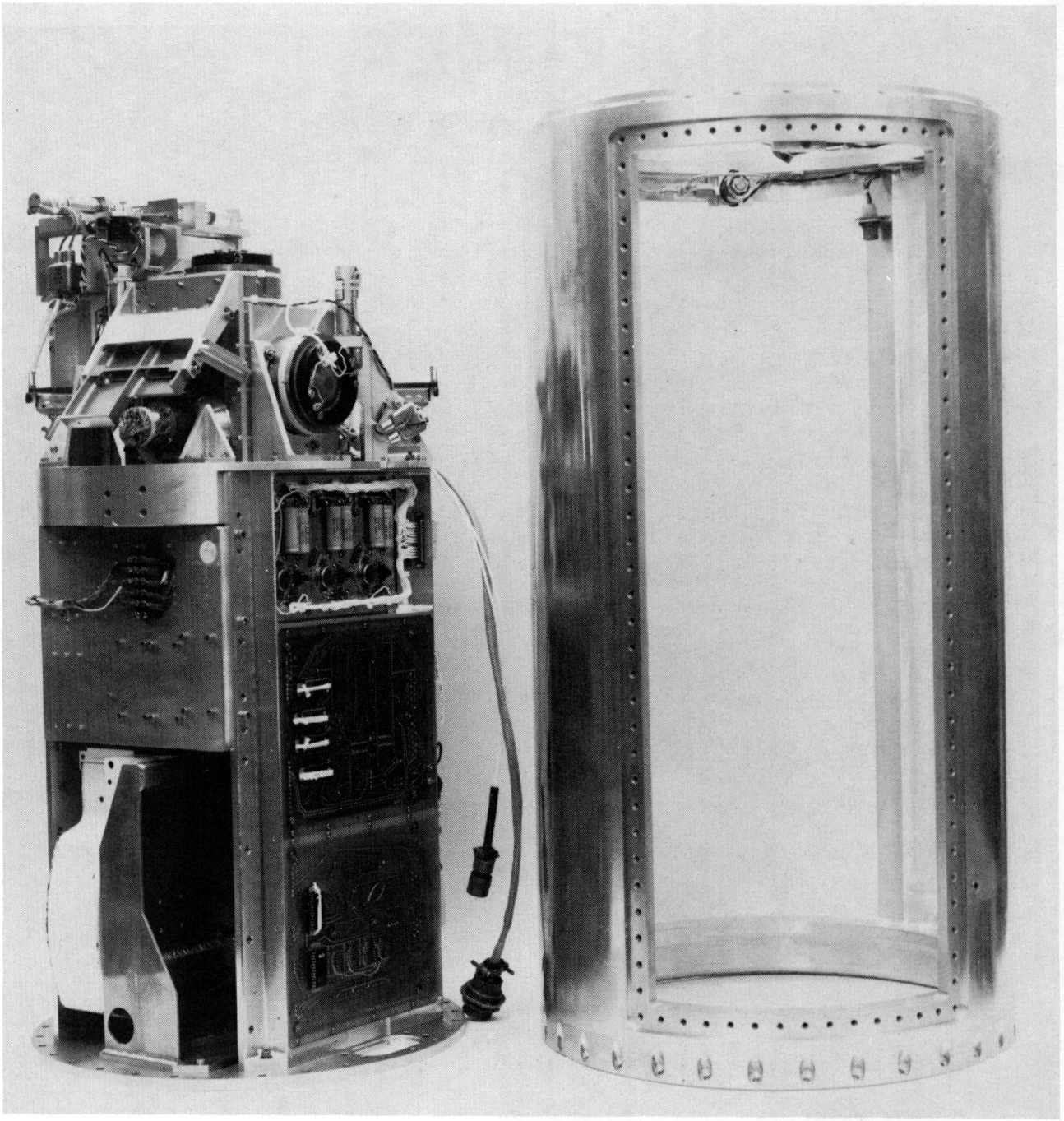

Figure 3.1 The SPAR 76-20/3 Payload Without and With Its Cover

used in its resonant mode, introduced liquids and particles tend to be driven toward the antinodes, where they collect and remain until the acoustic excitation is turned off.

Calculation of the acoustic forces on a single drop is simplified by the fact that the characteristic impedance of the liquid ρc ($\sim 10^5$ cgs) is very much greater than that of the gas $\rho_o c_o$ (~ 40 cgs): $\rho c/\rho_o c_o \sim 10^3$ where ρ and ρ_o are the densities of the liquid and gas, respectively, and c and c_o are the respective sound velocities. Because of this impedance mismatch, the acoustic power in the drop is three orders of magnitude smaller than that in the gas and can be neglected. This simplifies the expression for the radiation pressure $\langle \Delta P \rangle$, which is time-independent and is given at the boundary by

$$\langle \Delta P \rangle = (\overline{p^2}/2\rho_o c_o^2) - (1/2)\rho_o(\overline{\bar{u}^2}) \tag{1}$$

where p is the excess acoustic pressure, $\bar{u}$ is the gas particle velocity, and the heavy bars over p^2 and $\bar{u}^2$ denote time average of the quantities. Eq. (1) is the Bernoulli equation,[4] which gives the acoustical perturbation to the ambient pressure.

The pressure profile in this system can be derived as follows. The velocity potential φ of the wave in the chamber can be expressed as

$$\varphi = \varphi_x \cos(k_x x)e^{i\Omega_x t} + \varphi_y \cos(k_y y)\, e^{i\Omega_y t} \tag{2}$$

$$+ \varphi_z \cos(k_z z)e^{i\Omega_z t},$$

where $\varphi_{x,y,z}$ are the complex velocity potential amplitudes of standing waves of frequency $\Omega_{x,y,z}$ and wave number $k_{x,y,z}$. The particle velocity $\bar{u}$, by definition, is $\bar{u} = \nabla\varphi$. The pressure is given by $p = -\rho\dot{\varphi}$. With only one of the three drivers on ($\varphi_x = \varphi_y = 0$), the resulting expression for the

radiation pressure is

$$\langle \Delta P \rangle = \rho_o k_z^2 p_z^2 \cos 2k_z z \qquad (3)$$

In this situation the pressure node is a plane ($z = L_z/2$), which becomes a point when all three drivers are turned on. This has been verified experimentally.[5] Because this is a three-dimensional system with independent control on each dimension, it has a great deal of versatility. It can position a drop acoustically and then manipulate it by inducing either drop oscillation or rotation. The addition of a second drop is assumed to perturb the acoustic forces to only a slight degree so that the formalism developed for a single drop would be equally applicable to a double drop system. To date there has been no experimental evidence to indicate that the force on both of the drops varies significantly from Equation (3).

The primary source of data from this experiment was cine film obtained with a 16 mm camera. The camera is directed along the z axis, two mirrors giving nearly orthogonal views along the x and y axes. In addition the sound intensity at each wall, the camera lighting and deployment system status, the frequency of the z axis signal and the ambient pressure were monitored, telemetered and recorded. A portion of the MSFC accelerometer data was supplied to aid in the JPL analysis (see Figure 3.3). The x, y, and z axis accelerometer data is coaxial with the x, y, and z axes of the acoustic chamber, the view of the camera for each of the axes is from the positive axis to the negative axis of the accelerometer.

B. Operation (Coalescence and Mixing Experiments)

This section gives the operating characteristics of the acoustic chamber

required to conduct the experiments.

(1) The liquid used in this experiment was distilled water with small quantities of red and green dye added to each drop to provide optimum contrast between the two fluids. The surface tension of the dyed water was measured before the flight and was found to be 71.0 $\pm$ 2.0 dynes/cm. The water was deployed through two forked syringes so as to form two drops near the center of the chamber with one arm of the forks acting as a post and the other one, which was hollow, acting as the conduit for the liquid. The posts were necessary so that the drop would remain close to the center of the chamber when the two forks were retracted. The 4.6 cm^3 for each drop were injected over 13 seconds. The acoustic drivers were turned on just after retraction providing positioning forces as the injector tips were withdrawn.

(2) Assuming that the sample to be studied is a water droplet with radius, a = 1.30 cm (which corresponds to the coalesced drop), that the residual acceleration it feels is $10^{-1} cm/sec^2$ ($\sim 10^{-4} g$), and that the quality factor, $Q = \Omega/\Delta\Omega$, of the acoustic chamber is 25, Newton's equation of motion for the drop in the acoustic field is

$$\int \langle \Delta P \rangle n_z dA = (4\pi/3) a^3 \rho\, 10^{-4} g.$$

In the limit of $ka \ll 1$, this has been calculated by King[6] to be

$$(5\pi/6)(ka)(p^2a^2/\rho_o c_o^2) \sin 2kz = (4\pi/3)\rho a^3\, 10^{-4}\ g. \qquad (4)$$

For a 2.6 cm diameter sphere of density 1 g/cm^3, the corresponding minimum acoustic pressure required to position the drop is $p \sim 10^3$ dyn/cm^2 $\sim$ 134 dB, where the decibels are measured against the reference pressure 2×10^{-4} dyn/cm^2. For a 50% efficient compression driver, less than 0.2 W of electrical power is needed to provide the required acoustic pressure. It is worth pointing out that at this acoustic pressure level F_s, the surface tension

force, that acts on the water drops is two orders of magnitude larger than F_a, the acoustic force: $F_s/F_A = (2\pi r\sigma)/(\int \langle \Delta P \rangle n_z dA) \sim 100$.

(3) If the amplitude of the acoustic wave is modulated at the frequency Ω_m, the drop experiences a modulated force $F_m = \int \langle \Delta P \rangle_m \, n_z \, dA$. When Ω_m matches the frequency of maximum response, which is slightly less than the frequency of the normal modes of oscillation of the drop, ω_n, where

$$\omega_n^2 = n(n-1)(n+2)\ \sigma/\rho a^3, \tag{5}$$

the response amplitude can be as large as $|A_n| = |F_m/(\Omega_m M_d\ \beta_n|$, where β_n is the damping constant of the nth mode of the drop, and M_d is the mass of the drop. For the n=2 oscillation mode, $A_2 \sim 1$ cm when the SPL is 134 dB and the acoustic pressure is being modulated at 30%. Since the radius of the combined drop is 1.30 cm, even this small modulation force is sufficient to drive the drop into large amplitude oscillation at the fundamental frequency. However, larger amplitude modulation is required to stimulate large responses in the higher modes because of the increase in damping. That there is sufficient power to stimulate this very large amplitude response has been demonstrated in KC-135 flight experiments: the prototype chambers have been able to shatter water drops of roughly the same radius in less than 1 second when modulating at the drops' fundamental frequency.

C. Instrument Calibration

(1) Acoustic Calibration

The calibration of the acoustic intensity was difficult to accomplish because the instrument did not have calibrated microphones in the chamber. Because the primary interest was not in the sound intensity itself but in the positioning force produced by the acoustic standing waves, the acous-

tic intensity was calibrated by measuring the acoustic positioning force itself. The force measurement was performed by suspending a low density (styrofoam) sphere (.229g mass, 1.25cm radius) 3.175 cm from the center of the chamber on a thin string 5.08 cm long (see Figure 3.2). The signal to each speaker was adjusted so that the acoustic force deflected the sphere 0.115 in. (0.292 cm) toward the center of the chamber. This corresponded to a force of 12.9 dynes. The signal level to each of the speakers was preset so that the acoustic centering force would be 25.8 dynes for the entire flight.

(2) Liquid Volumetric Calibration

The liquid deployment system was tested before the flight by taking repeated volumetric measurements of the deployed liquid. There was a variability of several percent in these measurements caused by backlash in the gear system that drove the syringe system. Typical measured volumes were 9.2 $\pm$ 0.1 cm^3 for the combined drops.

(3) Sequence and Time Line Calibration

The program had been run through the flight sequence over 100 times in pre-flight tests. No deviation from the programmed sequence was observed in these tests. In addition, flight telemetry confirmed the sequence operated as programmed during the flight.

(4) Cine Camera and Lighting Calibration

Camera, lighting and film tests were run before the flight. The quality of test images was confirmed by the PI and CoI to be acceptable for data analysis.

ACOUSTIC FORCE CALIBRATION

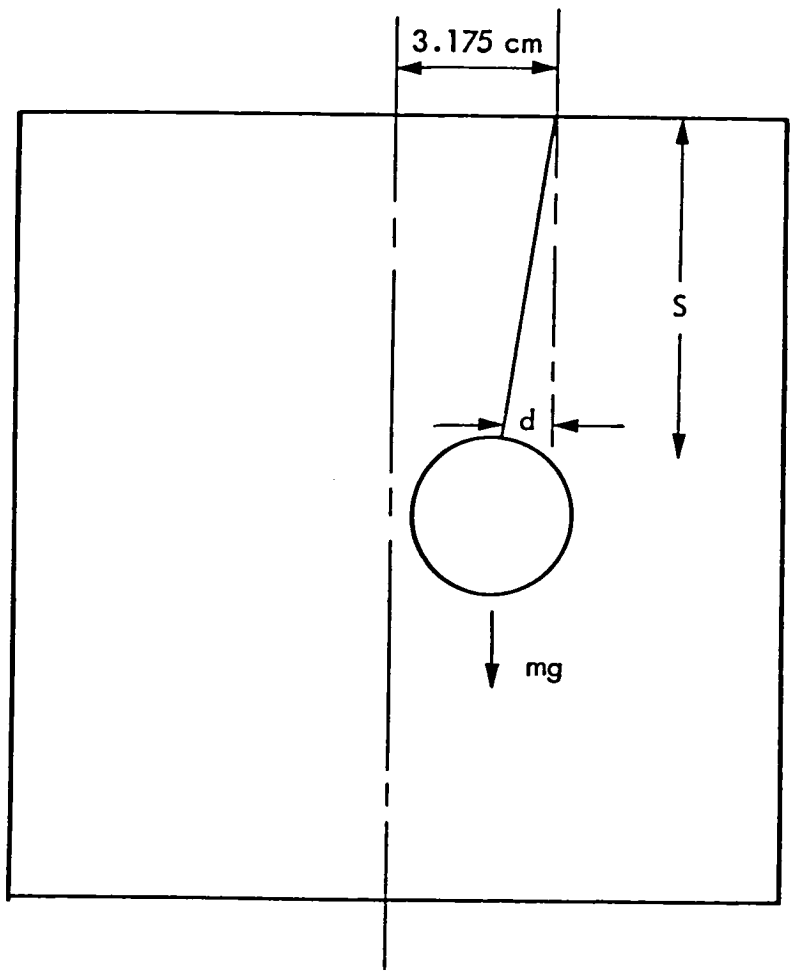

ACOUSTIC FORCE $F_A = mg \frac{d}{S}$

Figure 3.2 Calibration of the Sound Pressure Level Inside the Acoustic Chamber by Balancing Acoustic and Gravitational Forces.

D. Flight Experiment

(1) Pre-flight Preparation

The JPL experiment 76-20 was flown on SPAR VII on May 14, 1980. Pre-launch testing of the instrument indicated all systems were functioning and ready for flight.

On the morning of the flight of SPAR VII the PI was informed by Roger Chassay of MSFC that there were several options available to the PI for obtaining an optimum low-gravity platform from the SPAR rocket. We could choose not to use the stabilization system, i.e. not fire the small control jets, and hope that the rocket experiment package did not tumble or rotate too fast, or we could refrain from using the stabilization system until acceleration forces exceeded some predetermined range and then activate the system. It was decided to go with the second option.

(2) Telemetry Analysis

An analysis of the telemetry data from the JPL SPAR VII 76-20 experiment indicated that the system functioned according to the pre-launch timeline that had been programmed into the instrument. All subsystems on the instrument operated as commanded by the programs. In addition, postflight tests and operation of the instrument indicated that the instrument functioned according to the programs and, in fact, it was still in operating condition after the flight.

(3) Acceleration Forces on the SPAR Platform

Figure 3.3 shows the accelerometer data supplied to JPL by D. A. Schaefer of MSFC on 7/2/80. As can be seen in the data, several spikes occured along the x and y axes during the time of deployment of the first experiment. The largest spike was approximately 100μg and lasted for roughly

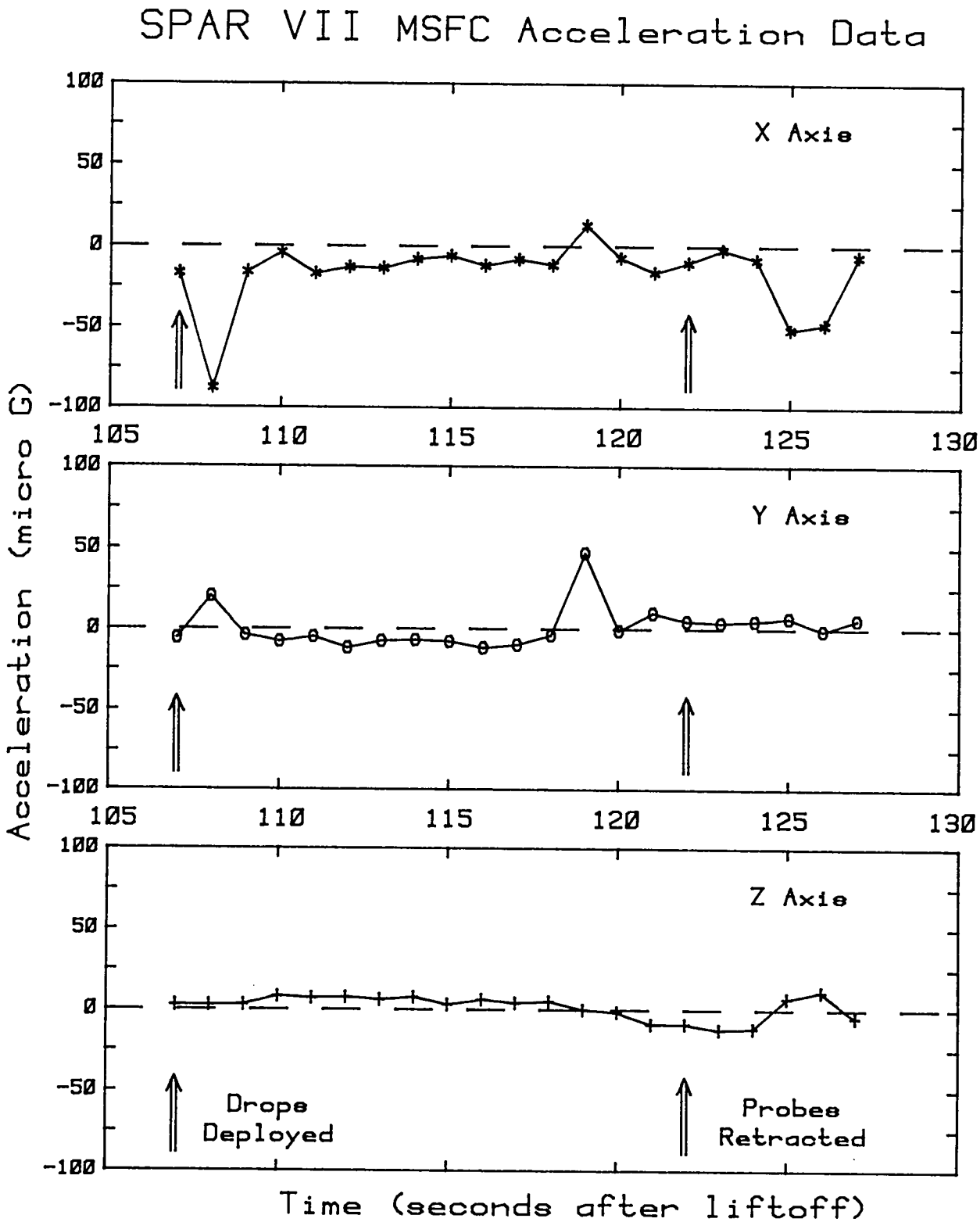

Figure 3.3 Accelerometer Data During the Deployment of the Drops of the First Sequence. This Telemetry Data Is Courtesy of D. Schaefer, MSFC.

two seconds. The acceleration force that occurs at 108 seconds ALO produced unwanted motions of the drops in experiment 76-20. This motion strongly affected the outcome of the experiment because it occurred at the most critical time just before probe retraction when the drops were full size and attached to the forked probes with no acoustic force to stabilize them.

(4) Deployment of the Multiple Drops

In Experiment 76-20/3, four similar experimental sequences were programmed: the simultaneous deployment of two water drops and their collision and coalescence as a result of the acoustic forces. The differences between the sequences involved modulation of the drop or droplets to vary the initial conditions.

The G-bump described above caused the drops to move down the posts (i.e. the nonhollow arms) of the forks dring the first sequence. When the probes were retracted the drops followed the probes to the corner. In the second and third series the red drop was successfuly deployed but the green drops slid down the post as the post had been wetted inadvertently during deployment of the previous sequence and were carried to the corner. In the final sequence the two drops were successfully deployed although their volumes were less than the preprogrammed ones because of residual water on the forks.

Because the drops were not centered in the chamber during deployment, they oscillated within the acoustic potential well. The acoustic force was sufficient to hold the drops and prevented them from contacting the container wall and in addition brought them together to coalesce. The motions caused by the acoustic restoring force are found to be consistent with what has been observed and reported in the SPAR VI Report[2].

(5) Objective Accomplished

The minimum acceptable success criteria for this flight were to:

i) Demonstrate the deployment and coalescence of multiple drops.

ii) Study mixing caused by that coalescence.

iii) Study the shift in frequency of large amplitude natural oscillations.

These objectives have been partially, but not satisfactorily, met. In only one of the three sequences did the two drops deploy and then coalesce. However, because that deployment was flawed, the coalescence of the drops was violent, precluding study of the development of the interface and mixing which were too quick to analyze from the film record. In addition, the shift of the natural oscillation frequency as a function of amplitude was not observable due to the presence of many modes generated by the energetic collision.

SECTION 4

DATA ANALYSIS

A. Introduction

The programmed timeline was as follows:

Time (sec ALO)	Event
97	Camera turned on
107	First set of drops deployed
122	Probes retracted, sound on
155	Sound off, drop removed
170	Second set of drops deployed
185	Probes retracted, sound on (MOD on)
194	MOD off
220	Sound off, drop removed
233	Third set of drops deployed
249	Probes retracted, sound on
260	MOD on
284	Sound off (MOD off), drop removed
299	Fourth set of drops deployed
314	probes retracted, sound on (MOD on)
344	MOD off
440	Sound off, camera off.

Analysis of the cine film indicated that the experiment adhered to this timeline.

During the first test sequence two quiescent drops were to collide and coalesce under the influence of the acoustic centering forces only. There occurred two G-events during deployment at 108 and 119 seconds ALO (see Fig. 3.3). At 108 seconds the drops which were just being injected hardly responded to the spike while 11 seconds later they moved sharply from their respective positions on the tipss of the forks to final resting positions near the center of the injector forks. Because the droplets were very small during the first event the inertial forces were less than the forces of adhesion and the perturbation was correspondingly small. In contrast the almost fully deployed drops (see Fig. 4.1) were very vulnerable to such acceleration spikes during the time of the second bump because the adhesion forces were no larger but the mass was several orders of magnitude greater. Because of this second bump each drop contacted only one injector when they were retracted and, as a result, the drops were given a non-zero momentum and followed the probes to the corners of the chamber. No information on the behavior of free drops was obtainable from this sequence.

During the second sequence modulation of the acoustic signal along the z axis started at deployment: it was intended to stimulate oscillations in the drops before they coalesced. The acoustic force along that axis was modulated (with an index of 15) and its frequency was swept over a range which included the expected frequency of the n=2 mode of the drops' natural oscillation, 3.6 Hz. Because the forks had been wetted during the first sequence, the green drop migrated down the post arm and only the red drop was deployed as a free drop. It was held by the acoustic forces and appeared to respond to the modulating force. Because the drop was not in the path of the ejector jet when it was turned on (and the sound turned off) at 220 seconds, it was not

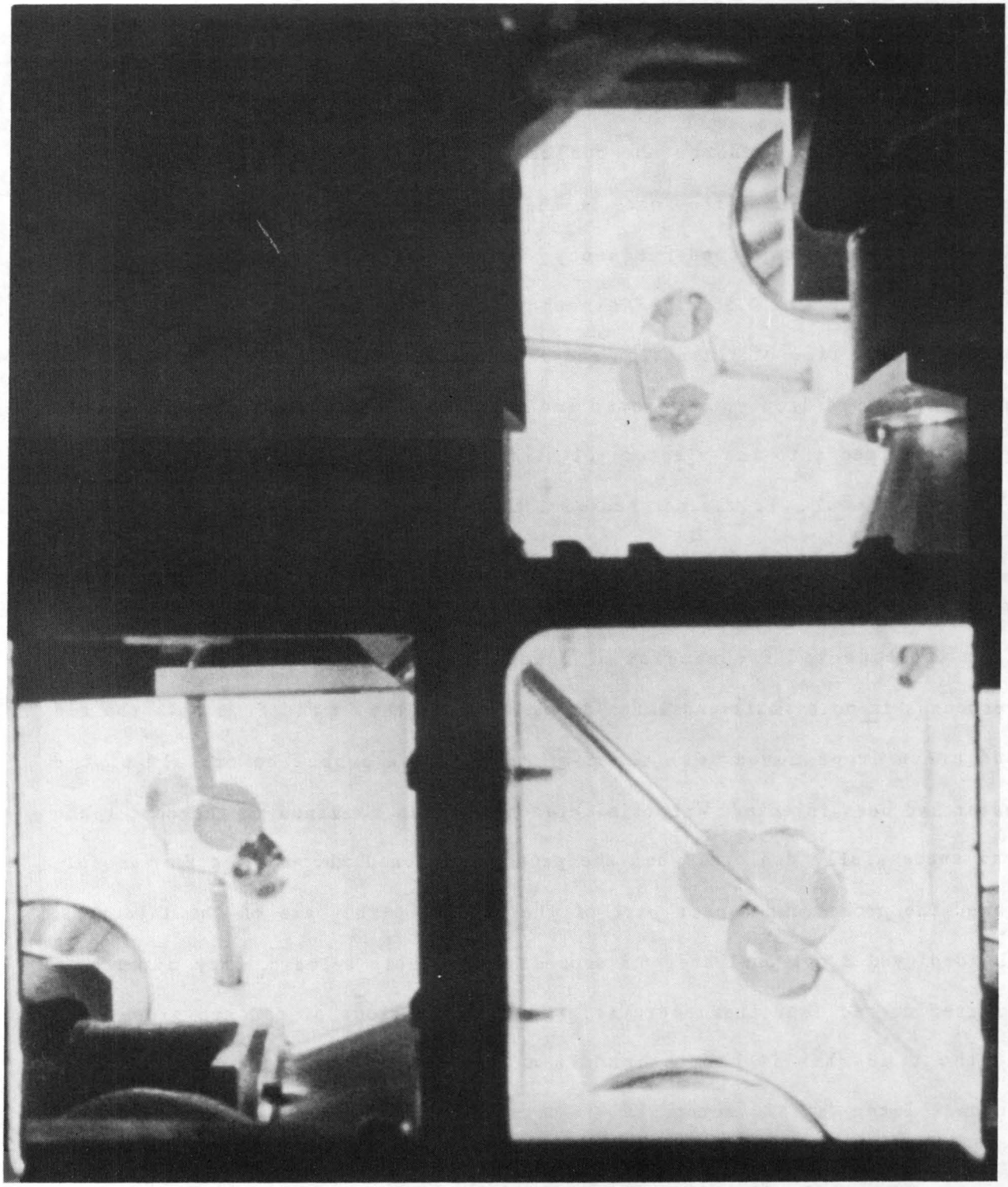

Figure 4.1 An example of the format of the 16 mm data film. This frame shows the beginning of the motion caused by the g-bump at 119 seconds ALO. The main view which was used in the data analysis is located in the lower right.

removed from the chamber by the jet/vacuum system as desired but drifted until it hit a wall.

In the third sequence the coalesced drop was to be stimulated by the modulation of the acoustic force in the z direction which was swept from 3.0 Hz to 4.0 Hz. The expected frequency of the n=2 mode of oscillation for the coalesced drop was 2.56 Hz. Again the green drop was not centered on the probes at the time of retraction and as a result followed the injector to the corner. The red drop was deployed and held. When the acoustics were turned off it drifted into the ejector jet stream near the nozzle and was pushed to the opposite wall. It was not sucked into the vacuum hole.

In the final sequence both the deployed drops and the coalesced drop were subject to a force which was modulated at 4.9 Hz. This was far enough from the expected frequencies of resonances to allow study of the forced responses in both small and large drops. Some of the liquid from both the red and green drops moved down the post arms of the probes before all of the water had been injected. Water injected after this remained in the center and was successfully deployed when the probes retracted whereas the former followed the probes and became part of the puddle at the base of the injectors. The deployed drops coalesced 6.3 seconds after their release. They mixed to a limited degree, but there were still definite regions of red and green even at the time when it hit the puddle at the base of one of the probes 100 seconds later (at 420 seconds).

B. Study of the Frequencies of Natural Oscillation

Given the programmed volumes of 4.6 cm^3 and 9.2 cm^3 for the deployed droplets and coalesced drop the frequencies of the lowest mode of oscillation

for small amplitude motion, f_2, were 3.62 Hz and 2.56 Hz, respectively. From laboratory observations[7], the expected shift in frequency for large amplitude motion was negative: the larger the amplitude of the motion, the lower the frequency of those oscillations. larger.

During the second and third sequences the full 4.6 cm^3 of the red drop appeared to be deployed. Cursory analysis revealed that they appeared to respond at f_{mod} ~ 4.1 and 3.0 Hz. These do not correlate well with the frequency expected for the apparant volumes deployed (i.e. 3.6 Hz). They probably reflect the interaction of the natural oscillations and the forced reponse.

In the final experiment both red and green drops were successfully deployed but with volumes less than intended. As in the previous sequences for the green liquid, some of the deployed liquid ran down the arms of the forks. Visual inspection indicated that roughly 30% and 55% of the green and red liquid were deployed as free drops.

By studying the changes in dimension and position of the minimum rectangle enclosing the drop (see Figure 4.2), information about the behavior of all three drops was obtained. The BOX method was designed to help analyse the data from Drop Dynamics experiments flown on the various SPARs and the KC-135 zero-gravity aircraft for which the information of interest was contained on 16 mm cine film. A Vanguard Motion Analyser is used to examine the film one frame at a time. It is a simple matter for the operator to determine the four points required to describe the minimum box for each boundary and to read the time after launch from the information on the edge of the film. The virtue of this procedure is the speed and ease of data acquisition and its main drawback is the simplicity of the algorithm used. If the boundaries are describ-

The BOX Method

By finding the smallest rectangle with vertical and horizontal sides that encloses the drop images, a simple picture of the drop's oscillations and center of mass motions can be deduced from analysis of the series of boxes. A 16 mm Vanguard Motion Analyser is used to quickly determine the minimum box by moving crosshairs until they are tangent to the drop. Timing information included beteween the sprocket holes of the film is partially visible and permits the positive identification of a particular frame. This process is represented by the following sketch:

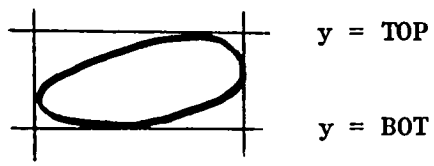

The four coordinates - LEFT, RIGHT, BOT and TOP - can be combined in several ways to enhance certain features of the drop's behavior. To study the motion of the drop in the acoustic potential well in the x direction, the function X = LEFT + RIGHT is used. In a similar fashion, Y = BOT + TOP can be used to study the y motion. (N.B. because the time periods analysed were so short in this study, meaningful center of mass data were not obtained.)

To study the oscillations of the drop there are again several ways to combine the four values. To see what frequencies the boundaries are oscillating at, the vertical or horizontal modes, with V = TOP - BOT and H = RIGHT - LEFT, are useful. To minimize the effects of bulk motion of the drop along the direction of viewing, one can study D = V - H, the difference mode. Conversely if the line of sight is an axis of symmetry for the drop, then the sum mode, S = V + H, will help highlight the oscillation.

The main virtue of this scheme is the simplicity and ease of data acquisition. However this simplicity limits the kinds of shapes that can be studied with confidence to those that are themselves simple. Theless elliptical the boundary, the less meaningful the data. This problem is particularly acute when studying the drop's behavior just after its deployment.

Figure 4.2 The BOX Method Was Used Throughout This Experiment to Study the Behavior of the Various Drops.

able by a series of ellipses this technique is quite powerful but if the shapes are more complex (e.g. if there is extreme local curvature) the simple algorithm is inadaquate to help the analyst isolate the component oscillations and/or rotations responsible for the more distorted shape.

Both the deployed drops and the coalesced drop underwent large amplitude oscillations. In an attempt to identify a known quantity from from the results, it was decided to locate the drops' responses to the modulated force. The sum mode of BOX was used as it should highlight such a signal: when viewing the drop along the z axis, the axis along which the force is being modulated, the size of the responding drop should appear to change at the same frequency. In the sum mode the vertical and horizontal dimensions of the box are added so that if the drop does oscillate in response the frequency of the driving signal should be apparant from the frequency domain results.

Examination of the data for the three drops (red, green and coalesced) indicated that there was a definite oscillation near the expected frequency in the case of the red drop but the signals for the other two drops were too complicated to identify any structure near that frequency. Figure 4.3a shows the strong signal at 4.94 Hz from the red drop and 4.3b the comparable signal from the coalesced drop.

When a distorted shape is rotated the BOX method will indicate the rotation by a peak located at twice the rotation rate if the dimemsions of the drop are used for the analysis or at four times the rate if the sum mode is used. When the drop is oscillating about one axis and rotating about another the expected oscillation peak will be split into two peaks seperated by twice the rate of rotation. Taking this into consideration it would appear that the various drops were rotating. It was possible to visually confirm

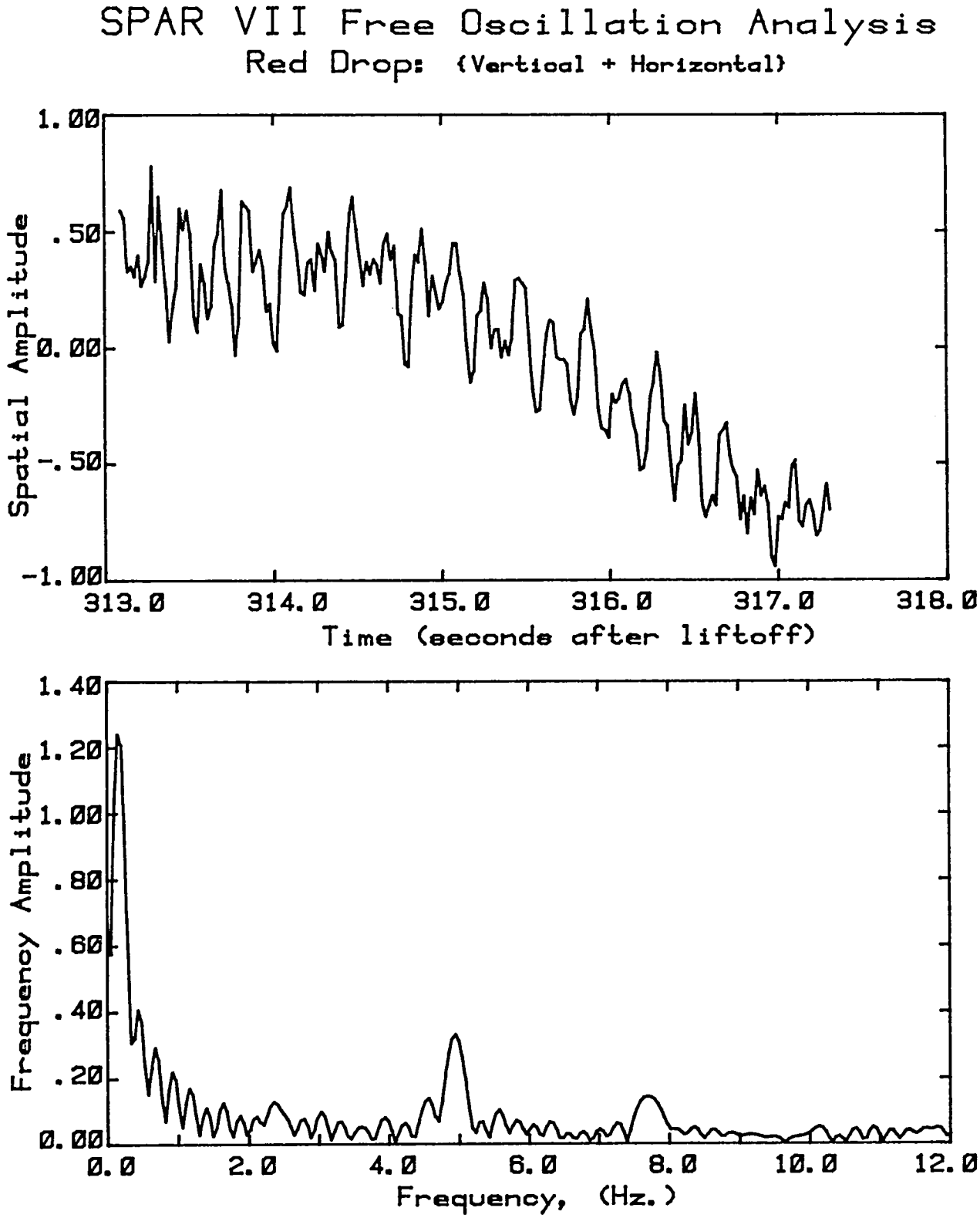

Figure 4.3a The Sum Mode of BOX Was Used to Isolate the Red Drop's Response to the Modulated Force at 4.9 Hz.

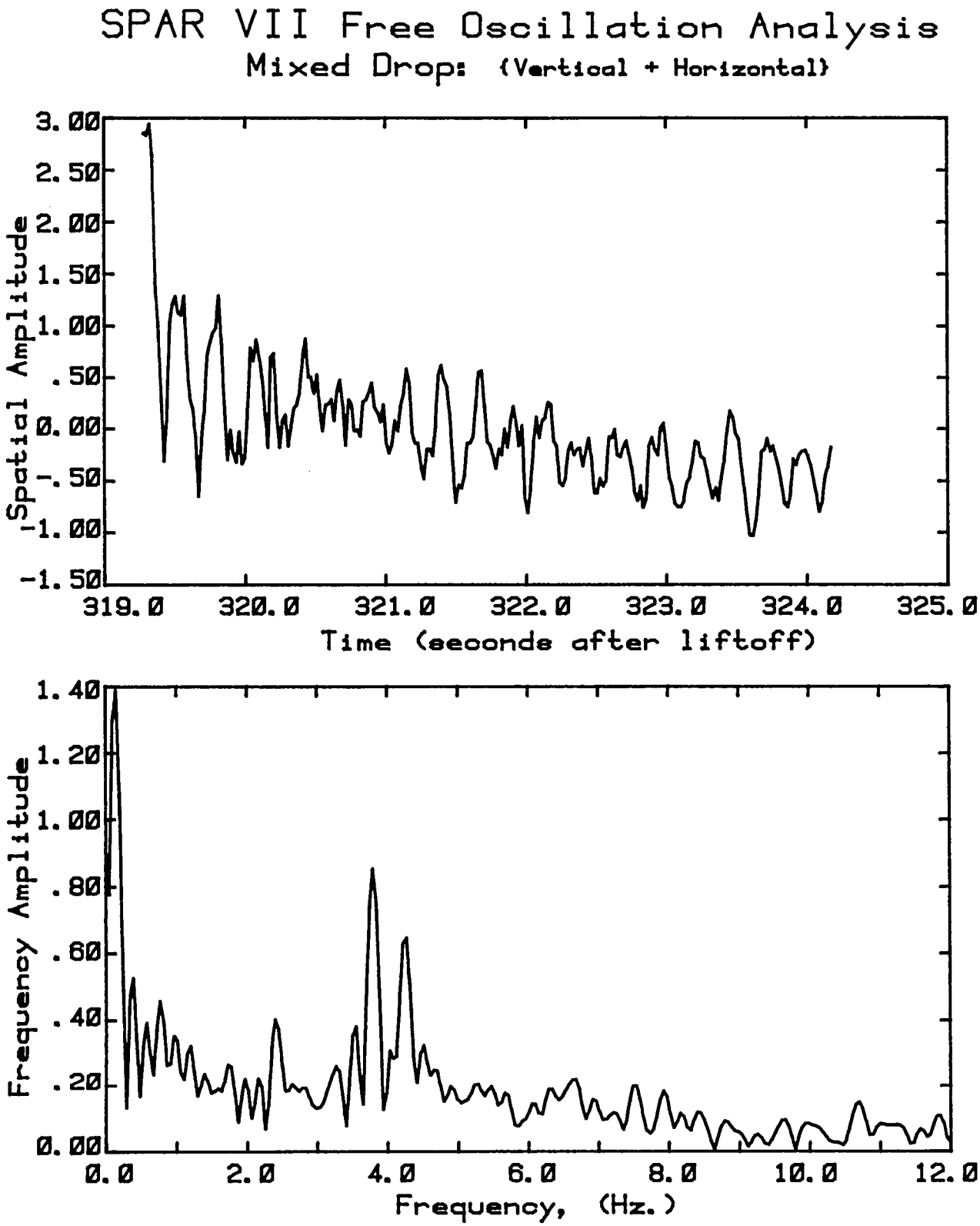

Figure 4.3b The Sum Mode of BOX Was Used to Attempt to Isolate the Coalesced Drop's Response to the Modulated Force at 4.9 Hz. It Was Not Successful.

this rotation only in the mixed drop because the boundary between the two fluids was clear. This observation indicated a rate of 0.98 rotations per second about the z axis right after coalescence which decreased to .72 rps just before the drop hits the wall. The quality of the image in the other two views was not adaquate to allow the observation of any rotation. The effect of this rotation would be to split any oscillation peaks by $\pm$0.90 Hz.

Because the full volumes were not deployed and there was insufficient time for the oscillations to damp out for the small drops it was impossible to isolate the natural oscillation frequency for small amplitude motion and to make a comparison with the theory for large amplitude oscillation. Despite not knowing the volume of the coalesced drop a measure of the small amplitude behavior could be obtained from the latter half of the experiment in which the amplitude of oscillation had decreased from that at the time of coalescence.

Using vertical and horizontal mode data, the relative radii were determined from the mean value of the two dimensions for each drop. Without correcting for the distances of the drops from the camera, the relative radii of the red, green and mixed drops were 4.73, 3.40 and 5.27. These correspond to relative volumes of 106, 39, and 146. These manipulations were important because the spectra obtained showed structure which was not clearly interpretable which made it quite difficult to positively identify a peak as the frequency of the n = 2 mode of oscillations.

Study of the mixed drop spectra showed two dominant peaks at roughly 2.5 Hz and 4.2 Hz (see Fig. 4.4). If either of these corresponded to the n = 2 mode of oscillation, they would indicate drop volumes of 9.2 cm^3 and 3.4 cm^3. The former is too high and the latter too small to be credible. More accept-

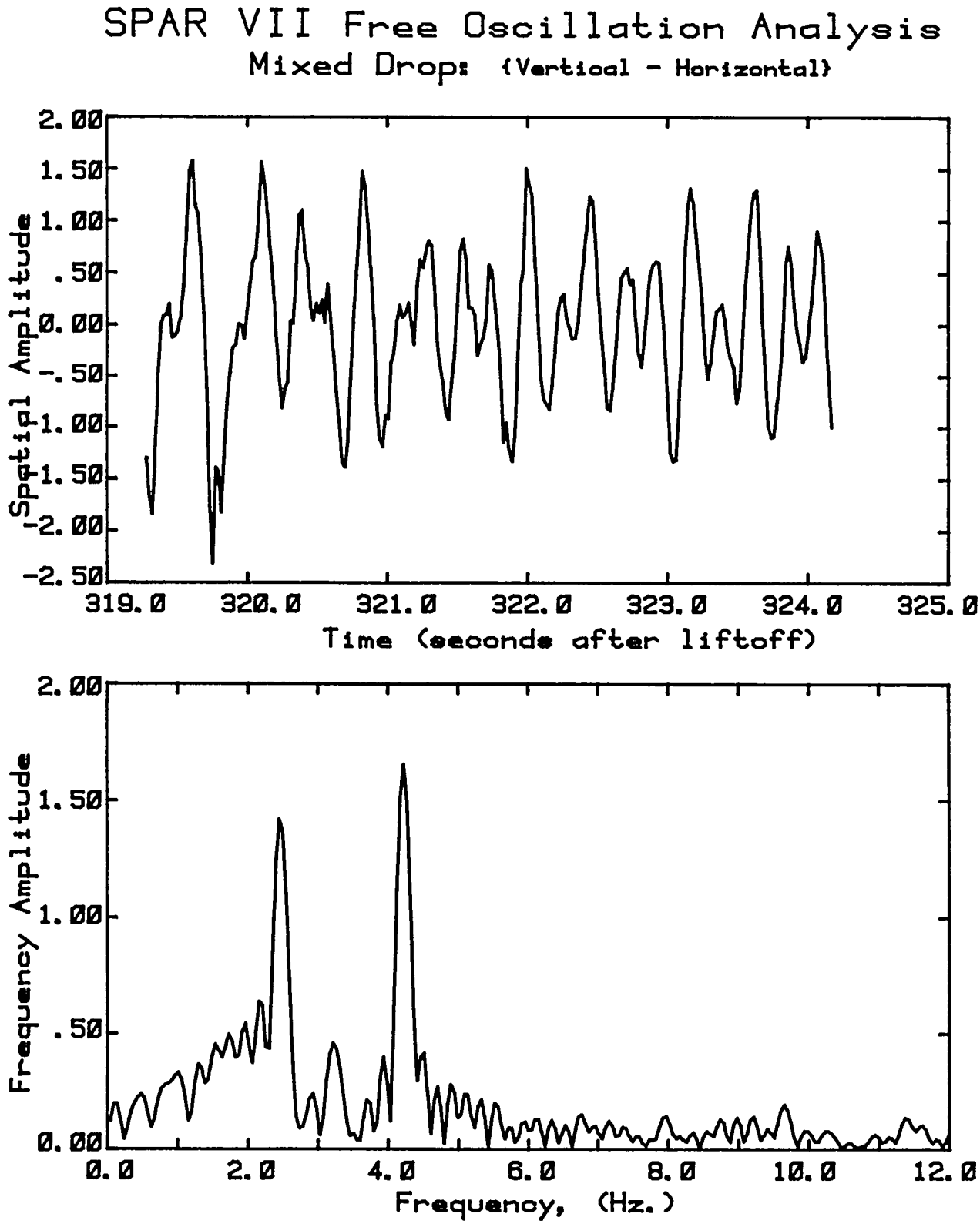

Figure 4.4 The Difference Mode Was Used to Study the Oscillation of the Coalesced Drop. The Oscillation Peak at 3.3 Hz Is Split by the Rotation of the Drop into the Two Peaks at 2.5 and 4.1 Hz.

able is an oscillation of 3.3 Hz combined with a rotation rate of 5.6 radians/second (0.90 Hz). (See Fig. 4.4 again). This would indicate a volume of 5.4 cm^3 using the small amplitude theory.

Study of the spectra for the red drop seemed to indicate as possible an oscillation frequency of 3.6 Hz coupled with a rotation of 1.7 Hz (10.7 rps) (see Fig 4.5). This corresponds to a volume of 4.5 cm^3 and would mean that the volume of the green drop could only be 0.9 cm^3, with $f_2 \sim 8.2$ Hz.

Study of the spectra of the green drop's oscillation indicates that a likely stituation which would be consistent with the data would be that of the drop oscillating at 7.6 Hz (see Fig. 4.6). This frequency would mean a drop volume of 1.0 cm^3. The agreement with the data of the other drops is close but not highly precise. The other peak visible in Fig. 4.6 probably indicates the response due to the modulation force at 4.9 Hz.

A fundamental problem of not being able to positively identify all the major peaks arising from the BOX method analysis has prompted the development of new test cases combining oscillations and rotations. Experience gained in the examination of these artificial situations will in time allow the analysers of data to more quickly and surely unravel this type of spectra. The data from this experiment will be used to test newly developed procedures.

C. Concluding Remarks

Despite the problems engendered by the g-perturbations early in the experiment, the system did deploy a droplet pair which coalesced under the influence of the acoustic fields. In this sequence the drops did behave as planned undergoing large amplitude oscillation. The variety of the data required testing and refining of the analysis techniques used, encouraging

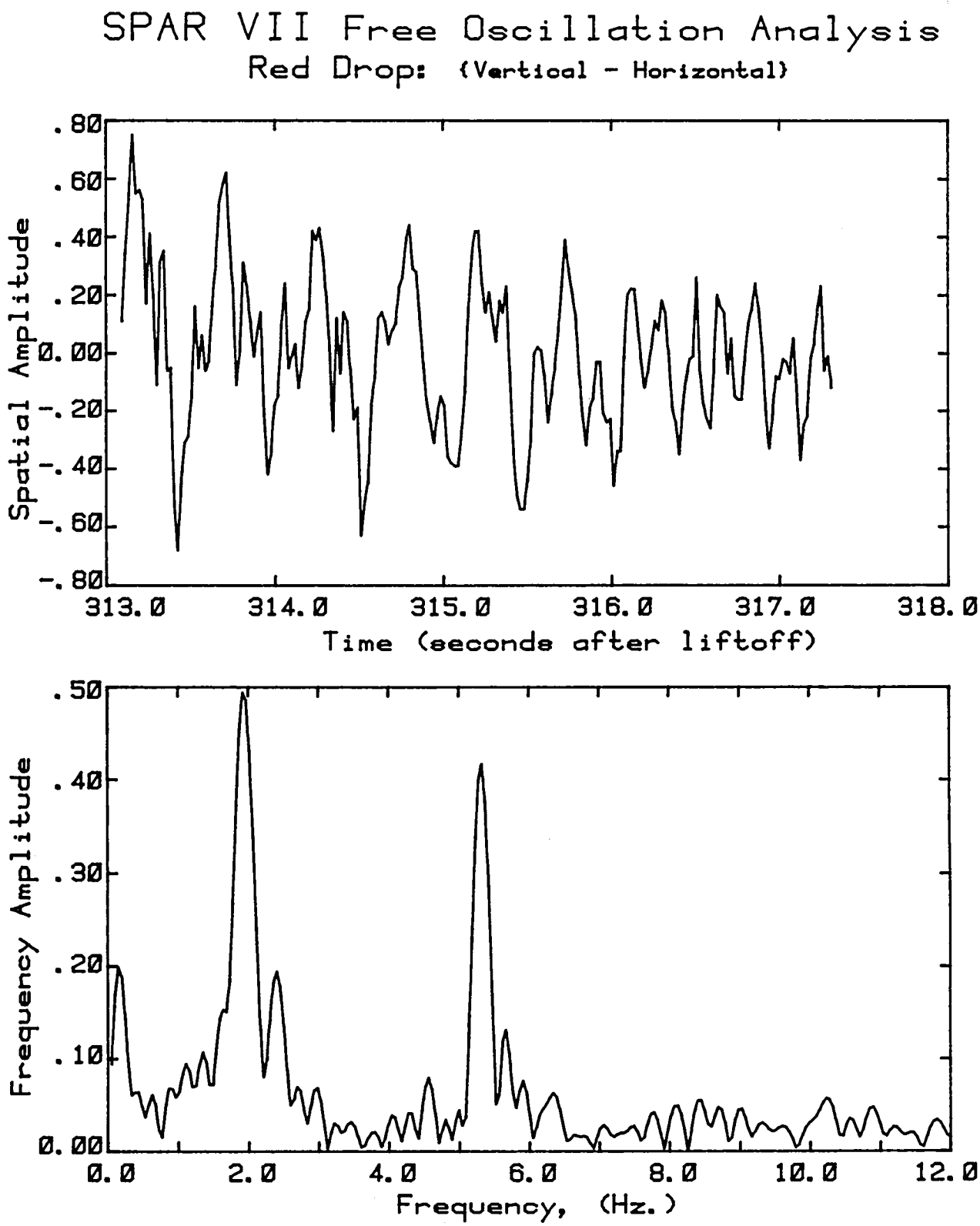

Figure 4.5 The Difference Mode Analysis When Applied to the Red Drop Isolates the n=2 Mode of Oscillation at 5.3 Hz. The Peak at 2.1 Hz Is Not Clearly Understood.

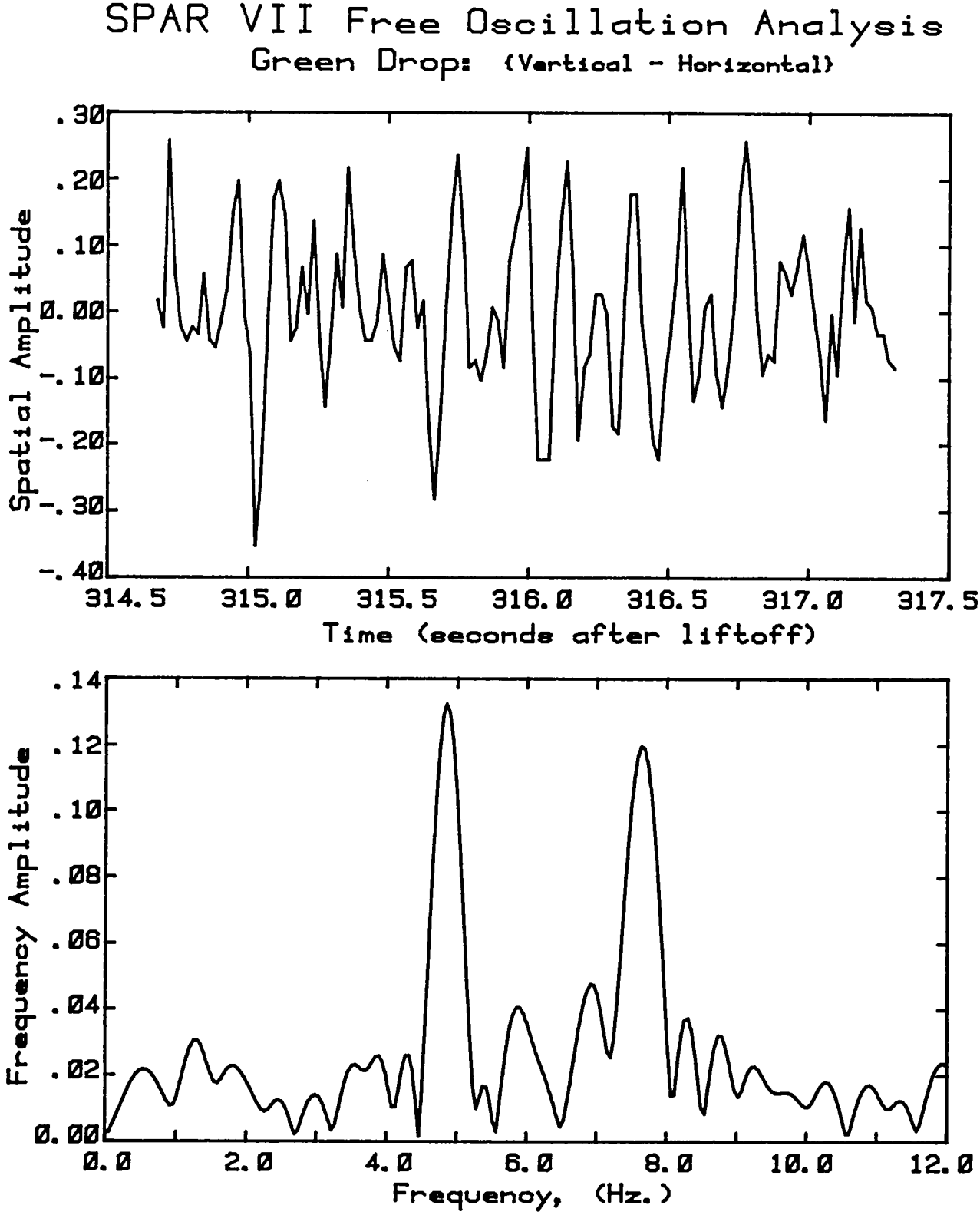

Figure 4.6 The Difference Mode Analysis Highlights Both the Frequency of the Free Oscillation, 7.6 Hz, for the Red Drop and Its Response to the Modulated Force at 4.9 Hz.

the development and implementation of more sophisticated algorithms. The film record of this experiment will provide a valuable pool of experimental data for testing these new ideas.

SECTION 5

REFERENCES

1. Wang. T. G., Elleman, D. D., Jacobi, N., Tagg, R. P., Containerless Processing Technology Experiment Report: SPAR IV Experiment 76-20/1, (1978).

2. Wang. T. G., Elleman, D. D., Jacobi, N., Croonquist, A. P., Containerless Processing Technology Experiment Report: SPAR VI Experiment 76-20/2, (1981).

3. Wang, T. G., Saffren, M. M., Elleman, D. D., Acoustic Chamber for Space Processing, AIAA No. 74-155 (1974). Wang, T. G., Saffren, M. M., Elleman, D. D., Drop Dynamics on Space, Progress in Astronautics and Aeronautics, vol. 52, AIAA (1977).

4. Landau, L. D., Lifshitz, E. M., Fluid Mechanics, Pergamon Press, 1959.

5. Leung, E., Jacobi, N., Wang, T. G., Acoustic Radiation Force on a Sphere in a Resonance Chamber, J. Acoustics Society of America, (to be published, Dec 1981).

6. King, L. V., On the Acoustic Radiation Pressure on a Sphere, Proc. Roy. Soc. 147, 212 (1934).

7. Trinh, E., Wang, T. G., Large Amplitude Free and Driven Shape Oscillations: Experimental Observations, J. Fluid Mech., (to be published, 1981).

CHAPTER V

CONTAINERLESS PROCESSING TECHNOLOGY EXPERIMENT

DYNAMICS OF LIQUID BUBBLES

REPORT

SPAR VII EXPERIMENT 77-18 FLIGHT I

September 1981

D. D. Elleman, A.P. Croonquist, N. Jacobi, and T. G. Wang

ACKNOWLEDGMENTS

The authors wish to thank L. Robinson, K. Tarver, D. Kerrisk, and H. Press of JPL for their valuable assistance in all phases of this experiment. Dr. Wang wishes to thank R. Chassay, D. Schaefer and R. Fallon of MSFC for their patience in handling this experiment.

This paper presents the results of one phase of research carried out at the Jet Propulsion Laboratory, California Institute of Technology, under Contract No. NAS 7-100, sponsored by the National Aeronautics and Space Administration

SECTION 1

INTRODUCTION

This final report describes one phase of an experimental research program designed to contribute to the understanding of containerless processing of fusion targets - microballoons - in space. Study of the stability and manipulability of liquid shells at room temperature is a useful and cost effective intermediate step in the development of a better understanding of the fluid physics pertinent to the production of fusion targets and the capability to fabricate fusion targets in a zero-G environment.

The primary goal of the experiment is to study three aspects of containerless processing of fusion targets in space: drop sphericity, bubble centering and adiabatic bubble expansion.

Drop sphericity studies will help to determine the competing effects of surface tension and residual G-jitter on the positioned sample, thus impacting the orbital requirements on the spacecraft.

Bubble centering studies will enable us to determine the centering capabilities of various techniques such as rotation, electrical charging, and temperature gradient, thus impacting the design requirement on the containerless processing of the fusion target facility.

Adiabatic bubble expansion studies will allow us to better understand the induced instability as the heavy medium accelerates toward the light medium. In addition, adiabatic expansion will allow us to increase the selection of microballoons available by varying size and wall thickness in a

controlled manner, thus impacting the versatility of containerless processing of fusion targets in space.

The practical knowledge obtained in these studies will aid in the design of a high-temperature system for containerless processing fusion targets in space. The study takes advantage of the laboratory work and zero-G aircraft tests under way at JPL, KMS, and LLL as part of the overall NASA Materials Processing in Space program.

This experiment utilized a new acoustic levitation rocket instrument similar to the instrument described in AO:OA-76-02 with minor modifications. Two rocket flights in a two-year period were planned. This report covers the results of the first of these two flights, 77-18 SPAR VII.

SECTION 2

OBJECTIVES

The primary objectives of the flight were to:

1) Determine the sphericity of a positioned liquid bubble.

The equilibrium shape of a positioned liquid bubble is the result of the balance of acoustic forces, surface tension, and spacecraft G-jitter. The sphericity of the liquid bubble will be determined from the film record.

2) Determine the efficiency of bubble centering by oscillation. The centering force generated by the oscillation of the liquid shell will be studied by acoustically exciting the liquid shell in its various normal oscillation modes. The centering mechanism will be compared with theoretical models developed at JPL.

3) Determine the perturbation on bubble centering by G-jitter. As the rocket experiences G-jitter, the liquid bubble moves back and forth within the chamber. The liquid bubble experiences a non-symmetrical modulating force, thus perturbing its shape. This can produce unwanted coupling between rotation and oscillation of the drop.

4) Study the natural resonant frequencies and damping mechanism of bubble oscillation. The resonant frequencies and the damping coefficient have been calculated. This experiment allows comparison of observed and calculated values.

5) Adiabatic expansion of liquid bubble. The liquid bubble's physical size and wall thickness is determined by the pressure difference across the

two boundaries and the surface tension of the water/air interface. As the exterior pressure decreases, the bubble expands its size and reduces its wall thickness. The post-flight film analysis will study the bubble surface velocities and accelerations, and also the surface instabilities.

SECTION 3

APPARATUS AND OPERATION

This experimental SPAR flight utilized a new acoustic levitation rocket instrument similar to that instrument described in AO:OA 76-20, and flown on SPAR VI 76-20, October 1979. The primary modification to this instrument was an addition to the injection system to allow the injection of air into the drop to form a liquid shell. This flight is the first of a series of flights that are intended to study liquid shell behavior. The second flight is scheduled to take place in the latter portion of 1980, and will include rotation of the drop.

A. Apparatus

Figure 3.1 shows the SPAR VII rocket payload 77-18 with the payload shell removed. The instrument consists of a triaxial acoustical levitation resonance chamber[1] which is used to position and control liquid drops or shells in a low-G environment. This particular chamber is nearly cubical though the three dimensions were purposely made slightly different to preclude interference effects. The chamber's inside dimensions are 10.59 x 11.42 x 12.70 cm for the x, y, and z axes, respectively. Three acoustic drivers are fixed rigidly to the center of three mutually perpendicular faces of the chamber.

During operation of the system, each driver excites the lowest-order standing wave along the direction that the driver faces. In a resonant system, the pressure is maximum at the nodes of the velocity wave and minimum

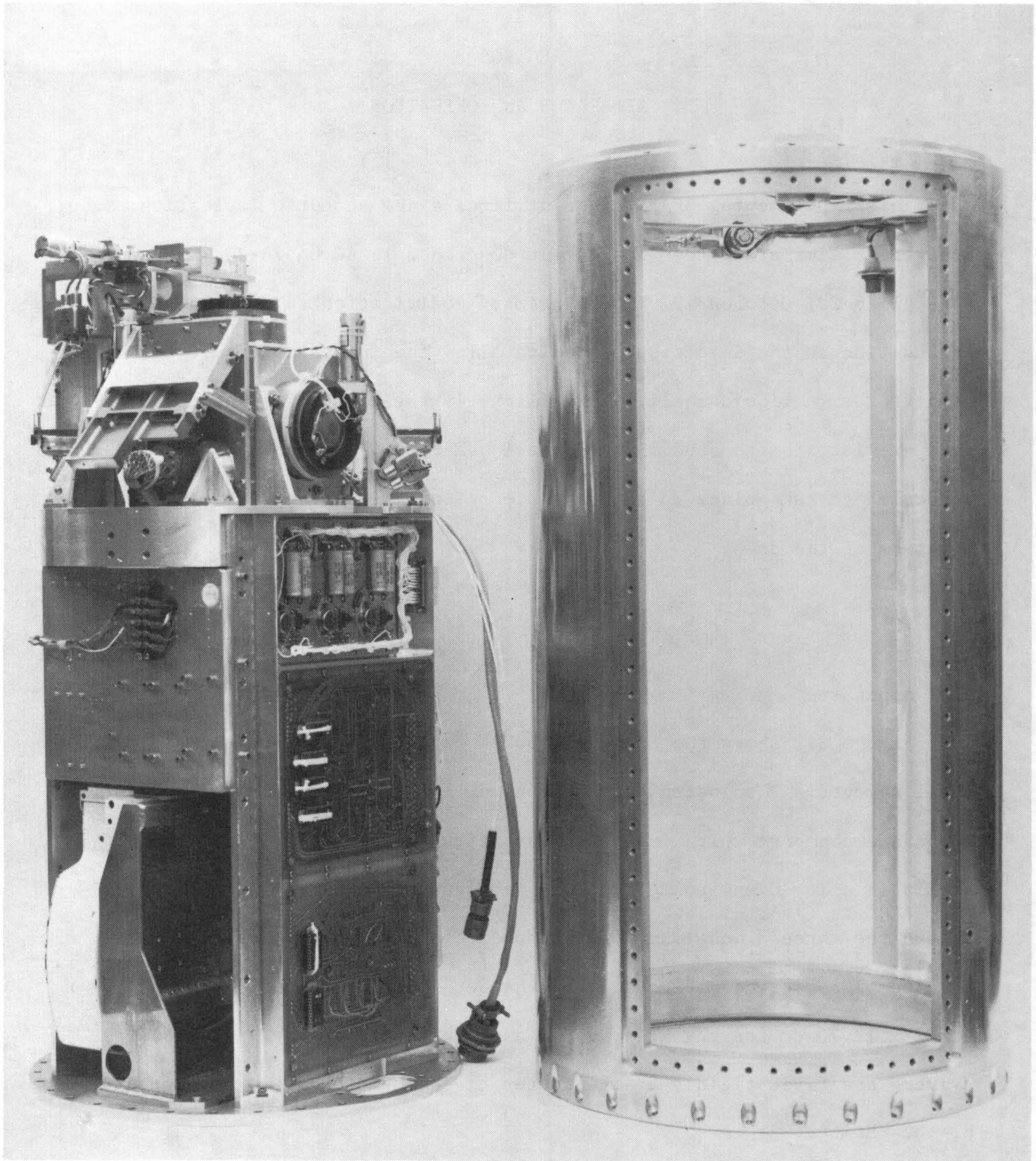

Figure 3.1. The 77-18 Experimental Payload Flown on SPAR 7

at the antinodes; in this geometry the velocity nodes occur at the walls and the antinodes at the center of the chamber. There is a tendency for introduced liquids and particles to be driven toward the antinodes, where they collect and remain until the acoustic excitation is turned off.

Calculation of the acoustic forces on the drop is simplified by the fact that the characteristic impedance of the liquid ρc is very much greater than that of the gas $\rho_o c_o$: ρc (10^5 cgs)/ $\rho_o c_o$ (40 cgs) ~ 10^3 where ρ and ρ_o are the densities of the liquid and gas, respectively, and c and c_o are the respective sound velocities. Because of this impedance mismatch, the acoustic power in the drop is three orders of magnitude smaller than that in the gas and can be neglected. This simplifies the expression for the radiation pressure $\langle \Delta P \rangle$, which is time-independent and is given at the boundary by

$$\langle \Delta P \rangle = (\overline{P^2}/2\rho_o c_o^2) - (1/2)\rho_o(\overline{\vec{u}^2}) \tag{1}$$

where P is the excess acoustic pressure, $\vec{u}$ is the gas particle velocity, and the heavy bars over P^2 and $\vec{u}^2$ denote time average of the quantities. Eq. (1) is the Bernoulli equation,[2] which gives the acoustical perturbation to the ambient pressure.

The pressure profile in this system can be derived as follows. The velocity potential of the wave in the chamber can be expressed as

$$\phi = \phi_x \cos(k_x x) e^{i\Omega_x t} + \phi_y \cos(k_y y)\, e^{i\Omega_y t} + \phi_z \cos(k_z z) e^{i\Omega_z t}, \tag{2}$$

where $\phi_{x,y,z}$ are the complex velocity potential amplitudes of standing waves

of frequency $\Omega_{x,y,z}$ and wave number $k_{x,y,z}$. The particle velocity $\bar{u}$, by definition, is $u = \nabla\phi$. The pressure is given by $P = -\rho\dot{\phi}$. With only one of the three drivers on ($\phi_x = \phi_y = 0$), the resulting expression for the radiation pressure is

$$\langle \Delta P \rangle = \rho_o k_z^2 P_z^2 \cos 2k_z z \tag{3}$$

In this situation the pressure node is a plane ($z = L_z/2$), which becomes a point when all three drivers are turned on. This has been verified experimentally. Because this is a three-dimensional system with independent control on each dimension, it has a great deal of versatility. It can position a drop acoustically and then manipulate it by inducing either drop oscillation or rotation.

The primary source of data from this experiment is cine film obtained with a 16 mm camera. The camera is directed along the z axis; two mirrors give nearly orthogonal views along the x and y axes. In addition the sound intensity at each wall, the deployment system, camera and lighting status, the frequency of the z axis signal and the ambient pressure were monitored and recorded. A portion of the MSFC accelerometer data has been supplied to aid in the data analysis. The x, y, and z axis accelerometer data is coaxial with the x, y, and z axes of the acoustic chamber, the view of the camera for each of the axes is from the positive axis to the negative axis of the accelerometer.

B. Operation (Rotation and Oscillation Experiments)

This section gives the operating characteristics of the acoustic chamber required to conduct the oscillation and adiabatic expansion experiments on the liquid shell.

(1) The liquid used in this experiment was distilled water with small quantities of dye added to provide optimum contrast in the cine film. The surface tension of the dyed water sample was measured before and after the flight and was found to be 71.0 $\pm$ 2.0 dynes/cm. The water was deployed into the center of the chamber through two coaxial syringes. The 8.0 cc of water was deployed in 15 sec. The 2.4 cc of air was injected with concentric tubes inside the water syringes 5 seconds after the end of the water injection. This was done so as to minimize unwanted flows within the shell. The injector tips were withdrawn from the shell while the acoustic field was positioning the shell.

(2) Assuming that the sample to be studied is a water droplet with radius, a = 1.25 cm, the residual acceleration it feels is 10^{-1} cm/sec^2 (~ 10^{-4} g), and the quality factor, $Q = \Omega/\Delta\Omega$, of the acoustic chamber is 25. For this water drop in an acoustic field Newton's equation of motion is

$$\int \langle \Delta P \rangle \, n_z \, dA = \rho_o \, 10^{-4} g \, (4/3) \, \pi a^3 .$$

In the limit of ka $<<$ 1, this has been calculated by King[3] to be

$$(P^2/2\rho_o c_o^2)(5k/6)2\pi a^3 \sin 2kz = (4\pi/3)\rho a^3 \, 10^{-4} \text{ g}.$$

For a 2.5 cm diameter sphere of density 1 g/cm^3, the corresponding minimum acoustic pressure required to position the drop is P ~ 10^3 dyn/cm^2 ~ 134 dB, where the decibels are measured against the reference pressure 2 x 10^{-4} dyn/cm^2. For a 50% efficient compression driver, less than 0.2 W of electrical power is needed to provide the required acoustic pressure. It is worth pointing out that at this acoustic pressure level the surface tension force, F_s, that acts on the water drop is two orders of magnitude larger than the acoustic force, F_A: $F_s/F_A = (\sigma 2\pi r)/(\int \langle \Delta P \rangle n_z dA) \sim 100$.

(3) If the amplitude of the foregoing 134 dB acoustic wave is modulated

at a given frequency Ω_o, the drop experiences a modulated force $F_o = \int \langle \Delta P \rangle_o \, n_z \, dA = 1$ dyne. When Ω_o matches the frequency of the normal modes of oscillation of the drop ω_n, where $\omega_n^2 = n(n-1)(n+2)\, \sigma/\rho a^3$, the amplitude of the drop oscillation can be as large as $|A_n| = |F_o/(\Omega_o M_d \beta_n| \sim 1$ cm, where β_n is the damping constant of the nth mode of the drop, and M_d is the mass of the drop. Since the drop radius itself is 1.25 cm, even a small modulation force is sufficient to drive the drop into large amplitude oscillation at least at the fundamental frequency. However, higher power modulation is required for higher modes because of the increase in damping. That there is sufficient power to stimulate this very large amplitude response has been demonstrated in KC-135 flight experiments; in fact, the prototype was able to shatter a water drop of 1.25 cm radius in less than 1 sec while operating at the fundamental frequency.

(4) Chamber depressurization

The acoustic chamber is switched to a mode in which the acoustic power is set at a low value (140 db) to hold the drop in the center of the chamber. The chamber pressure was connected to the outside atmosphere to commence depressurization. The rate of chamber depressurization was programmed to provide controlled expansion of the liquid bubble for the remainder of the low gravity portion of the flight.

C. Instrument Calibration

(1) Acoustic Calibration

The acoustic intensity calibration was difficult to accomplish because the instrument did not have calibrated microphones in the chamber. In fact the primary interest was not in the sound intensity itself but in the

positioning force produced by the acoustic standing waves. Therefore the acoustic intensity was calibrated by measuring the acoustic positioning force itself. The force measurement was made by suspending a low density (styrofoam) sphere (1.25 cm radius and 0.229 g weight) 3.175 cm from the center of the chamber on a thin string 5.08 cm long (see Figure 3.2). The signal to each speaker was adjusted so that the acoustic force deflected the sphere 0.115 in. (0.292 cm) toward the center of the chamber. This corresponded to a force of 12.5 dynes. The signal level to the speakers was preset so that the acoustic centering force would be 25.0 dynes from deployment to just prior to the adiabatic expansion and 12.5 dynes for the remainder of the flight.

(2) Liquid and Gas Volumetric Calibration

The liquid and gas deployment systems were tested before the flight by taking repeated volumetric measurements of the deployed liquid and gas. There was a variability of several percent in these measurements caused by back lash in the gear system that drove the syringe system. Typical measured volumes were 8.0 $\pm$ 0.1 cc water and 2.4 $\pm$ 0.1 cc air.

(3) Sequence and Time Line Calibration

The program had been run through the flight sequence over 100 times in pre-flight tests. No deviation from the programmed sequence was observed in these tests. In addition, flight telemetry confirmed the sequence operated as programmed during the flight.

(4) Cine Camera and Lighting Calibration

Camera, lighting and film tests were run before the flight. A liquid drop was simulated, placed in the chamber and photographed with the flight camera to test light levels and camera alignment. The quality of the

ACOUSTIC FORCE CALIBRATION

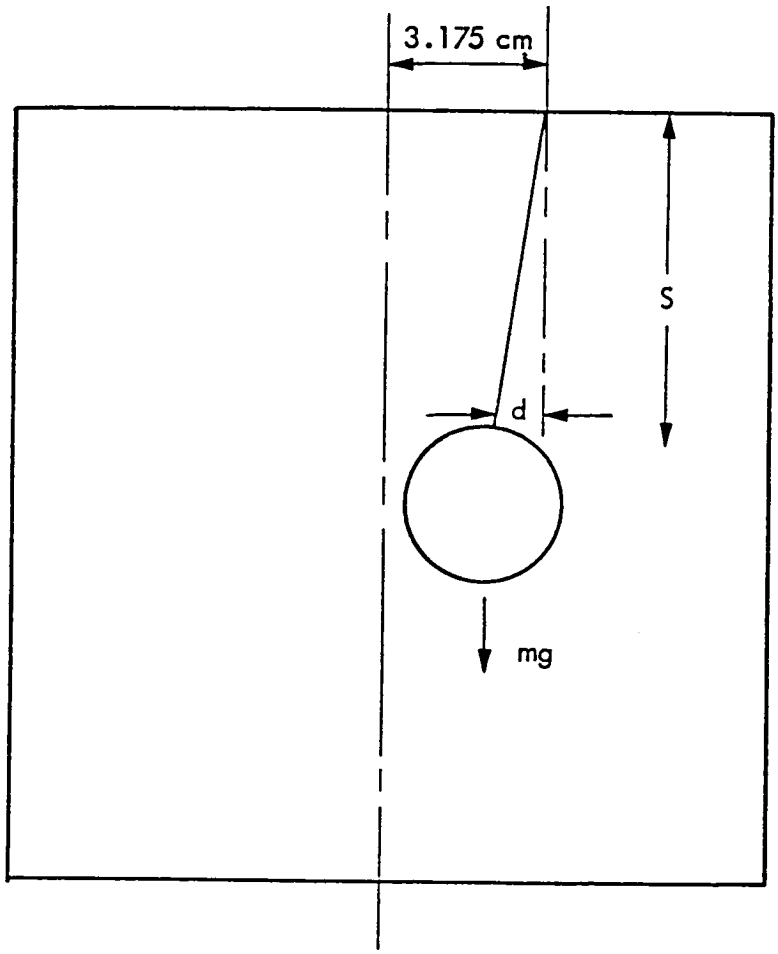

ACOUSTIC FORCE $F_A = mg \frac{d}{S}$

Figure 3.2. Acoustic Calibration Technique. With one speaker on, the level to that driver was adjusted so that a 0.229g styrofoam ball, suspended from a 5.08cm string at a distance of 3.175cm from the center of the chamber along that axis, was deflected toward the center 0.292cm. This is equivalent to an acoustic force of 12.9 dynes.

images was confirmed by the PI and CoI to be acceptable for data analysis.

D. Flight Experiment

(1) Pre-flight Preparation

The JPL experiment 77-18 was flown on SPAR VII on May 14, 1980. Pre-launch testing of the instrument indicated all systems were functioning and ready for flight. The only problem that was encountered was the appearance of small air bubbles in the fluid deployment system of the instrument. On May 13, the PI and CoI (Wang and Elleman) with MSFC personnel were able to extract the air from the lines and the instrument was judged ready for flight.

On the morning of the flight of SPAR VII the PI was informed by Roger Chassay of MSFC that there were several options available to the PI for obtaining an optimum low-gravity platform from the SPAR rocket. We could choose not to use the stabilization system, i.e. not fire the small control jets, and hope that the rocket experiment package did not tumble or rotate too fast, or we could refrain from using the stabilization system until acceleration forces exceeded some predetermined range and then activate the system. It was decided to go with the second option.

(2) Telemetry Analysis

An analysis of the telemetry data from the JPL SPAR VII 77-18 experiment indicates that the system functioned according to the pre-launch timeline that had been programmed into the instrument. All subsystems on the instrument operated as commanded by the programs. In addition, postflight tests and operation of the instrument indicated that the instrument

functioned according to the programs and, in fact, it was still in operating condition after the flight. The telemetry indicated that there was a slight pressure drop in the chamber which could be due to a leak in either the valves or the seal on the access door. The drop in pressure was small and did not have a detrimental effect on the experiment.

(3) Acceleration Forces on the SPAR Platform

Figure 3-3 is a copy of the accelerometer data supplied to JPL by D. A. Schaefer of MSFC on 7/2/80. As can be seen in the data, several spikes occurred along the x and y axes. The largest spike was approximately 10^{-4} g. The acceleration force that occurs at 108 seconds produced a small motion of the drop in Experiment 77-18. This motion did not adversely affect the experiment. The reason the motion was small, even though the acceleration was larger than at 119 seconds, was that the drop itself was not completely injected, and in fact the drop was quite small at this time. Therefore, surface tension forces were large compared to inertial forces. It should be noted that all of the acceleration data that is now available is for times which occurred before the drop had been deployed in the chamber.

(4) Liquid Shell Deployment

In Experiment 77-18, only one experimental sequence was programmed: the deployment of a water drop and the injection of an air bubble into the drop. The experiment was conducted as planned. However, the air bubble was not as large as anticipated because the probe tips were not adequately covered by the water when the air flowed through the injectors. In addition during deployment, the drop was not centered between the probes. This

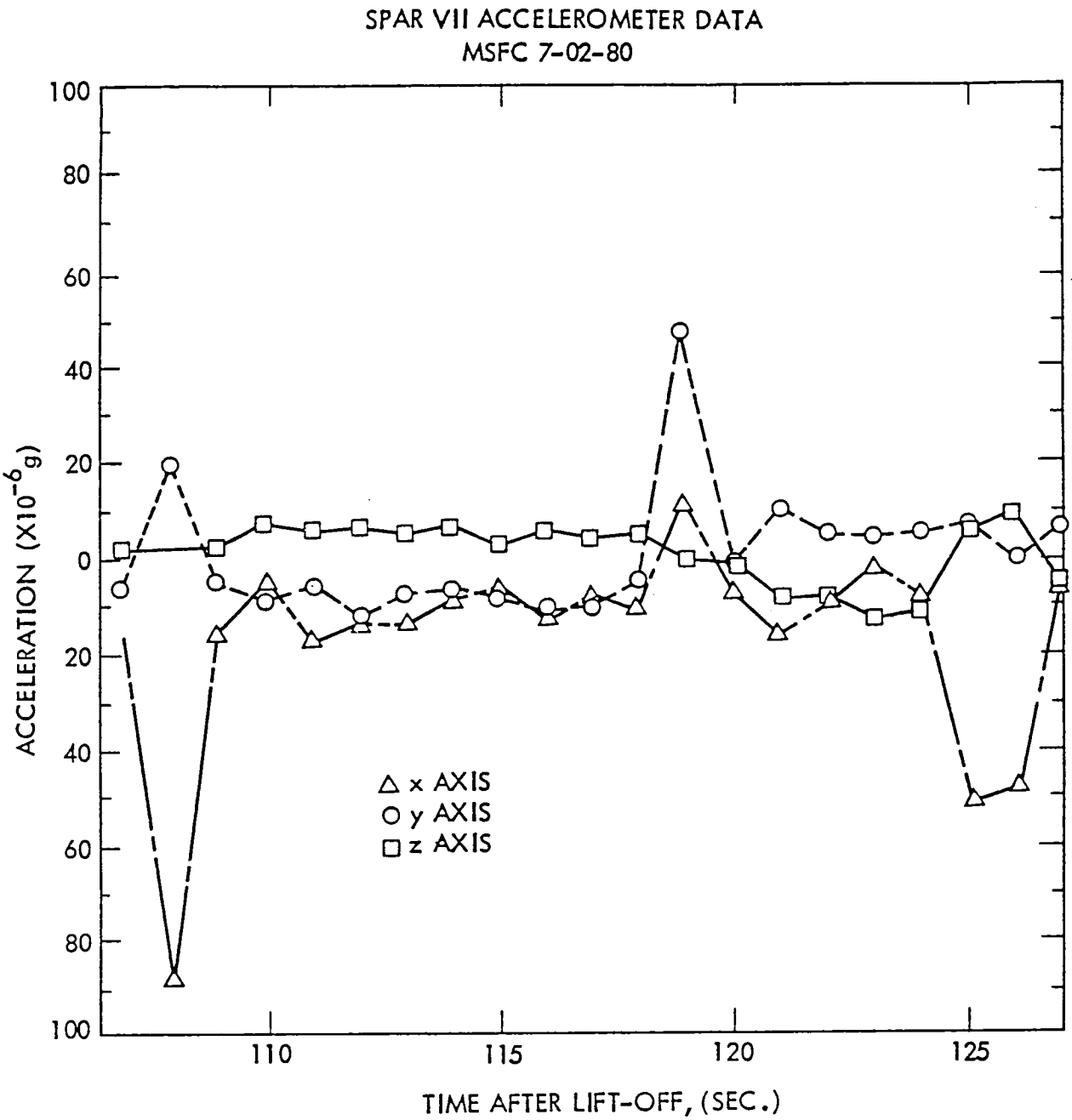

Figure 3.3. Accelerometer Data During Deployment (supplied by D. Schaefer, MSFC).

resulted in an oscillation of the drop in the acoustic potential well. The acoustic force was sufficient to hold the drop and prevent it from contacting the container wall. The acoustic force caused the small air bubble to move in the drop more than was planned and will complicate the data analysis. The motion caused by the acoustic restoring force should result in additional scientific information that will be of considerable interest though it was not planned for the original experiment.

Analysis of the data indicates that the entire 2.4 cc of air was not injected into the drop. Measurements from the cine film show that approximately 0.16 cc of air was injected. The remaining volume of air escaped from the shell during the injection process because the drop did not contact the injector tips as planned.

(5) Objective Accomplished

The minimum acceptable success criteria for the first flight were to:

Determine the sphericity of a positioned liquid shell.

Obtain data on the damping constant of liquid bubbles.

Obtain data on the centering force generated by oscillation.

The analysis of the data indicates that these objectives have been met.

SECTION 4

DATA ANALYSIS

A. Introduction

(1) General Comments

The experiment was scheduled as follows:

T=105 sec (after lift off): Dyed water is injected through both probes,

T=125 sec: Air is injected into the drop through both probes,

T=150 sec: Probes retract from shell,

T=165 sec: 30% amplitude modulation of z axis begins (modulating frequency is swept from 2.0 to 3.0 Hz),

T=285 sec: Modulation stops, sound pressure level drops 3 dB,

T=290 sec: Ambient pressure drops from 14.5 to 3.0 PSI in 80 seconds.

The orange water shell was to be 8.0 cm^3 water and 2.4 cm^3 air. The level of the signal to the acoustic speakers had been preset so that the force in each of the three directions was balanced at 25.0 dynes at 3.175 cm from the center of the chamber. The surface tension was measured at JPL before and after the flight and found to be 71.0 dynes/cm.

Analysis of the film record was carried out upon a Vanguard Motion Analyzer. It was hoped that the available information could be studied using simple and straightforward techniques which could be accomplished without a long lead time. The primary analysis that could not be accomplished using this equipment was the accurate determination of boundaries to test shell sphericity, bubble concentricity and damping. If the air bubble had been

larger, then the accurate study of inner and outer surfaces would have been neccessary and the technique inadaquate.

A simple system of computer assisted analysis called VERHOR was developed to study the behavior of a drop or shell using only information from the Vanguard Motion Analyzer. Requiring only four points per view per frame this technique is a compromise between the full analysis which requires the digitization of the entire boundary and the simple determination of frequency behavior by the operator of the Analyzer which requires only the ability to count frames. Figure 4.1 illustrates the VERHOR method and Figures 4.2, 4.5, and 4.7 show the results of using the method.

VERHOR METHOD

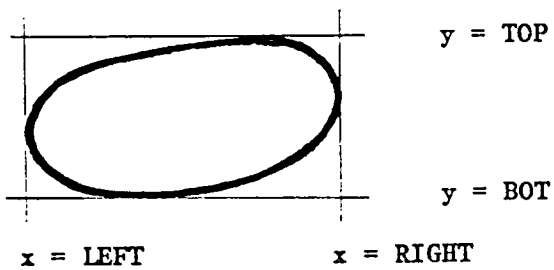

Procedure:

a) from the film, obtain five numbers:

TIME (in seconds after liftoff)

z = LEFT,RIGHT (in Analyzer units)

x = BOT,TOP (in Analyzer units)

b) to study drop oscillation (eg. using Fourier techniques):

analyze H = |RIGHT-LEFT|

V = |TOP-BOT|

D = {TOP-BOT}-{RIGHT-LEFT}

c) to study the center of mass motion:

analyse X = {TOP+BOT}

Z = {LEFT+RIGHT}

Fig. 4.1 - The VERHOR method is a computer program which finds the smallest box which contains the drop boundary for each frame and the variations in the box size and locationcan be analysed. It is a simple, quick and versatile technique.

(2) Determination of Radius

In order to relate the observed behavior to predicted responses an accurate value of the radius is required. If the actual surface tension of the drop were known, an equally accurate value of the radius could be found from the observed frequencies of natural oscillation (see Eq. 10). Using f_2 = 2.7Hz, this technique gives V = 8.1 cm^3 and a = 1.24 cm. It is risky to use the surface tension determined from measurements on liquids stored in bottles when the liquid used has been sitting in the package reservoir and injection lines for several days prior to the actual execution of the experiment. The presence of bubbles in the water line only underscores this concern.

An alternate method for determining the radius is to measure it directly from the film, transforming the image coordinates into actual dimensions. This was done crudely using the known separation of crosshairs which had been etched on the walls and the image coordinates of these points on the Vanguard Analyzer. These scale factors were multiplied by a correction factor which took into account the relative distances of the center of the chamber to the wall in each view. The radius of the drop in image coordinates was measured directly from the film when the drop was close to the center of the chamber. This technique gives a value of the radius of 1.28 $\pm$ 0.1 cm.

With careful effort the chamber coordinates can be related to the six coordinates seen on the film plane (eg. the analysis in Appendix A of the SPAR IV Report[4]) using the known geometry of the chamber, mirror assemblies and camera optics. This was not attempted for this flight as other information was deemed more important and the simpler determinations

described above were considered adaquate.

B. Boundary Analysis

(1) Sphericity

To study the deviation of drop and bubble boundaries from circularity requires the generation of a set of coordinates which closely models the true outline and which is preferrably large in number. When the system is undergoing large scale oscillation the boundary digitization need not be very precise for useful information to be obtained. In contrast, when the drop and bubble are quiescent, the deviations which may be present are often below the errors introduced by the human/mechanical digitization; the detection of slight deviations requires the careful processing of the frames, generating several boundaries with as many points as possible, in order to identify the small distortions present in a quiet system.

The image boundary (viewed along the z axis) was digitized at three times during the experiment: 6.5 seconds after release, in the later part of the modulation sequence when the shell was quiet and after the bubble had expanded. They were undertaken with the hope of finding the limits of this method and to aid in future decisions upon the appropriate level of analysis.

Four methods which used a computer to aid in the analysis were compared. Three of the routines used simple algorithms and approximations to find the center, (x_o,y_o), and the radius, a, for the boundary data which would minimize the sum

$$\delta^2 = \frac{1}{N}\sum\left\{\sqrt{(x_i - x_o)^2 + (y_i - y_o)^2} - a\right\}^2. \qquad (4)$$

The fourth method found a center, (x_o,y_o), the major and minor axes, a and b, and the angle of orientation of the major axis relative to the x axis, α, by

minimizing

$$\delta^2 = \frac{1}{N}\sum\left\{\sqrt{(x_i'-x_o')^2/a^2 + (y_i'-y_o')^2/b^2} - 1\right\}^2. \qquad (4a)$$

a. Newton's method was used to find the values the (k+1)th iterates $x_o(k+1), y_o(k+1)$ and $a(k+1)$ from the three normal equations

$$\begin{aligned}
\frac{\partial}{\partial x_o}\{\delta^2(x_o(k), y_o(k), a(k))\} &= 0 \\
\frac{\partial}{\partial y_o}\{\delta^2(x_o(k), y_o(k), a(k))\} &= 0 \qquad (5) \\
\frac{\partial}{\partial a}\{\delta^2(x_o(k), y_o(k), a(k))\} &= 0
\end{aligned}$$

These three equations correspond to the principal terms of the normal equations generated by the minimization of equation (4). It appeared that by solving each of these three equations independently for each iteration some precision would be sacrificed for the sake of speed.

b) In the full treatment there is a system of six independent nonlinear equations to be solved. This system was solved iteratively using a multi-dimensional Newton's technique (the Newton-Raphson method). Solutions for the three equations (5) are found by using all partial derivatives (i.e. $\partial^2/\partial x_o \partial a$, $\partial^2/\partial x_o^2$, $\partial^2/\partial x_o \partial y_o^2$ etc.) and not just those of the form $\partial^2/\partial x_o^2$.

c) The most direct solution to equation (4) is to solve the matrix form of the three normal equations by generating and inverting the coefficient matrix which is determined from the data. This corresponds to a least squares analysis in which the coefficients A, B, C, and D are found which will minimize the sum

$$\delta^2 = \frac{1}{N}\sum\{A(x_i^2+y_i^2) + 2Bx_i + 2Cy_i - D\}^2.$$

The matrix form of this equation is

$$\begin{bmatrix} \Sigma(x^2+y^2)^2 & 2\Sigma(x^2+y^2)x & 2\Sigma(x^2+y^2)y \\ 2\Sigma(x^2+y^2)x & \Sigma x^2 & 2\Sigma xy \\ 2\Sigma(x^2+y^2)y & 2\Sigma xy & \Sigma y^2 \end{bmatrix} \begin{bmatrix} A \\ B \\ C \end{bmatrix} = -D \begin{bmatrix} \Sigma 1 \\ \Sigma 1 \\ \Sigma 1 \end{bmatrix}$$

The solution of this system gives the radius and center of the best circle:

$$a = \sqrt{\{(A/D) + (B/D)^2 + (C/D)^2\}/(A/D)^2}$$

$$(x_o, y_o) = (-B/A, -C/A)$$

d) To test for distortion of the drop due to the acoustic forces or the viewing optics, the boundary was fit to the best ellipse using least squares analysis - giving both the magnitude of the disortion (i.e. the ratio of the major to minor axes) and the ellipse's angle of orientation (relative to the x axis). If there is distortion due to the optics, one would expect $\alpha \sim -45^\circ$ and if due to an imbalance between the x and y acoustic pressures, it would be expected near $\alpha \sim 0^\circ$ or 90°. A least squares technique is used to find the values of A, B, C, D and E which minimize

$$\delta^2 = \frac{1}{N} \sum \{Ax_i^2 + 2Bx_iy_i + Cy_i^2 + 2Dx_i + 2Ey_i - F\}^2 .$$

From its solution, one obtains

$$a = \sqrt{\{-1/(A\cos^4\alpha - C\sin^4\alpha)\}}$$

$$b = \sqrt{\{-1/(C\cos^4\alpha - A\sin^4\alpha)\}}$$

$$\text{where } \alpha = (1/2)\tan^{-1}\{2B/(A-C)\}.$$

The results of the four methods are tabulated in Table 4.1. It appears that when checking for circularity even the simplest procedure can give the

same level of accuracy as the full matrix inversion. The test for ellipticity indicated that the drop image was indeed distorted probably along axes which were due to the optics but one could not rule out the possibility that the drop was distorted by the acoustics.

TABLE 4.1. Circularity Test Results

T = 156.5 seconds (shortly after probe retraction, the drop is quiet)
N = 28 points

a)	(4.5543,0.7313) and a = 0.2979	$\delta(4) = 0.0078$	$\delta_m = 0.0158$
b)	(4.5543,0.7313) and a = 0.2980	$\delta(3) = 0.0071$	$\delta_m = 0.0158$
c)	(4.5543,0.7315) and a = 0.2984	$\delta = 0.0072$	$\delta_m = 0.0153$
d)	(4.5546,0.7320), a = .3059, b = .2890 $\alpha = -79.28°$	$\delta = 0.0039$	$\delta_m = 0.0108$

T = 257.3 seconds (after oscillations from forced oscillation have stopped)
N = 49 points

a)	(4.7922,0.9108) and a = 0.2948	$\delta(4) = 0.0056$	$\delta_m = 0.0099$
b)	(4.7923,0.9108) and a = 0.2948	$\delta(3) = 0.0056$	$\delta_m = 0.0099$
c)	(4.7923,0.9108) and a = 0.2951	$\delta = 0.0056$	$\delta_m = 0.0102$
d)	(4.7930,0.9097), a = .3024, b = .2876 $\alpha = -34.48°$	$\delta = 0.0024$	$\delta_m = 0.0069$

T = 378.1 seconds (bubble has expanded by a factor of 1.50)
N = 57 points

a)	(4.7367,0.9178) and a = 0.2967	$\delta(5) = 0.0060$	$\delta_m = 0.0118$
b)	(4.7367,0.9178) and a = 0.2967	$\delta(3) = 0.0060$	$\delta_m = 0.0118$
c)	(4.7366,0.9178)and a = 0.2970	$\delta = 0.0061$	$\delta_m = 0.0122$
d)	(4.7370,0.9188), a = .3050, b = .2896 $\alpha = -46.75°$	$\delta = 0.0025$	$\delta_m = 0.0065$

---

method a: Iterative solution of the three linearized normal equations.
method b: Iterative solution of the (3x3) nonlinear normal system.
method c: Least squares analysis for a circle.
method d: Least squares analysis for a general ellipse.

(2) Natural oscillations

A detailed theoretical and experimental treatment of a compound drop system has been worked out by Saffren, Elleman and Rhim[5]. The pertinent results of this work will merely be quoted here and not worked out in detail. The theory assumes that the drops are concentric and the fluids are inviscid and incompressible. In the present case the outer and inner fluids are air and the shell fluid is water. It is assumed that the surface tension of the inner and outer surfaces are the same. The theory predicts and neutral buoyancy experiments have verified that there are two normal modes for each value of the parameter n associated with the compound drop system. In the higher frequency mode, the + mode, the inner and outer surfaces of the shell oscillate in phase, whereas for the lower frequency mode, the − mode, the two surfaces move with a relative phase of 180°.

The frequencies of the two modes are given by

$$\omega_{\pm}^2 = \frac{-\beta \pm \sqrt{\beta^2 - 4\alpha\gamma}}{2\alpha} \tag{6}$$

where $$\alpha = \frac{R_i^6 \varepsilon^3}{(n-1)(n+2)} \{\Delta\rho_i \Delta\rho_o - \bar{\rho}_n \rho_o \varepsilon^{2n+1}\}$$

$$\beta = R_i^3 \{\sigma_i(\Delta\rho_o + \bar{\rho}_o \varepsilon^{2n+1})\varepsilon^3 + \sigma_o(\Delta\rho_i + \bar{\rho}_i \varepsilon^{2n+1})\}$$

and $$\gamma = \sigma_i \sigma_o (n-1)(n+2)(1 - \varepsilon^{2n+1}).$$

The parameter n can take the values 2, 3, ... and it indicates the various shape oscillation modes, σ_i and σ_o are the surface tensions of the inner and outer surface of the shell, and $\varepsilon = R_o/R_i$ is the ratio of the equilibrium outer and inner radii of the shell. $\Delta\rho_i = (\rho - \rho_i)/n$ and $\Delta\rho_o = (\rho - \rho_o)/(n+1)$ where ρ_i and ρ_o are the inner and outer fluid densities (i.e. the density of air in this case) and ρ is the shell fluid density. Similarly $\bar{\rho}_i$ and $\bar{\rho}_o$ are given by $\bar{\rho}_i = \rho_i/n + \rho/(n+1)$ and $\bar{\rho}_o = \rho_o/(n+1) + \rho/n$.

In the present case the inner radius R_i was small compared to R_o the outer radius. It can be shown that for the limit $\varepsilon \longrightarrow \infty$, one gets

$$\omega_+^2 \longrightarrow \frac{\sigma_i}{R_i^3}\left(\frac{n(n+1)(n+2)(n-1)}{\{n\rho + (n+1)\rho_i\}}\right) \tag{7}$$

$$\omega_-^2 \longrightarrow \frac{\sigma_o}{R_o^3}\left(\frac{n(n+1)(n+2)(n-1)}{\{n\rho_o + (n+1)\rho\}}\right) \tag{8}$$

which means that the + mode and the - mode decouple, and the + mode approaches the oscillation frequency of the core, that is of a bubble alone in an infinite shell, while the - mode goes to the oscillation frequency of a shell alone in an infinite host i.e. the frequency of a drop of water of radius R_o with air surrounding the drop.

The relative magnitude of the displacements for the two modes are given by the relationship

$$\left(\frac{\Delta R_o}{\Delta R_i}\right)_+ = \frac{-1}{\sigma}\left(\frac{\Delta R_i}{\Delta R_o}\right)_- \tag{9}$$

where ΔR_i and ΔR_o are the displacements of the inner and outer surfaces, and σ is the normalized surface tension, given by $\sigma = \sqrt{\sigma_o/\sigma_i}$ which is 1.

In addition it can be shown that as the core of the bubble shrinks $(\Delta R_o/\Delta R_i)_+$ decreases and approaches zero. This means that, for the + mode, only the bubble oscillates and the outer surface shows no response. Similarly for the - mode, as the core shrinks $(\Delta R_i/\Delta R_o)_-$ approaches zero which means that the inner surface, i.e. the bubble shows no oscillation while the outer surface becomes displaced.

Given the expected volumes of 8.0 cm^3 water and 2.4 cm^3 air the frequencies of the normal modes of the outer surface would have been 2.18 Hz (n=2), 4.47 Hz (n=3) and 8.21 Hz (n=4). The inner boundary would have had its lowest order resonance at 6.80 Hz.

Because of the method by which the drop is originally set into oscillation - the retraction of the injector probes - we would anticipate observing primarily the - mode, the low frequency mode with the outer surface oscillating and only a small out of phase motion of the bubble surface. This is indeed what was observed as no + mode oscillation was detected. Given the small size of the bubble, a ~ 0.34 cm, the lowest frequency at which bubble oscillation could be expected would be 25 Hz (see Eq. 7). In later SPAR flights such as SPAR VIII where the bubble is larger both modes should be observable.

Because of the small size of the bubble in the SPAR VII experiment, the compound system has been treated as a simple drop (see Eq. 8) for studying the natural oscillations. Rewriting Eq. 7, for a simple liquid drop the natural frequencies for small amplitude oscillations are

$$f_n^2 = \frac{n(n-1)(n+2)\ \sigma}{4\pi^2\ \rho a^3} \tag{10}$$

With σ ($= \sigma_i = \sigma_o$), the drop's surface tension, ρ its density, a ($= R$) its radius, and f_n the frequency (in Hertz) of the nth mode of oscillation. Since ρ_i/ρ and ρ_o/ρ are of the order 10^{-3} the term with ρ and ρ_o has been ignored. Treating ρa^3 as the mass, M, the equation above can be rewritten in the form

$$Q = \frac{\sigma}{M} = \frac{3\pi f_n^2}{n(n-1)(n+2)} \tag{11}$$

where Q should be constant for a particular drop.

Evidence of the three lowest modes, n = 2, 3, and 4, was seen in the film record in the oscillations of the specular reflections of the photolamps. The direct determination of the modes present through analysis of the boundaries themselves is the definitive approach but it is a much more difficult task. The surface motions of the drop at deployment were quite large ($\lesssim$ 30% of the resting radius) but there was no easily discernible symmetry to identify any of the modes; the complete study of the boundary as a function of time, with calculation of the correlation coefficients and their Fourier transforms would provide the the relative amplitudes of the modes and the damping coefficients with the damping coefficient defined by

$$\beta_n = (n-1)(2n+1)\ \eta/\rho a^2 \tag{12}$$

where η is the kinematic viscosity.

The first method for finding the resonant frequencies involved recording the timing information from the side of the film at the beginning and end of a certain number of periods of oscillation, and determining the frequency

from the average period. When possible many different combinations of reflections taken at several times were used to determine the average frequencies. For each mode the average frequency, the number of sequences, N, used to obtain the averages and the value of Q, the constant of the drop, were:

$f_2 = 2.74$ Hz, $N_2 = 12$, $Q_2 = 8.85$

$f_3 = 5.25$ Hz, $N_3 = 1$, $Q_3 = 8.66$

$f_4 = 8.16$ Hz, $N_4 = 4$, $Q_4 = 8.72$

Using a value of surface tension of 71.0 dynes/cm, which had been measured at JPL before the flight, and an average Q of 8.8, the theoretical formula (11) gives the drop's mass as 8.1 g which corresponds to a radius of 1.24 cm. When corrected for the presence of the bubble this changes only slightly. The ratios of the predicted frequencies (Eq. 10) with each other agree closely to the experimental ratios:

$f_3/f_2 = 1.936$ (theory)

$= 1.92$ (experiment)

$f_4/f_2 = 3.000$ (theory)

$= 2.98$ (experiment).

The VERHOR method, illustrated in Fig. 4.1, was also used to determine the frequencies at which the drop oscillated immediately after deployment. This invloved taking more data from the film and consequently an order of magnitude more time. Using data from 150.0 to 153.0 seconds after liftoff, the fundemental frequency (corresponding to n=2) was observed to be very strongly present at a frequency of 2.69 Hz (see Fig. 4.2). A weak signal corresponding to the n=3 mode was observed at 5.37 Hz in the Vertical data. Depending on the type of data combination used, the n=4 mode was either a

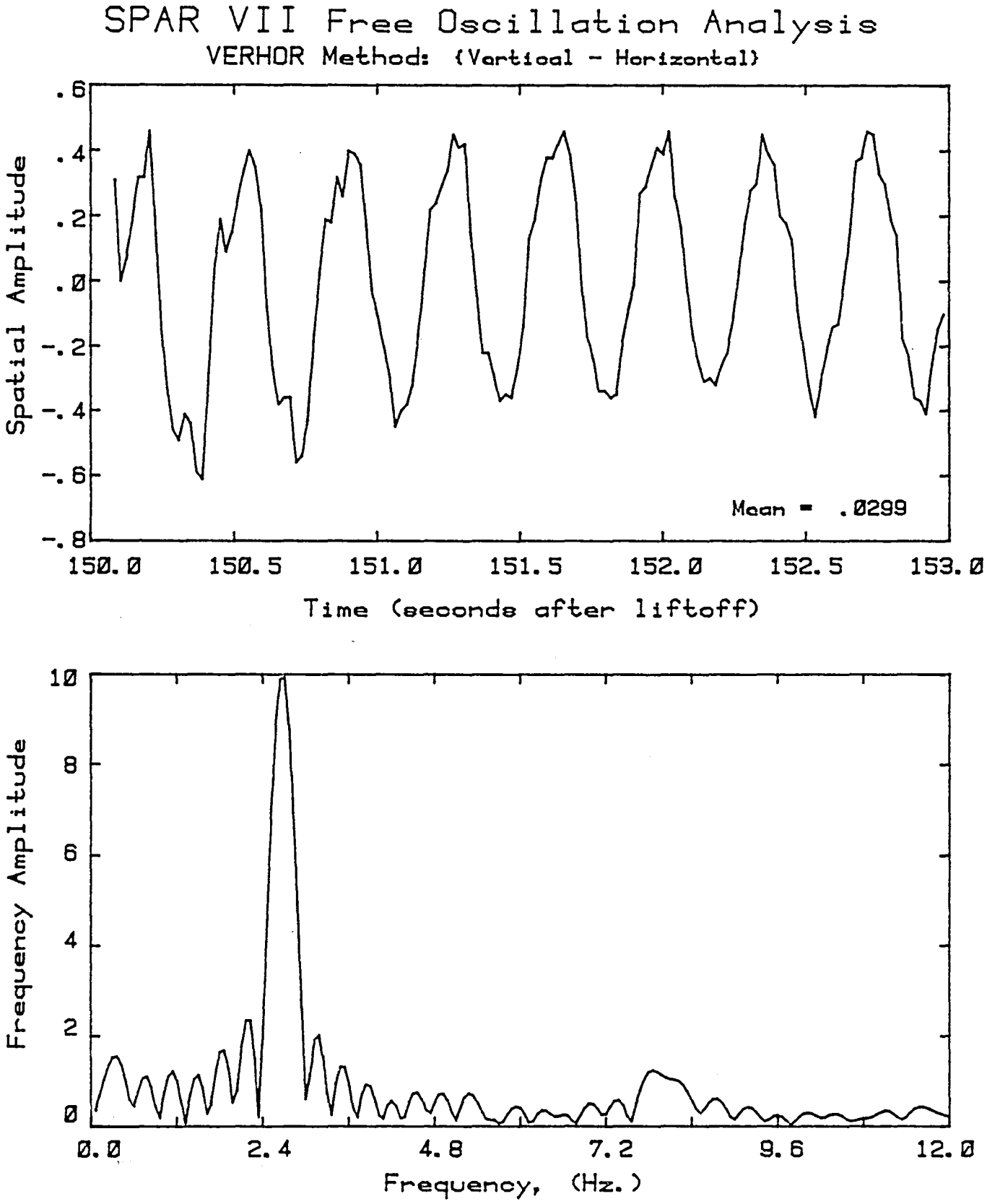

Fig. 4.2 - Natural Oscillation Analysis Immediately After Injector Retraction.

double peak or a skewed peak centered roughly at 8.1 Hz. The width of this peak was roughly 0.37 Hz (which is the order of the theoretical resolution available in the frequency domain). These frequencies would indicate a drop of radius 1.26 cm and a mass of 8.3 g if the surface tension were 71.0 dynes/cm.

The frequencies and volumes determined by these two methods are close but definitely different. To isolate the factors which give rise to this difference will involve more analysis of both techniques. It had been hoped that the precision of the VERHOR method would have been adaquate to definitely pinpoint the frequencies but the time sequence used was not sufficient.

C. Center of Mass Motion

Because the probes were tangent to the drop during deployment and at release, the drop was given sufficient energy by the retraction of the injectors to oscillate within the acoustic potential well for the entire flight. This permitted study of the strength of the acoustic forces under varying conditions, as both the acoustic and ambient pressures were changed in the course of this experiment. The latter was partially accidental, as the telemetry showed a slow leak which appeared 30 seconds after liftoff and dropped the ambient pressure from roughly 14.5 PSI at deployment (150 sec) to 12.2 PSI at 290 sec when the scheduled leak began.

From the analysis of King[3], the force upon a sphere of radius a and density ρ, in a one dimensional acoustic standing wave (with wave number k and acoustic pressure p) is approximately

$$F(z) = - \frac{5\pi k^2 a^3 p^2}{3\rho_o c_o^2} z \qquad \text{for } 2kz < 1 \tag{13}$$

where z is the coordinate along the direction of propagation; for the geometry used z = 0 is at the center of the chamber. The approximation in Eq. (13) is valid within 2.0 cm of the center for this acoustic chamber.

In analogy to the simple harmonic oscillator, an object in the acoustic field will move with a frequency Ω, where

$$\Omega^2 = \frac{5\ k^2 p^2}{4\rho\rho_o c_o^2} \tag{14}$$

A crude frequency corresponding to the center of mass motion was determined from the film by recording the times when the drop had moved the furthest from the center for each of the three axes. This period was averaged over two

cycles and the frequency was found from the average. Figs. 4.3 and 4.4 illustrate the results for the x and y axes from this analysis for the entire experiment. The right hand scale indicates the force corresponding to the frequency of the drop motion for a simple drop with a mass of 8.1g (as was determined from the free oscillation analysis).

During calibration of the experiment, the voltage to the speakers was set such that the forces along each of the axes were balanced at 25.0 dynes at 3.175 cm from the center; these correspond to frequencies of oscillation of 0.198 Hz, 0.189 Hz and 0.179 Hz for the x, y and z axes, respectively, for the expected liquid shell during the first half of the experiment. Because of the slow leak the force and the frequency slowly decreased, nevertheless the average forces at 3.175 cm were found to be 22.9 and 21.6 dynes, along the x and y axes. When the sound pressure level dropped by 3 dB at 285 sec, the frequency of oscillation in the potential well dropped by a factor of $\sqrt{2}$. This is clearly demonstrated in Fig. 4.4. The fact that this condition lasted only five seconds before the ambient pressure dropped made it difficult to isolate the effects of the drop in acoustic pressure using the Vanguard Analyzer. At 290 sec, the valves were opened, the ambient pressure dropped steadily and the force decreased in a similar manner; because both the acoustic pressure and the density are proportional to the ambient pressure, the force is also, (see Eq. 13). Despite an apparant loss of lock at 329 sec as recorded on the telemtry data, the drop was kept near the center until 403 sec when it started toward the wall.

Using the apparant volumes and the calibrated sound pressure level the expected frequencies were 0.152 Hz for the x axis, 0.145 Hz for the y axis, and 0.138 Hz for the z axis. These are to be compared to the values observed

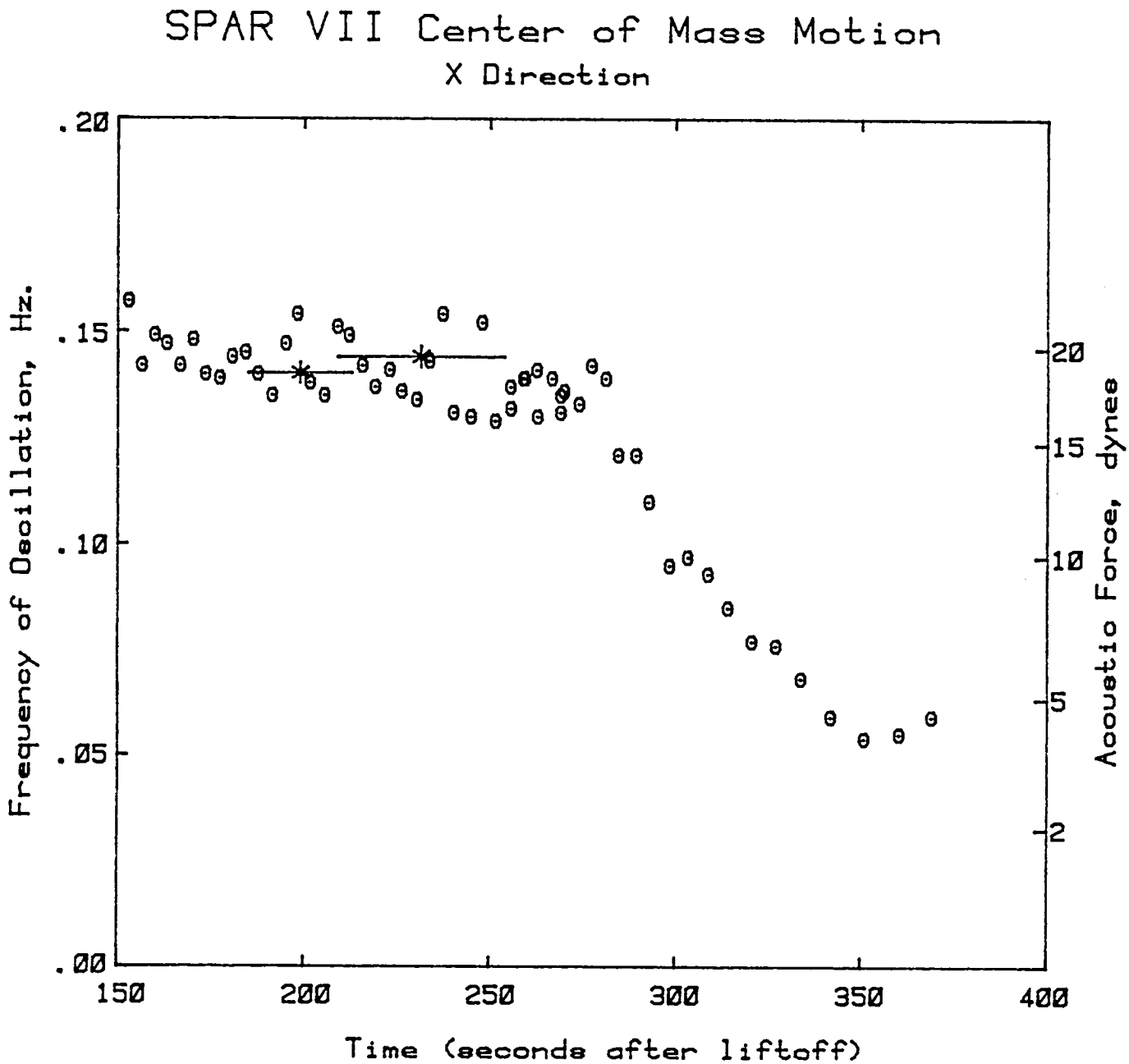

Fig. 4.3 - Center of Mass Motion in the X Direction.

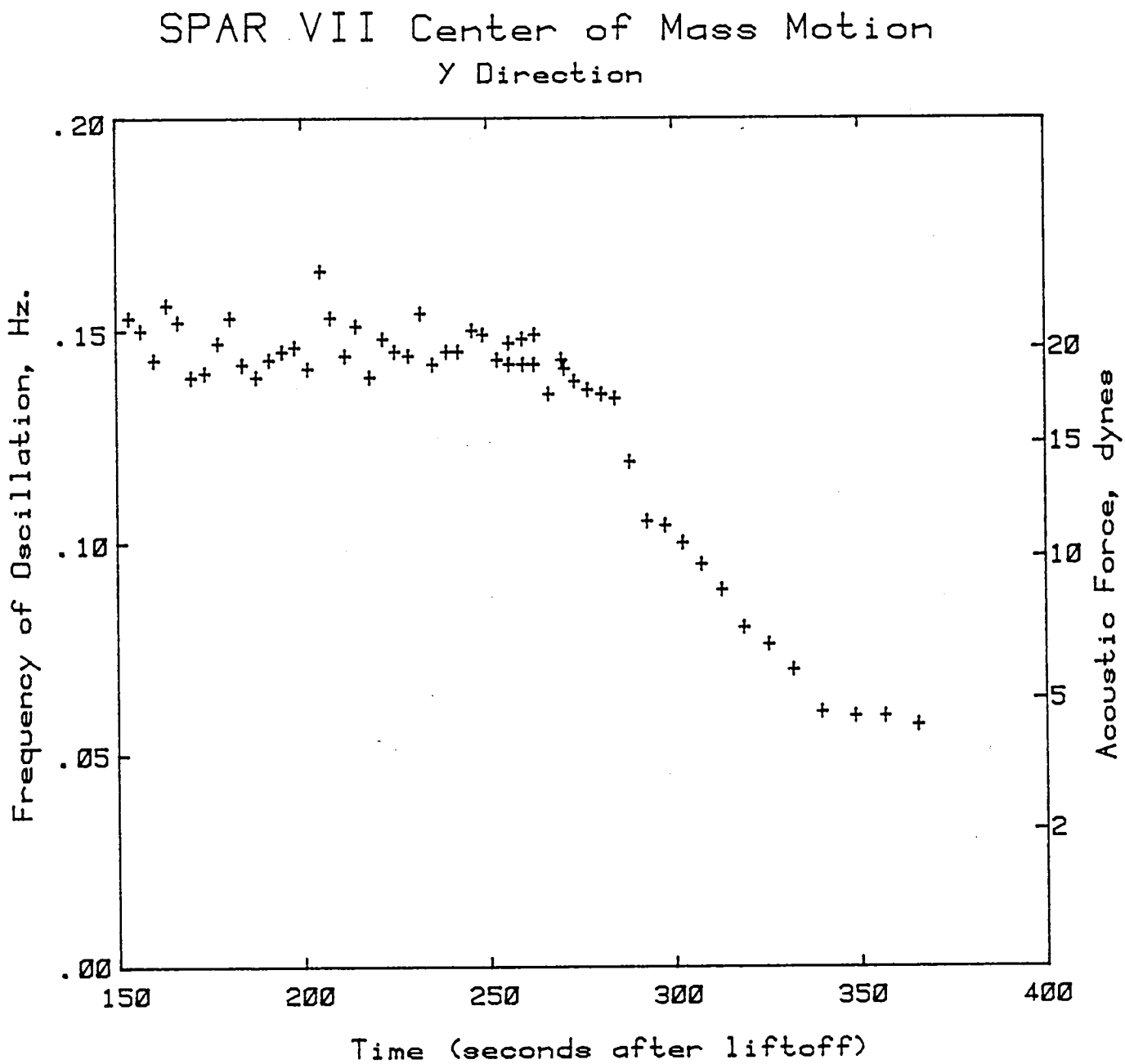

Fig. 4.4 - Center of Mass Motion in the Y Direction.

by the period counting method which were 0.145 Hz for the x axis and 0.149 Hz for the y axis. The predicted frequencies were determined for a chamber in which the pressure is at 1.0 atm. Because of the unscheduled leak these frequencies can be taken only as the extrapolation back to when the pressure was 1.0 atm had the acoustic signals been on and the shell deployed (see Figs. 4.3 and 4.4).

The scatter in the data reflects the effects of digitization and statistical errors as well as the experiment's response to the outside world in which jitters in the microgravity environment manifest themselves in an apparant motion of the drop. In actuality these bumps are transmitted to the drop only through the loose coupling of the acoustic fields.

A byproduct of the VERHOR study of the forced oscillation sequence were values of the frequency of the drop's motion in two of the three possible directions. Figure 4.5 shows the data and its power spectra. The frequencies determined in this manner in the x direction are indicated by the asterisks and horizontal bars in Fig. 4.3. Along the z axis this method gave an average frequency of 0.143 Hz for the time period between 185 and 254 seconds after liftoff.

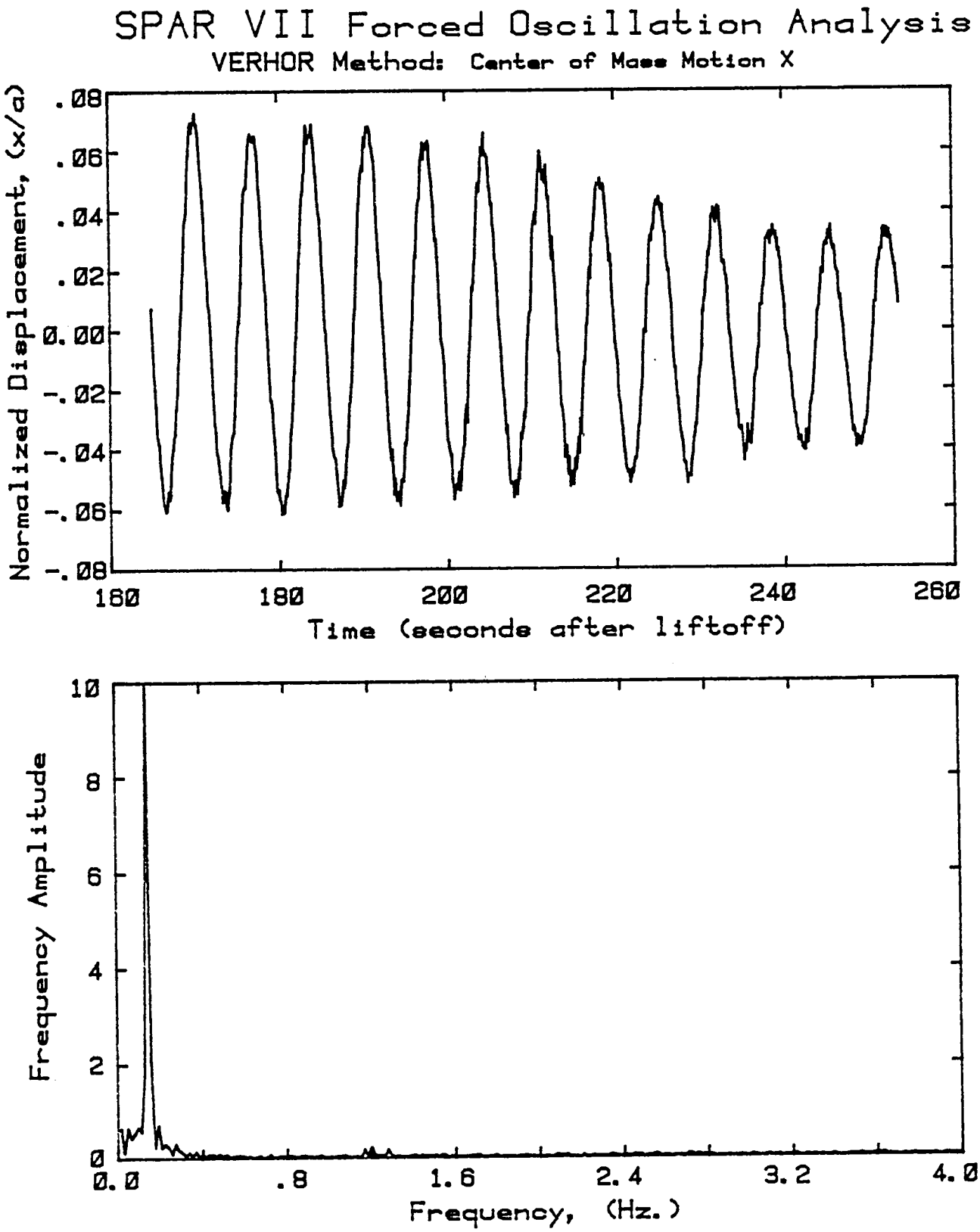

Fig. 4.5 - Motion of the Drop in the Acoustic Potential Well (in the X Direction).

D. Bubble Behavior

Throughout the film the bubble remained as close as possible to the center of the chamber while the drop appeared to move about it as it rocked in the potential well. This effect made it impossible to say whether there was a centering force acting on the bubble during the z-axis modulation sequence or at any other time because the bubble was never free from the effects of the center of mass motion. The tendancy for the bubble to stay as close to the center of the chamber as the shell allowed has been explained as an inertial response: the acoustic forces on the liquid are much greater than those on the bubble and so the acoustic forces move the liquid and the bubble follows. To compare the relative accelerations of the outer and inner shells, r_{drop} and r_{bubble}, the parameter ξ was studied as the drop moved about the chamber where

$$\begin{aligned} \xi &\equiv (\ddot{r}_{drop}) \cdot (\ddot{r}_{bub} - \ddot{r}_{drop}) \\ &= \ddot{r}_{drop} \cdot \ddot{r}_{bub} - |\ddot{r}_{drop}|^2 \end{aligned} \tag{15}$$

Studying the time average of the paramter ξ would indicate whether the motions of the drop and bubble were correlated. If $\xi = 0$, the motions of the two surfaces would be uncorrelated and, if $\xi = \pm 1$, correlated. Visual inspection of the film indicates a value between 0 and -1. Numerical study of this behavior was attempted but could not be concluded because it required determining the second variation in the centers of mass of the liquid and bubble for a large amount of data; the accuracy of the Vanguard analyzer was inadaquate to handle this procedure.

(1) Forced Oscillation

From 165 to 285 seconds the amplitude of the acoustic pressure along the z axis was modulated at 30%. The resulting force was swept from 2.0 to 3.0 Hz (at twice the frequency that the acoustic pressure was modulated). During this sequence the drop went through periods of calm behavior as well as violent oscillation while the bubble to all appearances remained quiescent throughout the sequence. The lowest frequency at which one would expect a response from a 0.14 cm^3 bubble inside a 8.1 cm^3 shell is 25 Hz (see Eq. 7).

The shell (which for all practical purposes was a simple drop) responded to the modulating force very strongly in the first half of the sequence, i.e. from 2.00 to 2.50 Hz (which coresspond to 165 to 225 seconds after liftoff). During the period of maximum response ($f_{mod} \sim 2.33$ Hz), the amplitude of the coefficient of P_2 (from the decomposition of the boundary into spherical harmonics), $|A_2|$, was roughly 0.3 a, the radius of the drop . After that the drop became quiet (see Figs. 4.6 and 4.7). When the modulating force was swept through the frequency of the n = 2 resonance (which had been observed to be 2.74 Hz), at 250 sec the drop did not show any response. The behavior of the drop was also studied using the VERHOR method to look at the distortion of the drop in one of the side views. The response along the x-axis is shown in Fig. 4.6.

During the early part of the large amplitude response the drop's oscillations were about axes which were parallel to the walls; at T = 221.2 sec the large amplitude oscillations appeared to change character. Note the very small amplitude of the signal at 208 seconds in Figure 4.6; this point correlates well with the onset of the running waves on the surface where the image along the z axis appeared static while along the x and y axes the drop

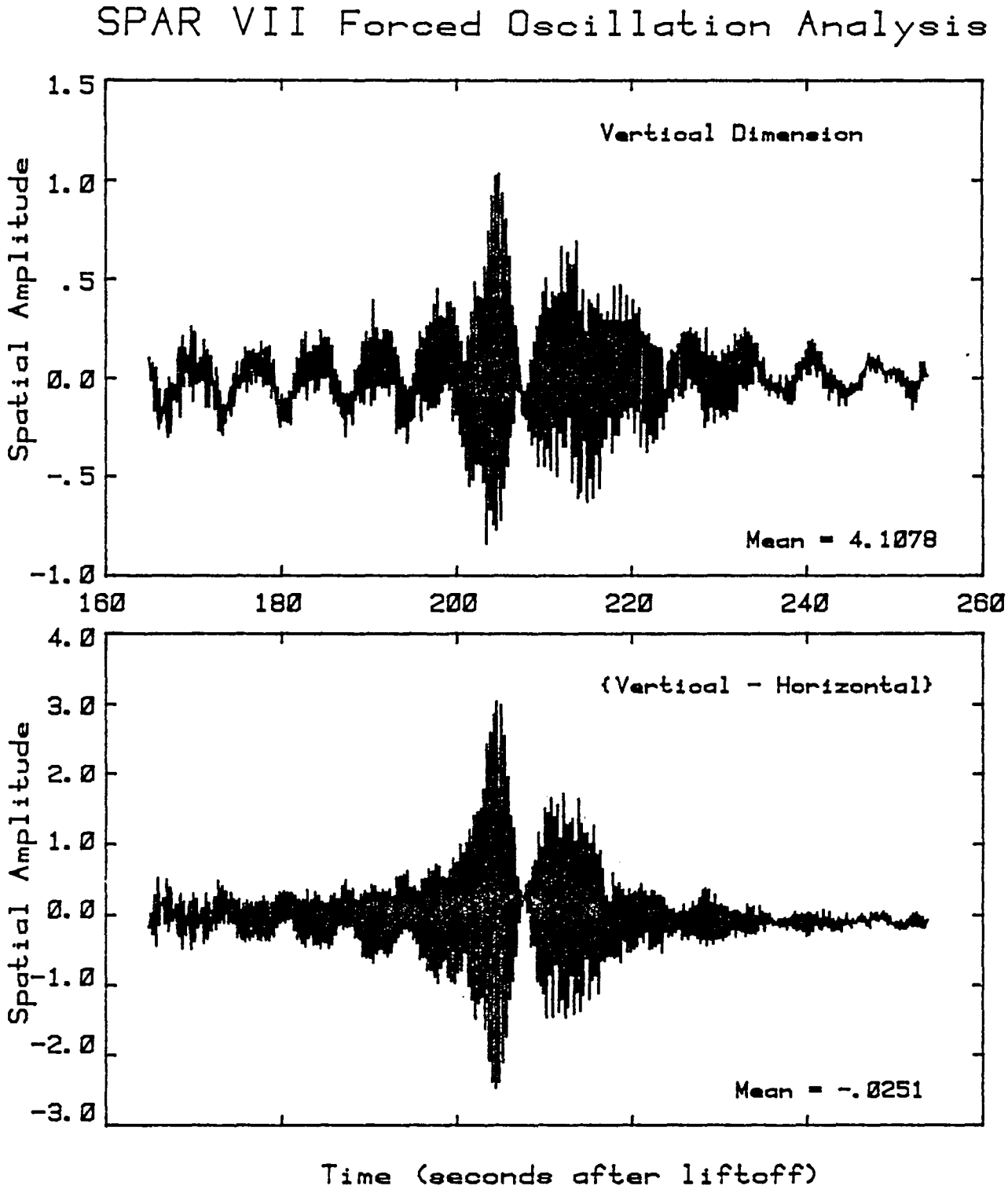

Fig. 4.6 - A Comparision of Two Modes of VERHOR Analysis. The Difference mode minimizes the center of mass motion effects.

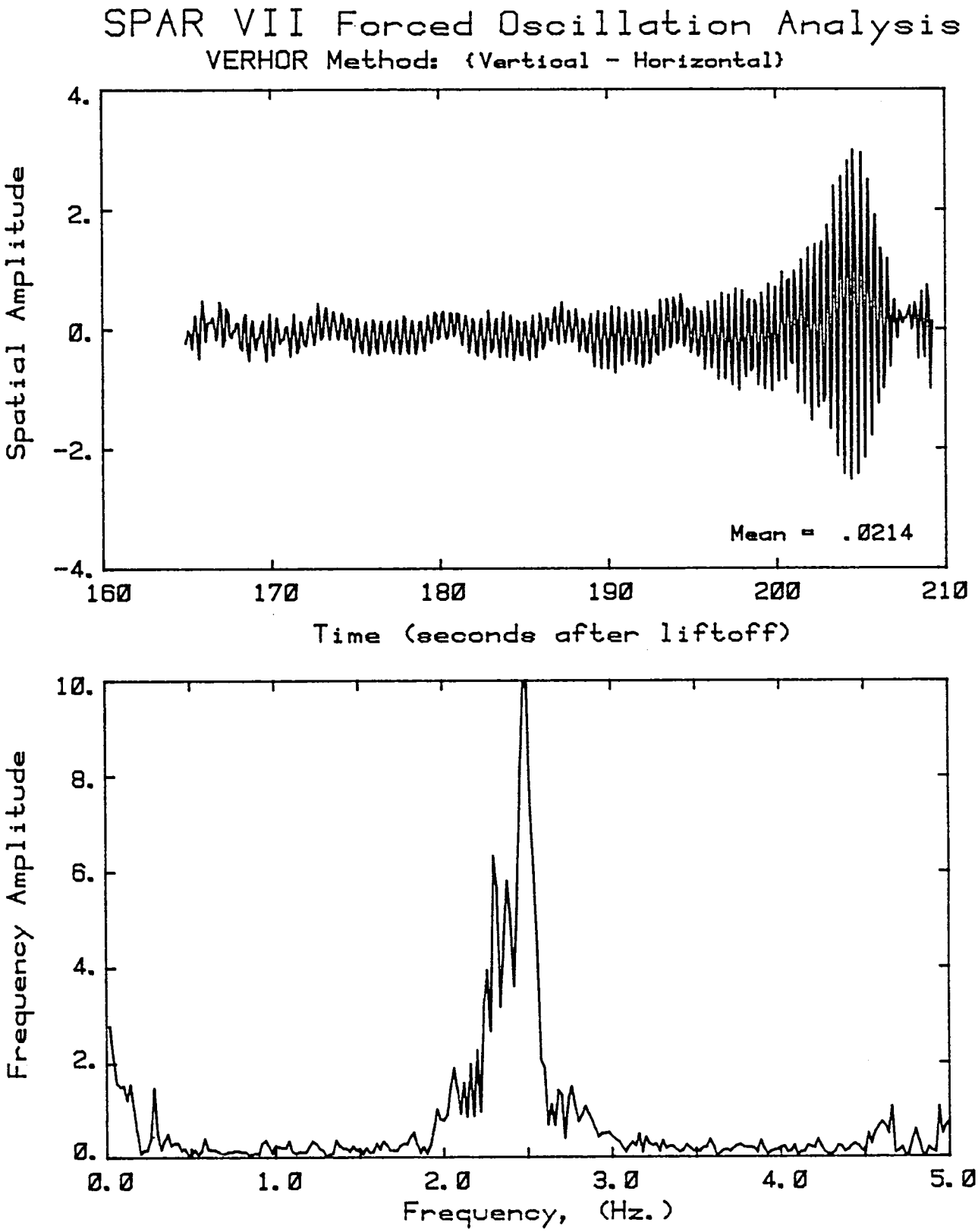

Fig. 4.7a - First Third of the Forced Oscillation Sequence. The modulation frequency is swept from 2.0 to 2.4 Hz in this sequence.

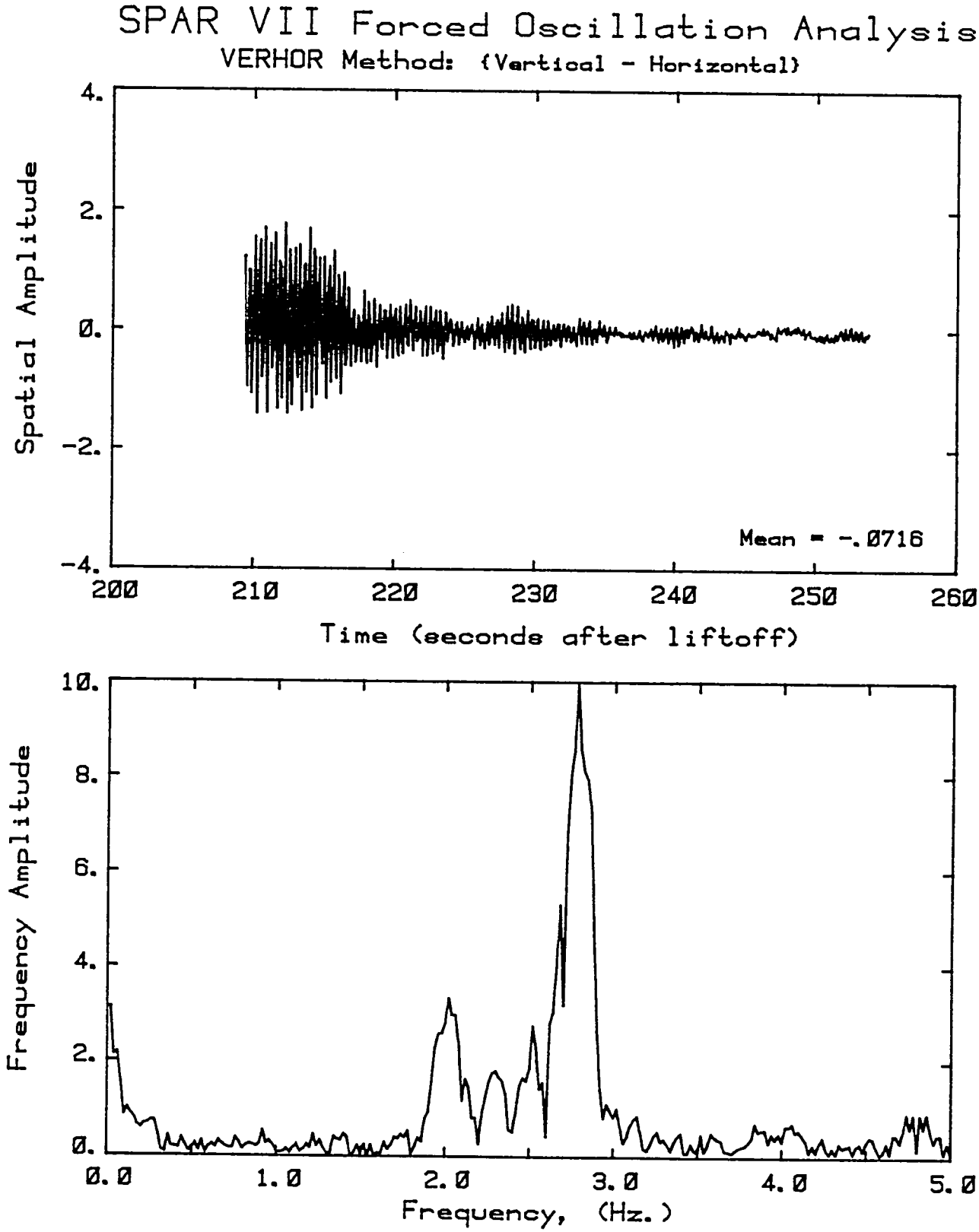

Figure 4.7b. The Second Third of the Forced Oscillation Sequence. The modulating force is swept from 2.4 to 2.8Hz.

seemed to be rotating. By 266 seconds the whole drop appeared to be rotating about one of the diagonal axes in the x-y plane.

This response to a force which is swept through the drop's resonant frequency is not completely understood at present but is being studied further from both theoretical and experimental points of view. It has been observed in both the laboratory and on another rocket flight (SPAR 76-20).

(2) Adiabatic expansion

The deployment system was set to deliver 8.0 cm^3 of water and 2.4 cm^3 of air giving a shell of radius 1.35 cm and a bubble with a radius of 0.83 cm. 290 seconds after lift-off valves were scheduled to open dropping the ambient pressure of the acoustic chamber from 14.5 PSI to 3.0 PSI, thereby increasing the volume of the bubble by a factor of 3.0.

Five seconds after probe retraction, the ratio of the inner to outer radius was measured at 0.26. This ratio increased slightly as the ambient pressure dropped due to a slow leak in the system. During the course of drop relaxation and z axis amplitude modulation, most of the bubbles coalesced into one large, one medium and several small bubbles. This did not occur at a single moment but throughout the entire flight.

There exists an anomaly in the relative bubble size during the period from 280 to 290 seconds (see Fig 4.8). At the same time the acoustic pressure had dropped by a factor of 0.707; what the correlation is between these two facts will be studied in the laboratory.

The relative bubble size increased from 0.24 at 290 seconds to 0.37 at 353 seconds which corresponds to a volume change of roughly 300%.

Errors due to distance from the camera were minimized by measuring the relative radius. A much more serious source of error was the lens effect

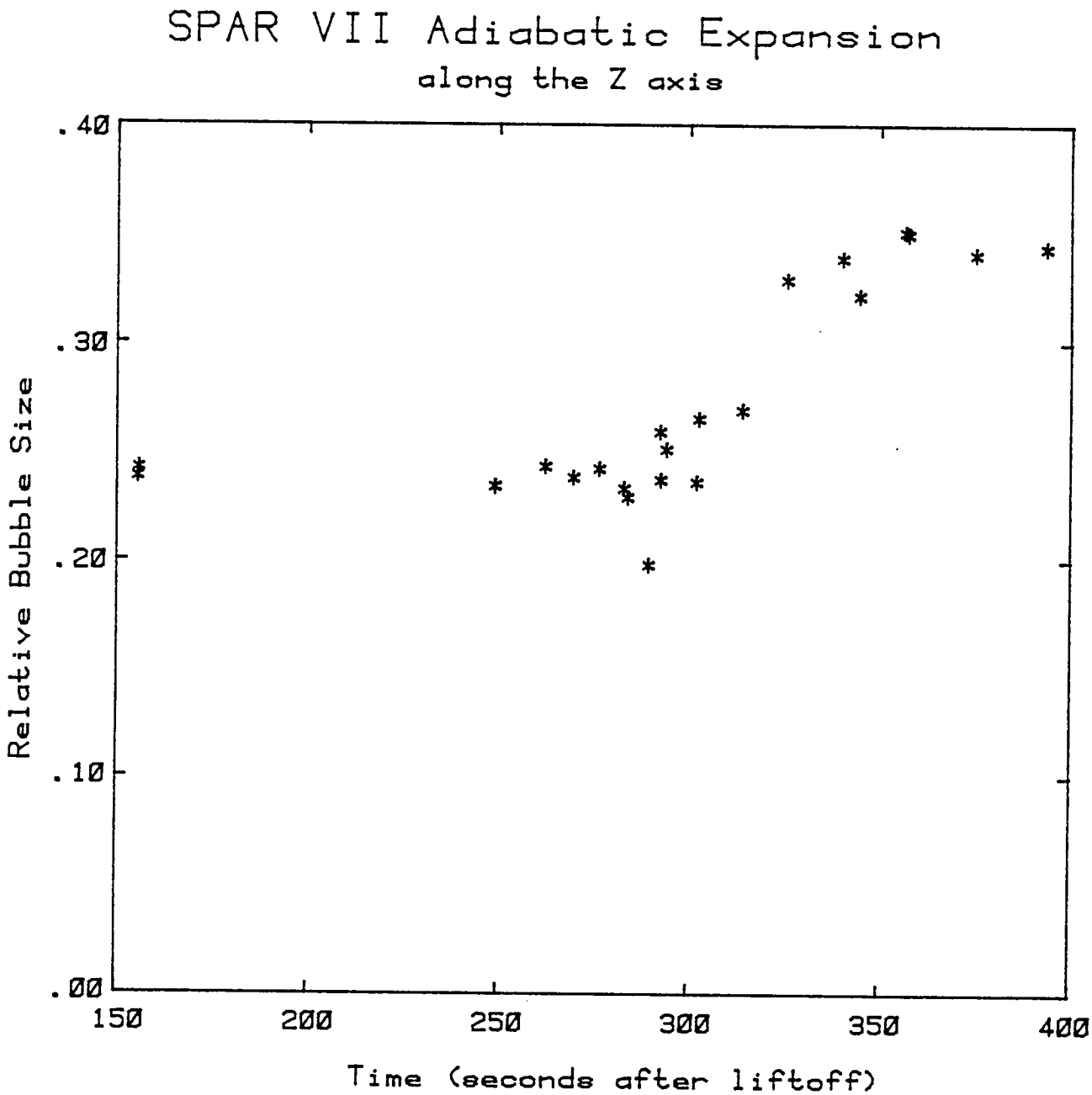

Fig. 4.8 - Data from the Bubble Expansion Experiment.

provided by the outer boundary of the drop and the position of the bubble inside. An attempt to minimize its effect was made by measuring dimensions whenever the bubble was in a specific spot inside the drop and the drop as close as possible to the same location in the chamber.

Shortly after the pressure dropped the formation of many small bubbles began and continued through the remainder of the flight. It is not known to what degree they may have affected the bubble size. They did not appear to respond to any centering force, nor did they seem to coalesce. Even using the small bubbles as tracers, it could not be determined from the film what the motions inside the liquid shell were. They were excellent trace particles in that they were small and plentiful; unfortunately there was no interesting behavior to reveal.

E. Conclusions from the Data Analysis

Using simple techniques of taking information from the cine film record several areas were successfully studied: the observation of the natural oscillations of orders 2, 3 and 4; the characterization of the acoustic potential well in terms of the simple harmonic oscillator potential and the observation of the corresponding frequencies, and the study of the expansion of the bubble as the pressure dropped. The methods used failed to give information about the damping coefficient but allowed a crude analysis of the deviation of the drop boundary from circularity. The VERHOR method was used to study the frequency behavior of the drop after release and during the forced oscillation sequence. Unfortunately in the case of the former it did not corroborate the presence of any n=3 oscillation and in the latter the power spectra did not illuminate the drop's response in a clear manner.

Because of its small size it was impossible to study the natural oscillations of the bubble and the presence of a centering force within the drop was overwhelmed by the drop's motion in the acoustic potential well. The behavior of a drop under a modulated force which is swept through the natural oscillation frequency of the drop is a difficult problem and is being studied.

SECTION 5

REFERENCES

(1) T. G. Wang, M. M. Saffren, and D. D. Elleman, Drop Dynamics in Space, Progress in Astronautics and Aeronautics, Vol. 52 AIAA (1977). Also, Proceeding of International Colloquium on Drops and Bubbles, Vol. II, 266 (1974).

(2) T. G. Wang, M. M. Saffren, and D. D. Elleman, Acoustic Chamber for Weightless Positioning, AIAA Paper 74-155, (1974).

(3) L. V. King, On the Acoustic Radiation Pressure on Spheres, Proceedings of the Royal Society, Vol. A147, (1934).

(4) T. G. Wang, D. D. Elleman, N. Jacobi, R. P. Tagg, Report on SPAR IV Experiment 76-20, Report 750 - 133, Aug 1978. Also, N. Jacobi, R. P. Tagg, J. M. Kendall, D. D. Elleman and T. G. Wang, Free Oscillations of a Large Drop in Space, AIAA Paper 79-0225 (1979).

(5) M. M. Saffren, D. D. Elleman, W.-K. Rhim, Dynamics of Liquid Shells, Technical Digest of Topical Meeting on Inertial Confinement Fusion (Optical Society of America), page 60, 1980. Also M. M. Saffren, D. D. Elleman, W.-K. Rhim, Dynamics of Compound Drops, Proceedings of the International Colloquium on Drops and Bubbles, 1981.

1. REPORT NO.	2. GOVERNMENT ACCESSION NO.	3. RECIPIENT'S CATALOG NO.
NASA TM-82535		

4. TITLE AND SUBTITLE	5. REPORT DATE
Space Processing Applications Rocket (SPAR) Project SPAR VII Final Report	October 1983
	6. PERFORMING ORGANIZATION CODE
7. AUTHOR(S)	8. PERFORMING ORGANIZATION REPORT #
Richard M. Poorman, Compiler	
9. PERFORMING ORGANIZATION NAME AND ADDRESS	10. WORK UNIT NO.
NASA-George C. Marshall Space Flight Center Marshall Space Flight Center, AL 35812	M-419
	11. CONTRACT OR GRANT NO.
	13. TYPE OF REPORT & PERIOD COVERED
12. SPONSORING AGENCY NAME AND ADDRESS	Technical Memorandum
National Aeronautics and Space Administration Washington, D.C. 20546	14. SPONSORING AGENCY CODE

15. SUPPLEMENTARY NOTES

16. ABSTRACT

The Space Processing Applications Rocket Project (SPAR) VII Final Report contains the compilation of the post-flight reports of each of the Principal Investigations (PI's) of the three selected science payloads, in addition to the engineering report as documented by the Marshall Space Flight Center (MSFC). This combined effort also describes pertinent portions of ground-based research leading to the ultimate selection of the flight sample composition, including design, fabrication and testing, all of which are expected to contribute to an improved comprehension of materials processing in space.

The SPAR project is coordinated and managed by MSFC as part of the Materials Processing in Space (MPS) program of the Office of Space and Terrestrial Applications (OSTA) of NASA Headquarters.

This technical memorandum is directed entirely to the payload manifest flown in the seventh of a series of SPAR flights conducted at the White Sands Missile Range (WSMR) and includes the experiments entitled, "Containerless Processing Technology," "Containerless Processing Bubble Dynamics," and "Comparative Alloy Solidification."

17. KEY WORDS	18. DISTRIBUTION STATEMENT
Space processing Containerless processing Solidification Bubble dynamics Acoustic levitation	Unclassified - Unlimited Subject Category: 15

19. SECURITY CLASSIF. (of this report)	20. SECURITY CLASSIF. (of this page)	21. NO. OF PAGES	22. PRICE
Unclassified	Unclassified	130	A07

For sale by National Technical Information Service, Springfield, Virginia 22161

NASA-Langley, 1983

National Aeronautics and
Space Administration

Washington, D.C.
20546

Official Business
Penalty for Private Use, $300

THIRD-CLASS BULK RATE

Postage and Fees Paid
National Aeronautics and
Space Administration
NASA-451

U.S.MAIL

NASA

POSTMASTER: If Undeliverable (Section 158
Postal Manual) Do Not Return